

ADA 070267

NUSC Technical Report 5781

**LEVEL**

10

NUSC Technical Report 5781



14

110-111-5781  
DDC  
JUN 22 1979  
C

# Hatteras Abyssal Plain Low Frequency Bottom Loss Measurements

Peter D. Herstein  
Robert K. Dullea  
Salvatore R. Santaniello

Special Projects Department

(16) FS 552

(12) 11/5/79 (11) 14 April 1979

(17) SF 552602

DDC FILE COPY

# NUSC

NAVAL UNDERWATER SYSTEMS CENTER  
Newport, Rhode Island • New London, Connecticut

Approved for public release; distribution unlimited.

415 115 115

PREFACE

This document was prepared under NUSC Project No. A-650-06, Navy Subproject No. SF 52 452 602-19345, "Low Frequency Forward Scattering Studies," Principal Investigator, S. R. Santaniello (Code 3104). The sponsoring activity is the Naval Sea Systems Command (SEA 06H1-4), A. P. Franceschetti, Program Manager.

The technical reviewer for this report was Gustavo Leibiger (Code 327).

**REVIEWED AND APPROVED: 14 April 1979**



**R. W. Hasse**  
**Head: Special Projects Department**

The authors of this report are located at the New London Laboratory, Naval Underwater Systems Center, New London, Connecticut 06320.

REPORT DOCUMENTATION PAGE		READ INSTRUCTIONS BEFORE COMPLETING FORM
1. REPORT NUMBER TR 5781	2. GOVT ACCESSION NO.	3. RECIPIENT'S CATALOG NUMBER
4. TITLE (and Subtitle) HATTERAS ABYSSAL PLAIN LOW FREQUENCY BOTTOM LOSS MEASUREMENTS		5. TYPE OF REPORT & PERIOD COVERED
		6. PERFORMING ORG. REPORT NUMBER
7. AUTHOR(s) Peter D. Herstein Robert K. Dullea Salvatore R. Santaniello		8. CONTRACT OR GRANT NUMBER(s)
9. PERFORMING ORGANIZATION NAME AND ADDRESS Naval Underwater Systems Center New London Laboratory New London, CT 06320		10. PROGRAM ELEMENT, PROJECT, TASK AREA & WORK UNIT NUMBERS A65006
11. CONTROLLING OFFICE NAME AND ADDRESS Naval Sea Systems Command (SEA 06112) Washington, DC 20362		12. REPORT DATE 14 April 1979
		13. NUMBER OF PAGES 112
14. MONITORING AGENCY NAME & ADDRESS (if different from Controlling Office)		15. SECURITY CLASS. (of this report) UNCLASSIFIED
		15a. DECLASSIFICATION/DOWNGRADING SCHEDULE
16. DISTRIBUTION STATEMENT (of this Report)  Approved for public release; distribution unlimited.		
17. DISTRIBUTION STATEMENT (of the abstract entered in Block 20, if different from Report)		
18. SUPPLEMENTARY NOTES		
19. KEY WORDS (Continue on reverse side if necessary and identify by block number) Bottom Loss Measurements Deconvolution Processing Ocean Bottom Modeling Ocean Sediment Impulse Response Ocean Sediment Sound Refraction		
20. ABSTRACT (Continue on reverse side if necessary and identify by block number) Bottom-loss measurements were made for frequencies less than 800 Hz at three stations in the Hatteras Abyssal Plain. The stations were each separated approximately 55 km along 70°30'W longitude. The data acquisition procedure was to launch two self-recording submersibles (AUTOBUOYS) and then maneuver from and to the launch site detonating explosives as the AUTOBUOYS recorded data. Because of the experimental geometry, the direct and bottom-interacting signals were time-separated as they arrived at the AUTOBUOYS. Thus, a "self-calibrating" (over)		

processing procedure could be used to compute bottom loss values.

Bottom loss versus grazing angles (5-66 deg) was obtained over a wide bandwidth (90-790 Hz) and for a number of narrow bandwidths (1/3 octave and less). Broadband results were found to be homologous between stations, whereas the narrowband results were less correlated. Negative bottom loss values were also observed.

Replica deconvolution processing was performed using the associated time-separated direct and bottom interacted signals over a large range of grazing angles. A history of the bottom/subbottom impulse response as a function of grazing angle was then constructed from the deconvolved signals. This history showed evidence of strong subbottom reflected and sediment refracted arrivals in the bottom interacting signals. Since these types of arrivals were present, the calculation of negative bottom loss can be attributed to use of the Rayleigh plane wave reflection model, which does not account for non-plane wave refracted or reflected signals.

Analyses of the impulse responses for the southern station also aided in developing a geophysical description of the sediment structure. The derived structure consists of a thin (21 m), constant sound-speed layer overlaying a thick layer having a linear depth-dependent sound speed. This structure is representative of a class of documented subbottom sediment structures that can support the propagation of low-frequency acoustic signals traversing non-plane wave reflected and refracted acoustic paths.

Accession For	
NTIS GMA&I	<input checked="" type="checkbox"/>
DDC TAB	<input type="checkbox"/>
Unannounced	<input type="checkbox"/>
Justification	
By _____	
Distribution/	
Availability	
Dist.	Avail and/or special
A	

## TABLE OF CONTENTS

	Page
LIST OF ILLUSTRATIONS . . . . .	ii
LIST OF TABLES. . . . .	iii
INTRODUCTION. . . . .	1
BASIC OBJECTIVES. . . . .	1
BASIC APPROACH. . . . .	1
DATA ACQUISITION PROCEDURES . . . . .	2
Bottom Loss Measurements With AUTOBOUYS. . . . .	2
Seismic Measurements . . . . .	3
Sediment Core Measurements . . . . .	3
SUMMARY OF OPERATIONS . . . . .	3
BOTTOM LOSS DATA PROCESSING PROCEDURES. . . . .	4
Digitization . . . . .	4
Preprocessing Digital Filtering. . . . .	4
Processing for Separated Arrivals. . . . .	4
BOTTOM LOSS RESULTS . . . . .	8
Nature of the Bottom Arrivals. . . . .	8
Quality of Data. . . . .	12
Geometry Dependence of Bottom Loss . . . . .	14
Frequency Variations of Bottom Loss. . . . .	14
Negative Bottom Loss . . . . .	14
Geographical Variations of Bottom Loss . . . . .	15
PRELIMINARY MODELING AND INTERPRETATION . . . . .	15
Empirical Modeling Via Polynomials . . . . .	15
Input Parameters for a Geophysical Model . . . . .	16
SUMMARY AND CONCLUSIONS . . . . .	17
REFERENCES. . . . .	34
APPENDIX A--SOUND SPEED VERSUS DEPTH PROFILES . . . . .	A-1
APPENDIX B--BOTTOM LOSS VERSUS GRAZING ANGLE DATA FOR ALL STATIONS AND FREQUENCIES. . . . .	B-1
APPENDIX C--SIXTH-ORDER POLYNOMIAL REPRESENTATIONS OF BOTTOM LOSS DATA. . . . .	C-1

## LIST OF ILLUSTRATIONS

Figure		Page
1	Operations Area for Hatteras Abyssal Plain Low Frequency Bottom Loss Measurements . . . . .	19
2	Typical Representation of Geometry for Bottom Loss Measurements (Station BL-3) . . . . .	20
3	Block Diagram of Data Processing System for Bottom Loss Measurements . . . . .	21
4	Sequence of Arrivals for a Typical Reception Before and After Filtering Line Components - (Station BL-1, AUTOBUOY No. 2, $\theta_g = 13.0^\circ$ ) . . . . .	22
5	Averaged Direct Path Energy Spectrum (Average Source Depth 909 m) . . . . .	23
6	Example of Signal Enhancement Obtained Using Deconvolution . . . . .	24
7	Consecutive Time Displays of Bottom Arrivals as a Function of Grazing Angle With Respect to Interface Reflected Angle (Station BL-1) . . . . .	25
8	Squared Travel Time Difference Between Subbottom and Ocean Bottom Reflections as a Function of the Cosine Squared of the Ocean Bottom Grazing Angle . . . . .	26
9	Measured and Predicted Travel Time Differences Between Ocean Bottom Reflected and Subbottom Refracted Arrivals . . . . .	27
10	Deconvolved Sediment Interacted Signals Low Pass Filtered at Three Frequencies: 500, 250, and 200 Hz (Site BL-1, Upper Buoy) . . . . .	28
11	Comparison of Bottom Loss Versus Grazing Angle as a Function of Receiver Depth (Station BL-1) . . . . .	29
12	Frequency Variation of Bottom Loss Versus Grazing Angle . . . . .	30
13	Geographical Variations of Bottom Loss Versus Grazing Angle Data (Broadband) . . . . .	31

## LIST OF ILLUSTRATIONS (Cont'd)

Figure		Page
14	Polynomial Fitted and Averaged Broadband Bottom Loss Measured at Three Stations in the Hatteras Abyssal Plain . . . . .	32
15	Geographical Variations in Bottom Loss (Narrowband) . . . . .	33

## LIST OF TABLES

Table		Page
1	Locations and Descriptions of Bottom Loss Measurements . . . . .	2
2	Summary Analysis of Sediments Recovered by Boomerang Core Near Station BL-3 . . . . .	5
3	Summary Analysis of Sediments Recovered by Boomerang Core Near Station BL-2 . . . . .	5
4	Filter Parameters Used In Narrowband Bottom Loss Analysis . . . . .	7

## HATTERAS ABYSSAL PLAIN LOW-FREQUENCY BOTTOM LOSS MEASUREMENTS

### INTRODUCTION

In May and June 1973, low-frequency bottom-loss measurements were conducted at three locations in the Hatteras Abyssal Plain of the Atlantic Ocean by the Acoustic and Environmental Research Division of the Naval Underwater Systems Center (NUSC) and the Lamont-Doherty Geological Observatory (LDGO). This project was designated MAINLOBE (MAJOR INVESTIGATION FOR LOW-FREQUENCY OCEAN BOTTOM-LOSS EXPERIMENT) 73. The text that follows is divided into the topical areas of (1) basic objectives, (2) basic approach, (3) data acquisition procedures, (4) summary of operations, (5) data processing procedures, (6) analysis and interpretation of the bottom-loss measurements, (7) preliminary modeling, and (8) summary of results.

### BASIC OBJECTIVES

The primary objectives of the experiments described in this report are the (1) measurement of ocean bottom loss over a wide frequency range (20-1000 Hz) as a function of grazing angle (5-90 deg) and (2) estimation of sediment acoustic parameters (such as density, sound speed, and attenuation) for sediment interaction modeling and prediction of propagation loss.

### BASIC APPROACH

Three measurement locations, shown within the circled areas in figure 1\* as stations BL-1, -2, and -3, were employed in MAINLOBE to account for possible acoustic variations from changes in bottom topography and structure (both subbottom and bottom interface). Data were collected successfully at each of the three measurement locations. Explosive signals, underwater sound (SUS) charges were used in conjunction with two self-contained, completely automated receiving systems (AUTOBUOYS) to generate and receive the low-frequency wide-band underwater signals.<sup>1</sup>

To enable estimation of sediment acoustic parameters, seismic reflectivity measurements and subbottom profiling were planned along the tracks shown as dashed lines in figure 1. These operations, conducted jointly by personnel from NUSC and LDGO, involved the transmission of acoustic signals generated by air guns and the reception and recording of these signals by means of a towed horizontal receiving array system.<sup>2</sup> Boomerang cores were also planned at locations near the bottom-loss measurements. The positions of the two successful boomerang cores are shown in figure 1.

\*Figures 1 through 15 are presented at the end of the text.

Environmental and oceanographic data in support of the above measurements included:

1. sound speed profiles (SSP) (stations BL-1,-2,-3) and
2. expendable bathythermographs (XBT)

## DATA ACQUISITION PROCEDURES

### BOTTOM-LOSS MEASUREMENTS WITH AUTOBUOYS

The ocean bottom-loss experiments conducted during project MAINLOBE involved the deployment of two AUTOBUOYS, SUS explosive charges, and AN/SSQ-57A or AN/SSQ-41 sonobuoys. An example of the measurement geometry is shown in figure 2 for a typical AUTOBUOY receiver. A primary objective in NUSC's approach to measurement of low-frequency acoustic bottom loss using SUS charges is to obtain time-isolated direct and bottom interaction path arrivals over a wide range of grazing angle. The optimum depths of signal source and receiver for arrival separation were determined from ray-tracing analysis using the Navy Interim Surface Ship Model II (NISSM II) computer model.<sup>3</sup> To study the possible effects of source/receiver geometry on bottom loss measurements, two AUTOBUOYS were deployed at each measurement station. The general measurement procedure consisted of (1) deploying the first AUTOBUOY on station, (2) traversing 2.3 km north, (3) deploying the second AUTOBUOY on station, (4) traversing 32 km north, (5) turning 180 deg, and (6) deploying SUS charges while returning on a due south track to the second AUTOBUOY. The SUS charges were type EX-94(0), containing 816 g tetryl and 31 g primer, set to detonate at 914 m.

Data concerning AUTOBUOY hovering depths, functioning, and minimum/maximum range separation are listed in table 1 for all three measurement stations. The sonobuoys were used to monitor the source level and detonation depth of the explosives and the near range (high grazing angle) bottom path arrivals during the measurement period.

Table 1. Locations and Descriptions of Bottom Loss Measurements

Measurement Station	Latitude	Longitude	Programmed (m) AUTOBUIY Depth*		AUTOBUOY (m) Successful Mission		Minimum Range (km) AUTOBUOY 1, AUTOBUOY 2		Maximum Range (km) AUTOBUOY 1, AUTOBUOY 2	
			No. 1	No. 2	No. 1	No. 2				
BL-1	28°00.0'N	109°10.0'W	3962	3353	Yes	Yes	9.2	3.6	34.9	30.9
BL-2	28°10.0'N	109°10.0'W	3962	3353	No	Yes	-	3.0	-	30.4
BL-3	29°00.0'N	109°10.0'W	3962	3353	No	Yes	-	11.7	-	33.3

\*For actual receiver depths see Appendix A.

Either immediately prior to or following the acoustic measurements, a deep SSP cast was made for each station to a depth of at least 4500 m. These sound speed versus depth profiles are presented in appendix A.

## SEISMIC MEASUREMENTS

The procedure for obtaining wide angle seismic data was to first deploy an air gun and then pay out a buoyant seismic receiving line array (122 m long) from the stern of the research ship as it proceeded at 4 knots. After deployment, the speed of the ship was increased to 6 knots and a sonobuoy was deployed. The acoustic signals generated by the air gun were received by the line array and the sonobuoy and recorded on LDGO's seismic profiling system. The profiling system provides (in situ) some general results concerning the characteristics of the ocean sediment and layer structure. The same data were also recorded on analog tape for further laboratory analysis. Additional information concerning the LDGO seismic data processing procedures can be found in "Physics of Sound in Marine Sediments."<sup>4</sup> An analysis of measurement results is reported in an unpublished work by Houtz and Bryan.<sup>5</sup>

A buoy having a deep (1128 m) hydrophone was also deployed while making the seismic measurements. This acoustic radio buoy (ARAB) is a NUSC innovation consisting of sonobuoy transmitters installed in a spar buoy housing. The ARAB system was used primarily to obtain a measure of the effective low-frequency beam pattern (including the Lloyd mirror effect) of the air gun. Poor signal-to-noise ratio (SNR) of the bottom-interacted signals precluded analysis of the ARAB data to obtain high grazing angle bottom loss results.

## SEDIMENT CORE MEASUREMENTS

Core measurements were made using a Benthos boomerang core.<sup>6</sup> This device is an untethered free-fall corer having a 1.22 m long barrel and an outside diameter of 7.94 cm. The plastic core liner tube, which holds the core sample, is 1.22 m long, has an outside diameter of 7.3 cm, and an inside diameter of 6.50 cm. After the core penetrates the sediment, a trigger releases the barrel from the housing and buoyant glass spheres lift it to the surface with the captured sediment.

## SUMMARY OF OPERATIONS

Only a summary of project MAINLOBE operations is presented herein because daily operations have been reported in detail.<sup>7</sup> Successful bottom-loss measurements were made at all three stations: however, no usable data were obtained from AUTOBUOY No. 1 at stations BL-2 and BL-3 because it malfunctioned.

Seismic measurements were successfully completed along the tracks shown in figure 1. The ARAB was successfully deployed in each of the three areas of seismic profiling; however, low-frequency noise caused by electrical feedback in the ship power line during operation of the air gun compressor degraded the data. Seismic data were not affected by this problem.

Only two of six boomerang cores were successfully retrieved. The first was retrieved at 29° 06.8'N, 70° 30.0'W, near station BL-3. The other was retrieved at 28° 36.5'N, 70° 24.5'W, near station BL-2. A summary analysis of the data is presented in tables 2 and 3.

### BOTTOM-LOSS DATA PROCESSING PROCEDURES

The basic approach to the measurement and processing techniques employed at NUSC for the determination of ocean bottom loss has been previously documented. 8,9,10 A summary of these procedures and the special processing techniques required is described below.

#### DIGITIZATION

As shown in figure 3, data from two of the three available staggered-gain AUTOBUOY analog tape channels were passed through a 750-Hz low-pass filter, digitally sampled, and stored on magnetic tape using a UNIVAC 1230 computer system. To compensate for record and/or reproduce tape-speed variations, external sampling commands were generated from a 1000-Hz time code carrier (also recorded on the AUTOBUOY analog data tape) via a phase-locked frequency multiplier. A sampling rate of 3000 Hz, which exceeds the Nyquist sampling criterion rate by a factor of 2, was used to facilitate deconvolution processing of the data.

#### PREPROCESSING DIGITAL FILTERING

Following digitization, contaminating interference caused by alternating current components during playback of the AUTOBUOY analog tape was removed by digital filtering. A digital filter was designed to pass all frequencies except the narrowband alternating current line components. In figure 4, a typical sequence of arrivals prior to and following the line component filtering is shown.

#### PROCESSING FOR SEPARATED ARRIVALS

##### Bottom Loss Calculation

The determination of bottom loss for any given explosive detonation was accomplished by using

$$B_L = (R_D - R_B) + (N_D - N_B), \quad (1)$$

where

$B_L$  = bottom loss (dB),

$R_D$  = received energy in direct arrival (dB),

Table 2. Summary Analysis of Sediments Recovered  
by Boomerang Core Near Station BL-3

Depth (cm)	Sound Speed* (m/s)	Bulk Density (g/cm <sup>3</sup> )	Impedance (10 <sup>3</sup> .g/cm <sup>2</sup> /s)
Interface	1608	1.11	1.785
15.2	1600	1.11	1.776
30.5	1637	1.11	1.817
45.7	1603	1.15	1.843
57.2	1637	1.15	1.883
Average	1617	1.13	1.827

\*Corrected to seafloor in situ conditions.

Table 3. Summary Analysis of Sediments Recovered  
by Boomerang Core Near Station BL-2

Depth (cm)	Sound Speed* (m/s)	Bulk Density (g/cm <sup>3</sup> )	Impedance (10 <sup>3</sup> g/cm <sup>2</sup> /s)
Interface	1609	1.33	2.140
3.8	1584	1.33	2.107
12.7	1616	1.33	2.149
29.4	1616	1.33	2.149
41.2	1621	1.20	1.945
Average	1609	1.30	2.092

\*Corrected to seafloor in situ conditions.

$R_B$  = received energy in bottom-interacting arrival (dB),

$N_D$  = propagation loss over direct path (dB), and

$N_B$  = propagation loss over bottom-reflected path (dB).

As is evident from the above expression, the procedure for calculating bottom loss is comparative and self-calibrating in that only the relative energy difference between the direct and bottom interacting arrivals need be experimentally determined. The corresponding propagation loss within the water column for the two arrivals is determined using a NISSM II computer ray-tracing program.<sup>3</sup> The input parameters for NISSM II were (1) in-situ measured water SSP, (2) water depth, and (3) the depths of the signal source and of the receiver. In computing the propagation loss for the bottom-reflected path, the computer program assumes a flat, single-layer, zero-loss (totally reflecting) ocean bottom. NISSM II also provided an accurate estimate of the grazing angle for each bottom-reflected arrival, as discussed below.

An analog reconstruction of the digitally sampled data (after preprocessing filtering) is shown in the lower trace of figure 4, where the four arrivals resulting from the detonation of a single explosive are clearly separated in time. The direct, bottom, and surface-reflected arrivals are isolated\* via a UNIVAC 1108 computer program by using an energy threshold criterion.<sup>9,10</sup> The program then computes the time separation and pulse duration of the various arrivals. Furthermore, each arrival is partitioned and increased in duration by appending zeros to it. The time extension of the digital data is required to satisfy the response time of the recursive digital filters centered at the lower frequencies. Following partitioning, the energy in each arrival is computed by squaring and summing its digital time series after filtering for the frequency band of interest.

#### Bandwidths and Center Frequencies

The center frequencies of the recursive filters were chosen to match the peaks of the measured direct path energy spectrum. A measured energy spectrum, which was averaged from 20 SUS charges detonated within  $909 \pm 26$  m, is shown in the upper half of figure 5 with the center frequencies and bandwidths of the recursive bandpass filters. The geometric center frequency, bandwidth, and upper and lower effective frequency limits for each recursive filter are listed in table 4. The digital recursive filters were five-pole Butterworth filters.<sup>11</sup>

The AUTOBUOYS used in this experiment were outfitted with processing frequency pre-emphasis. In the experiment conducted prior to MAINLOBE, the AUTOBUOYS had been used for ambient noise measurements in which amplifier gain variation with a frequency range in the 20 to 1000 Hz regime is useful. Time did not permit the removal of the frequency pre-emphasis

\*The upper water refracted arrival (resulting from a path totally refracted near the ocean surface) was also isolated for identification, but was not processed.

circuit prior to the MAINLOBE measurements. The effect of the pre-emphasis amplifier has been removed for the spectrum shown in the lower half of figure 5. The combined effects of the preemphasis amplifier and the alternating current line interference filtering resulted in an effective broadband of 90 to 790 Hz. Note that although an anti-aliasing analog filter with a 750 Hz cutoff frequency was used, the pre-emphasis amplifier effectively increased the cutoff frequency to 790 Hz.

Table 4. Filter Parameters Used in Narrowband Bottom Loss Analysis

Center Frequency (Hz)	Bandwidth (oct)	Frequency Bounds of 3-dB Passband (Hz)	
100	1/7	95.1	105.1
177	1/3	157.7	198.7
252	1/3	224.5	282.9
325	1/3	287.4	367.5
445	1/3	396.4	499.5
600	1/3	534.5	673.5
745	1/6	703.2	789.3

Accuracy of Propagation Loss and Bottom/Grazing Angle Determination

As mentioned previously, the direct-path and bottom-reflected path propagation losses, together with the corresponding bottom grazing angle for each explosive detonation, were determined by use of the NISSM 11 computer ray-tracing program. To reduce the required amount of computer storage and program processing time, polynomial expressions were fitted to the NISSM 11 output tabulations.<sup>9</sup> Polynomials were generated as a function of horizontal range between the signal source and the receiver for (1) the propagation loss of each path and (2) the grazing angle for the bottom interacted path. To obtain two independent determinations of horizontal range separation, two additional polynomial functions were generated. The first was a function of time separation between the direct and bottom interacted arrivals and the second was a function of time separation between the direct and surface reflected arrivals.

Thus, for each detonation, two independent estimates of range were determined. These range estimates corresponded to the time separation intervals of the direct path and surface-reflected path arrivals and the direct path and bottom-reflected path arrivals. The arithmetic mean of the two range estimates was then used in estimating the remaining parameters (such as grazing angle) from the evaluation of the corresponding polynomial expression. For 95 percent of the data, the difference between the mean horizontal range and its two associated values was less than  $\pm 5$  percent. The remaining 5 percent of the data had no more than  $\pm 10$  percent range error. These differences result from differences between the actual and the assumed detonation depth.

For range differences of less than  $\pm 5$  percent, the maximum variation in bottom grazing angle was  $\pm 0.6$  deg and the maximum variation in propagation loss was  $\pm 0.2$  dB. For range differences of less than  $\pm 10$  percent, the maximum variation in bottom grazing angle was  $\pm 1.3$  deg and the maximum variation in propagation loss was  $\pm 0.4$  dB.

The above procedure was modified at ranges where the upper water-refracted arrivals could no longer be time isolated from the surface-related arrival. When this occurred, range was computed only from the separation between the direct and bottom pulses. This situation arose only for horizontal range separations greater than 28 km, corresponding to reflection grazing angles of less than 9.5 deg. Generally, the upper refracted path appeared only at horizontal ranges greater than 24 km.

The source level for each SUS charge detonation was computed by adding the direct path arrival broadband energy to the value of energy lost along the direct path as predicted by NISSM 11. The prediction from NISSM 11 is used in conjunction with a broadband energy measurement; however, this does not present a problem because sensitivity studies showed that there is little frequency dependence in propagation predictions throughout the 90 to 790 Hz band over the range of 0 to 36 km for the source/receiver geometry employed. If the SUS source level were constant, the computed source level would also be constant with range, providing that the propagation prediction is correct. For this experiment, the average standard deviation of the computed source level was less than  $\pm 0.8$  dB for all of the data. It was necessary to correct the NISSM 11 propagation prediction over a brief range interval for stations BL-1 and -3. This range generally occurred around the region where the direct path arrived at the ALTOBODY at approximately  $0^\circ$ , the path's turning region. This interval was generally less than 2 km and only occurred at ranges greater than 22 km. The correction was made by altering the NISSM 11 prediction over the problem range interval until the computed source level was statistically equal to mean source levels computed at the other ranges.

#### BOTTOM LOSS RESULTS

A complete set of bottom loss versus grazing angle curves for the data obtained at all three stations is contained in appendix B. Certain aspects of the results have been previously reported.<sup>8,9</sup> For the purpose of completeness they are included in the following discussion. To provide insight into the nature and characteristics of the bottom loss curves, the time series structure of the bottom interaction arrival is discussed first.

#### NATURE OF THE BOTTOM ARRIVALS

The complicated time series structure of a received explosive signal that has interacted once with the ocean bottom can be simplified through the use of deconvolution. The deconvolution process is used to determine the ocean bottom impulse response, thereby, eliminating interference effects of the explosive's bubble pulses.

The method of frequency domain deconvolution has been applied to the analysis of bottom interacted signals when the acoustic source is an explosive.<sup>8,10,12,13</sup> A simplified mathematical description of the deconvolution process employed at NUSC is represented by

$$h(t) = F^{-1} \left\{ \frac{Y(f) X^*(f)}{|X(f)|^2 + A} G(f) \right\}, \quad (2)$$

where

- $h(t)$  = impulse response of the ocean bottom,
- $X(f)$  = Fourier transform of input signal (direct arrival),
- $Y(f)$  = Fourier transform of output signal (bottom arrival),
- $A$  = additive white noise constant, and
- $G(f)$  = Gaussian filter function

and where the operators  $F^{-1} \{ \cdot \}$  and  $X^*$  denote, respectively, the inverse Fourier transform and the complex conjugate of the Fourier transform of the input signal. As described in a recent report,<sup>8</sup> a Gaussian filter function was used in the process to improve the SNR and a small fraction of white noise was added to the direct arrival spectrum (denominator) to enhance the stability of the transfer function.<sup>8</sup> Since the Fourier transform of the impulse response represents the frequency function, the base ten logarithm of the magnitude squared of the quantity within the brackets of equation (2) is, in actuality, the ocean bottom loss as a function of frequency. However, to obtain a value of the transfer function, this quotient must be normalized by a factor equivalent to the difference in propagation losses associated with the two signals (i.e., the direct and bottom arrivals).

The effect of deconvolution can be seen in figure 6. The upper trace is representative of a typical noise-filtered reception. The shock and bubble pulses of the direct arrival are clearly defined. Because of bubble pulse interference, it is possible to identify only the reflection from the ocean bottom interface boundary. However, in the deconvolved time series shown in the lower trace, interference from bubble pulses has been eliminated by transforming the acoustic waveform of the direct arrival of the explosive source into a delta function. Thus, the direct path arrival appears as a single spike. As such, additional receptions (representing the subbottom response to a delta function impulse stimulus) can be seen in this deconvolved trace.

An approach to identifying the mechanisms that produce the subbottom arrivals is shown in figure 7. In this figure, the time series of bottom interacted arrivals are displayed for eight consecutive values of the bottom interface reflection angle. Consecutive receptions are "stacked" along the ordinate as a function of water-sediment interface grazing angle. The unprocessed data are shown on the left and the deconvolved data are shown on the right. The deconvolved signals were low-pass filtered by a Gaussian filter with 3-dB cutoff frequency at 250 Hz. Although the existence of subbottom arrivals is evident in the unprocessed data, their presence is distorted by interference from the bubble pulses. With the elimination of this interference via deconvolution and the formation of the time history display, the trend in the relative time displacement of the subbottom arrivals as a function of grazing angle becomes more apparent.

Subbottom Reflection

The first subbottom arrival (see figure 7) was thought to be a reflection from a subbottom layer. If the layer thickness is assumed constant and independent of range and the sound speed within the layer is also assumed constant, then the layer thickness and sound speed of the layer can be computed. Let " $\Delta t$ " be the travel time difference obtained by subtracting the travel time of the signal reflecting from the top of the layer (the water/sediment interface) from the travel time of the signal reflecting from the bottom of the layer. Let " $\theta_g$ " be the grazing angle at the water/sediment interface. When the sediment layer is thin with respect to the water layer, it can be shown that

$$(\Delta t)^2 = \left(\frac{2h}{c_s}\right)^2 - \left(\frac{2h}{c_w}\right)^2 \cos^2 \theta_g, \quad (3)$$

where

$h$  = sediment layer thickness,

$c_w$  = sound speed of water at the water/sediment interface,

$c_s$  = sound speed of sediment layer, and

$\theta_g$  = grazing angle at water/sediment interface.

Letting

$$y = (\Delta t)^2,$$

$$b = \left(\frac{2h}{c_s}\right)^2,$$

$$x = \cos^2 \theta_g, \text{ and}$$

$$m = -\left(\frac{2h}{c_w}\right)^2,$$

Equation 3 can then be expressed as the linear equation,

$$y = mx + b. \quad (4)$$

Figure 8 shows measured values of  $(\Delta t)^2$  versus  $\cos^2 \theta_g$  for 45 points at site BL-1 over a range of 16.9 to 47.6 deg grazing angle. A least squares linear fit was computed and resulted in values of  $h = 20.6$  m and  $c_s = 1580.4$  m/s. A comparison of these results with those from the boomerang cores and archival data will be discussed later in this report.

Subbottom Refraction (see figure 7)

The second subbottom arrival behaved in a manner peculiar to a refracted rather than reflected, signal. The refracted signal did not occur at the higher grazing angles, but emerged at 26 deg grazing and converged with the first subbottom reflected signal as the grazing angle decreased. This behavior is characteristic of an acoustic signal traveling along a path through a medium whose SSP increases with depth.

The LDGO wide angle seismic measurements made during the experiment verified the existence of a sound-speed gradient in the sediment. Bryan and Houtz<sup>5</sup> report that the velocity in the upper 250 m of sediment can be expressed as

$$V(t) = V_0 + Kt, \quad (5)$$

where

$$V_0 = 1.52 \text{ km/s},$$

$$K = 2 \text{ km/s}^2, \text{ and}$$

where  $t$  is the one way travel time of an acoustic signal propagating downward at normal incidence from the ocean/sediment interface. Equation (5) can be reexpressed so that sound speed is a function of depth rather than of time:

$$V(z) = V_0 \left( 1 + \frac{2K}{V_0^2} z \right)^{1/2}, \quad (6)$$

where  $z$  = depth.

When the term  $\frac{2K}{V_0^2}$  is small, equation (6) may be expanded as a

Taylor series, with terms of order 2 and higher removed:

$$V(z) = V_0 + gz \quad (7)$$

where

$$g = \frac{K}{V_0}$$

For the values previously given, equation (7) is a reasonable approximation (2 percent error in sound speed to a depth of 300 m).

Travel time differences between the refracted and ocean/sediment interface reflected signals were measured for 29 points over a grazing angle range of 14 to 26 deg at station BL-1. These values were compared with predictions obtained using the Continuous Gradient Ray Tracing System II (CONGRATS II) ray trace program.<sup>14</sup> The SSP was given by equation (5), where  $V_0 = 1.52$  km/s and  $K = 2$  km/s<sup>2</sup>. Although modeled prediction agreed reasonably well with the data, a better fit was obtained by accounting for the previously discussed constant velocity layer and modifying the parameters  $V_0$  and  $K$ . The modified values of  $K$  and  $V_0$  are

$$K = 2.16 \text{ km/s}^2,$$

$$V_0 = 1.6 \text{ km/s, and, therefore,}$$

$$g = 1.35 \text{ s}^{-1}.$$

Figure 9 shows the measured and predicted refraction/reflection travel time differences as a function of reflection grazing angle.

#### Frequency Dependence of Apparent Acoustic Sediment Layers

The above description of a relatively simple sediment structure consisting of a 20.6 m constant-velocity layer overlaying a sediment whose speed increases linearly with depth was obtained from analysis of deconvolved sediment interacted signals that were low-pass filtered at 250 Hz. As the frequency passband is widened, the apparent acoustic sediment structure becomes more complex. This observation is illustrated in figure 10. Filtered deconvolved sediment interacted signals are shown for five reflection grazing angles. The signal from the first subbottom reflector, which is clearly seen when filtered at  $f_c = 500$  Hz, reduces to background noise at a cutoff frequency of 200 Hz. When the filtering frequency is 250 Hz, signals from two subbottom reflectors can be seen. However, as the grazing angle decreases, signals from the first subbottom reflector become weaker and vanish into background noise, while those of the second reflector remain significant. This is the reflector associated with the 20.6 m constant-speed layer previously described.

#### QUALITY OF DATA

The quality of experimental measurements can be degraded by systematic and random errors. Systematic error, generally characterized by biased measurements, can be minimized through prudent experiment design and data analysis. Random error, however, results from the presence of noise in the data and is usually unavoidable.

The experimental methodology requiring time-isolated bottom and direct path arrivals eliminates, or greatly reduces, certain forms of systematic and random errors inherent in the measurement of bottom loss. In particular, errors caused by multipath interference and improper source level estimates are eliminated.<sup>8,15,16</sup> Errors attributed to improper estimation of SUS detonation can also be significantly reduced.

One measure of the magnitude of random error in the data measurement is the SNR, defined here as:

$$\text{SNR} = 10 \log_{10} \frac{I_S}{I_N} \quad , \quad (8)$$

where

$I_S$  = intensity of signal and  
 $I_N$  = intensity of noise.

Because the direct and bottom interacted signals can never be truly separated from noise interference, a modified SNR ( $\text{SNR}_m$ ) is defined as

$$\text{SNR}_m = 10 \log_{10} \frac{I_{S+N}}{I_N} \quad , \quad (9)$$

where

$I_{S+N}$  = intensity of signal plus noise

A noise sample was recorded prior to the detonation of each SUS charge. From these samples, intensity levels were computed in all the processing frequency bands. Thus, for all bottom loss measurements, a signal-plus-noise to noise ratio could be computed in all frequency bands for the direct and bottom interacted arrival. The  $\text{SNR}_m$  for the bottom interacted arrival was always less than that for the direct path arrival. For the processing bands centered at 177, 252, 325, 445, 600, and 745 Hz, the bottom-interacted arrival  $\text{SNR}_m$  was, on the average, 11 dB or greater. The  $\text{SNR}_m$  was approximately 9 dB in the broadband. For the narrowband centered at 100 Hz, the average  $\text{SNR}_m$  was less than 4 dB. This lower value results because (1) the source signal spectrum level decreases rapidly for frequencies less than the bubble pulse frequency of 151 Hz (see figure 5), (2) the noise spectrum increases with decreasing frequency, and (3) there is a large variance in the low frequency noise resulting from the short time duration (approximately 45 ms) of the arrivals. With the exception of the 100 Hz data, the relatively good SNRs are demonstrated by the "closeness of fit" of the individual data points to the three points moving average curve shown in the bottom loss data in appendix B.

## GEOMETRY DEPENDENCE OF BOTTOM LOSS

The effect of source/receiver geometry on bottom loss measurements can be observed in the data acquired at station BL-1. A receiver (AUTOBUOY No. 1) at 3658 m and a second receiver (AUTOBUOY No. 2) at 3200 m recorded the acoustic signals from the explosive charges detonated at 914 m. Simultaneous water/sediment grazing angle coverage exists over the range of 8 to 34 deg. In figure 11, bottom loss computed from the 3200 m receiver (solid line) and the 3658 m receiver (dashed line) are compared for two frequency bands. In both bands, the correlation between receivers is excellent. In both bands, between the 8 to 30 deg range the two curves are identical to a high degree of statistical confidence. This agreement is significant because for each data point, at a given grazing angle, the bottom loss from the lower buoy was acquired using a different SUS charge from that used to acquire the bottom loss from the upper buoy. Furthermore, the area of sediment interaction resulting in the bottom loss data point at a given grazing angle is different for each buoy. Thus, the bottom/subbottom structure seems to be independent of range for at least short distances (4.6 km or less). Also, the travel time differences between the subbottom and bottom arrivals are nearly the same for both buoys. An analysis of ray angles, using the model profile given in figure 9, confirmed that the bottom/subbottom arrival structure was nearly identical between the two buoys for a given reflection grazing angle. Thus, a geometrically dependent bottom loss, to the extent previously reported<sup>8</sup> (where the separation between receivers was a greater percentage of water depth), did not occur.

## FREQUENCY VARIATIONS OF BOTTOM LOSS

An example of typical frequency variations of bottom loss versus grazing angle is shown in figure 12. The dashed line represents the 3 point moving average at a center frequency of 177 Hz and the solid line represents the 3 point moving average at a center frequency of 745 Hz. For all three stations the bottom loss generally decreased with increasing frequency for grazing angles of 25 deg or greater, and tended to increase with increasing frequency for grazing angles of 25 deg or less.

The oscillations in bottom loss versus grazing angle seen in figures 11 and 12, and throughout the narrowband bottom loss curves in appendix B, are a result of spatially complex interference patterns created by the interaction of acoustic energy with the ocean bottom. The broadband processed data (90-790 Hz) tends to average-out the narrower frequency band effects; therefore, the oscillating patterns are greatly reduced.

## NEGATIVE BOTTOM LOSS

The 3 point moving average curve centered at 177 in figure 12 shows the occurrence of negative bottom loss over the grazing range of 8 to 20 deg. Negative bottom loss was observed in about 75 percent of the 3 point moving average curves computed. As can be seen in appendix B, with the exception of data centered at 100 Hz, the level of negative bottom loss rarely exceeds -2 dB, occurs only intermittently, and generally is not observed for grazing

angles of 20 deg or greater. The observance of negative bottom loss has been reported recently in other ocean bottom acoustical investigations and has been attributed to the use of the Rayleigh reflection model in the reduction of the data.<sup>8,9</sup> This model does not account for both refracted and non-plane wave reflected path signals that have been shown to exist in the data.<sup>8,9,17</sup> This interaction was previously described and is illustrated in figures 7 and 10. For the data reported here, negative bottom loss is apparent in the narrow bands, but is insignificant in the broadband where the effect has been averaged out because of the frequency diversity of the wider band.

#### GEOGRAPHICAL VARIATIONS OF BOTTOM LOSS

A comparison of the broadband bottom-loss versus grazing angle data obtained at all three geographical locations is presented in figure 13. At station BL-1, the data are representative of the combined results of the two AUTOBUOY receiving systems. The bottom-loss values at the three locations are in excellent agreement over the entire measurement range. Because of this close agreement, the broadband data from all three locations, representing 394 data points, were smoothed and fitted. These data are shown in figure 14, where the solid line represents a 6th order least square polynomial fit to the 394 data points. The dots represent the data averaged in 5-deg bins centered at  $2.5 + 5n$  deg,  $n = 1, 2, \dots, 12$ . The averaging was computed in linear space. Upper and lower bounds of one standard deviation have been applied to the averaged data. The largest value of the standard deviation was 1.1 dB. Thus, the broadband bottom loss is characterized by a loss of 5 dB at 62.5 deg, gradually rising to a maximum of about 7 dB at 37.5 deg, and then smoothly decreasing to a minimum of approximately 1.3 dB around 7.5 deg.

There was less agreement in the narrowband bottom-loss data between the three locations. This is attributed to slight changes in subbottom structure affecting the complex frequency relationships in the interaction of bottom and subbottom arrivals. The comparison of bottom loss at 177 and 745 Hz for all three locations is shown in figure 15. Variations of up to 10 dB can be observed.

#### PRELIMINARY MODELING AND INTERPRETATION

Two separate methodologies can be applied to the problem of modeling the bottom-loss measurements for the Hatteras Abyssal Plain. Since both empirical and geophysical models have advantages and disadvantages, this dual approach is necessary.

#### EMPIRICAL MODELING VIA POLYNOMIALS

The goal of empirical modeling is to approximate the data by a numerical function. This method can usually be implemented in a straight forward manner. However, it offers no explanation of the mechanisms that cause the bottom loss. Thus, the model cannot be extrapolated beyond the range of the

data. The bottom loss data in this report have been fitted to 6th order polynomials. Tabulations and illustrations of the resultant polynomial expressions are contained in appendix C. The polynomials allow the modeler to compute bottom loss in decibels as a function of grazing angle for each frequency band of each buoy at each station, for the combined buoys at station BL-1, and for the combined data of the three stations (BL-1, -2, and -3).

#### INPUT PARAMETERS FOR A GEOPHYSICAL MODEL

A geophysical model attempts to simulate mechanisms causing bottom loss. The model requires a theory adequate to explain the interaction of acoustic pressure in the bottom and subbottom. These types of models require input parameters such as the sediment thickness, density, attenuation, sound speed, and sound-speed gradient of each effective subbottom layer.

Some of the parameters that could be used to model the bottom loss at station BL-1 have been derived. A brief discussion of these parameters and variations in their measurement follows.

The central region of the Hatteras Abyssal Plain is characterized by silts interstratified with clay.<sup>18</sup> The total sediment overlaying the basement is approximately 2.1 km, which is considerably thicker than the average 1-km sediment thickness in the North Atlantic.<sup>19</sup>

Earlier in this report (see figure 9) a partial geophysical description of the subbottom was given, describing it as consisting of a layer of constant velocity sediment overlaying a layer where sound speed increased linearly with depth. The speed of sound computed for the first layer was 1580 m/s. For the same area, Horn, et al., report<sup>18</sup> an average sound speed computed from a mean grain size of 1572 m/s (corrected for depth and temperature) in the upper 3.5 m of sediment. The two values of sound speed averaged from the boomerang cores to the north of station BL-1 were higher (1617 and 1609 m/s). The average sediment densities measured from the cores were 1.13 and 1.30 gm/cm<sup>3</sup>. Horn et al. predicted<sup>18</sup> a density of 1.77 gm/cm<sup>3</sup>. The second sediment layer was characterized by the linear-with-depth SSP:

$$V(z) = V_0 + gz \quad (10)$$

where

$$V_0 = 1600 \text{ m/s,}$$

$$g = 1.35 \text{ s}^{-1}, \text{ and}$$

where  $z$  is the depth in meters referenced to the boundary with the first sediment layer. This description is valid to a depth of approximately 145 m below the water/sediment interface, as this was the turning depth of the deepest refracted ray measured.

The linear-with-depth gradient can be compared with averaged seismic measurements. As previously discussed, the seismic measurements describe the velocity in the sediment as linear with reflection time,  $T$ , referenced to the water/sediment interface. The expression for all seismic tracks was given in equation (5). Following the approximations discussed in equations (5) and (6) a  $K$  of  $2 \text{ km/s}^2$  can be approximated by a  $g$  of  $1.32 \text{ s}^{-1}$ . Houtz<sup>20</sup> has indicated that a value of  $V_0 = 1.52 \text{ km/s}$  may be unrealistically low for Abyssal Plain turbidities and, hence, alternate values of  $V_0 = 1.55 \text{ km/s}$  and  $k = 1.75 \text{ km/s}^2$  should be used. This would lead to an approximate linear (with depth) gradient of  $1.11 \text{ s}^{-1}$ . Boomerang core data and deconvolved records tend to support the alternate value of  $V_0$ . Seismic measurements are made using methods yielding good results at depths deep in the sediments, but are less accurate at and near the ocean/bottom interface. The best resolution available in the MAINLOBE seismic measurements is approximately 200 m. The parameters derived from the deconvolved signals have much finer resolution (roughly 5 m), but are only valid to about 145 m below the ocean/sediment interface.

#### SUMMARY AND CONCLUSIONS

Project MAINLOBE ocean-bottom-loss experiments conducted by NUSC and LDGO in the Hatteras Abyssal Plain of the Atlantic Ocean have been reported and the results have been presented in their entirety. Five significant observations arising from the analysis of these results are that:

- Bottom loss measurements were acquired using a self-calibration technique in which direct and bottom arrivals were time isolated from all other arrivals, thereby precluding multipath interference. As a result, the data exhibited excellent agreement over adjacent but independent measurements.
- Time coincident interaction of the ocean-bottom reflection and refractions, which are not ascribed by the Rayleigh model in the reduction of the acoustic data, resulted in negative values of bottom loss over a limited range of frequencies and grazing angles.
- A vertical change of 358 m in receiver depth had little measurable effect on the bottom loss results for the geometry and environmental conditions encountered during these experiments.
- Broadband (90-790 Hz) bottom loss from the three stations, spaced over an interval of 1 deg of latitude, showed considerable similarity. A smoothed curve of the combined stations broadband bottom loss had a standard deviation of the order of 1 dB.
- Narrowband (1/3 octave or less) bottom loss showed less similarity between stations. This effect is the result of small changes in sediment layer structure between stations.

In addition, bottom-interacted arrivals at station BL-1 were deconvolved to obtain the sediment impulse response, resulting in the isolation and identification of reflected and refracted arrivals. A geophysical description of the subbottom was abstracted from studies of subbottom/bottom arrival time differences as a function of grazing angle. For frequencies less than 250 Hz, this description consisted of a 21 m constant sound speed layer overlaying a layer where sound speed increases linearly with depth. The derived sound speed gradient ( $1.35 \text{ s}^{-1}$ ) of this layer was similar to the equivalent gradient ( $1.11 \text{ s}^{-1}$ ) obtained by concurrent independent seismic studies.

The above geophysical description can be used as an input to a bottom loss model. The output of such a model can then be validated by comparison with the bottom loss results reported for station BL-1. Because of the significant contribution of the subbottom reflections and refractions, it is recommended that the bottom loss model use the geophysical description of a layered bottom with sound speed gradients.

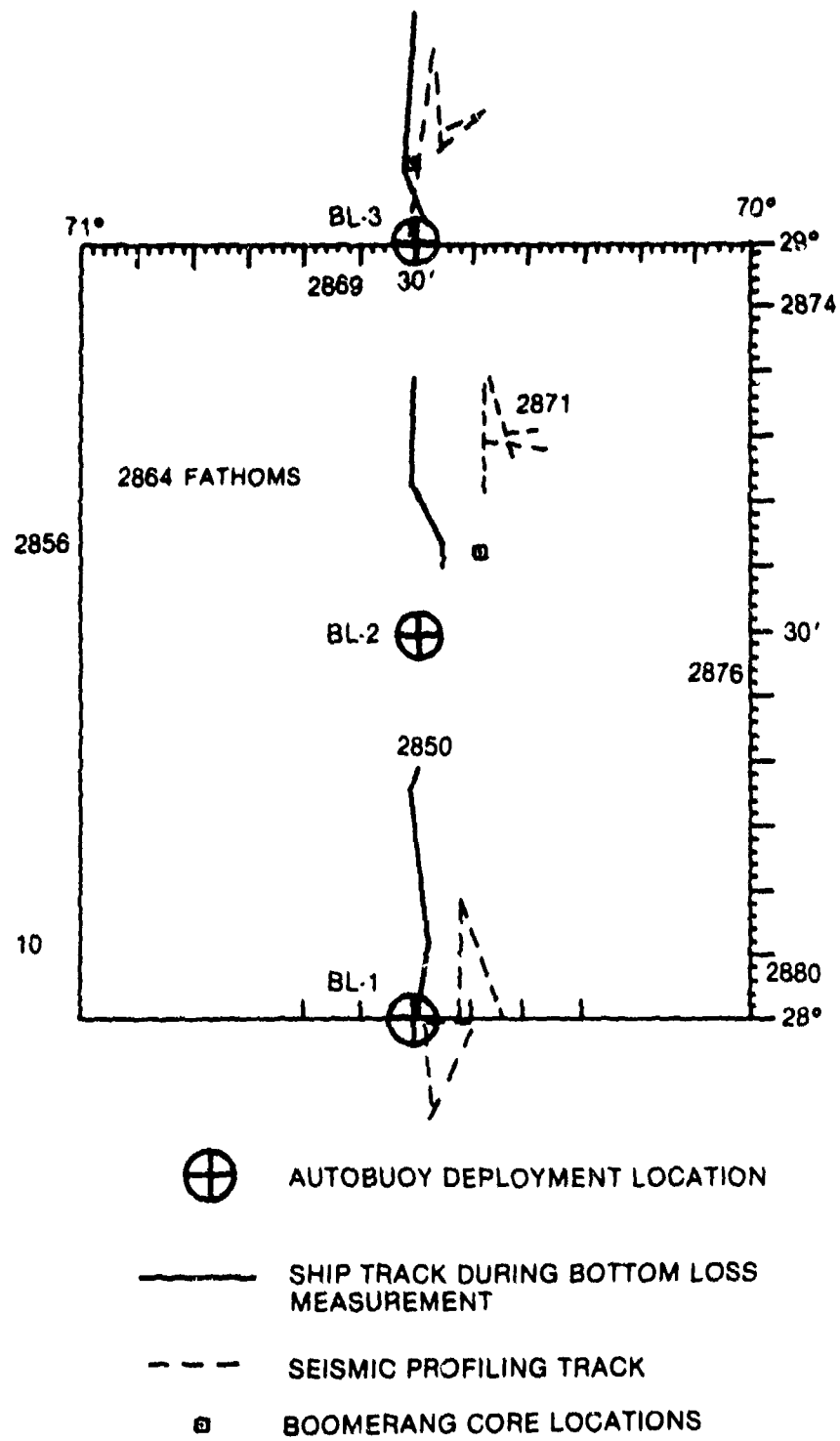


Figure 1. Operations Area for Hatterus Abyssal Plain Low Frequency Bottom Loss Measurements

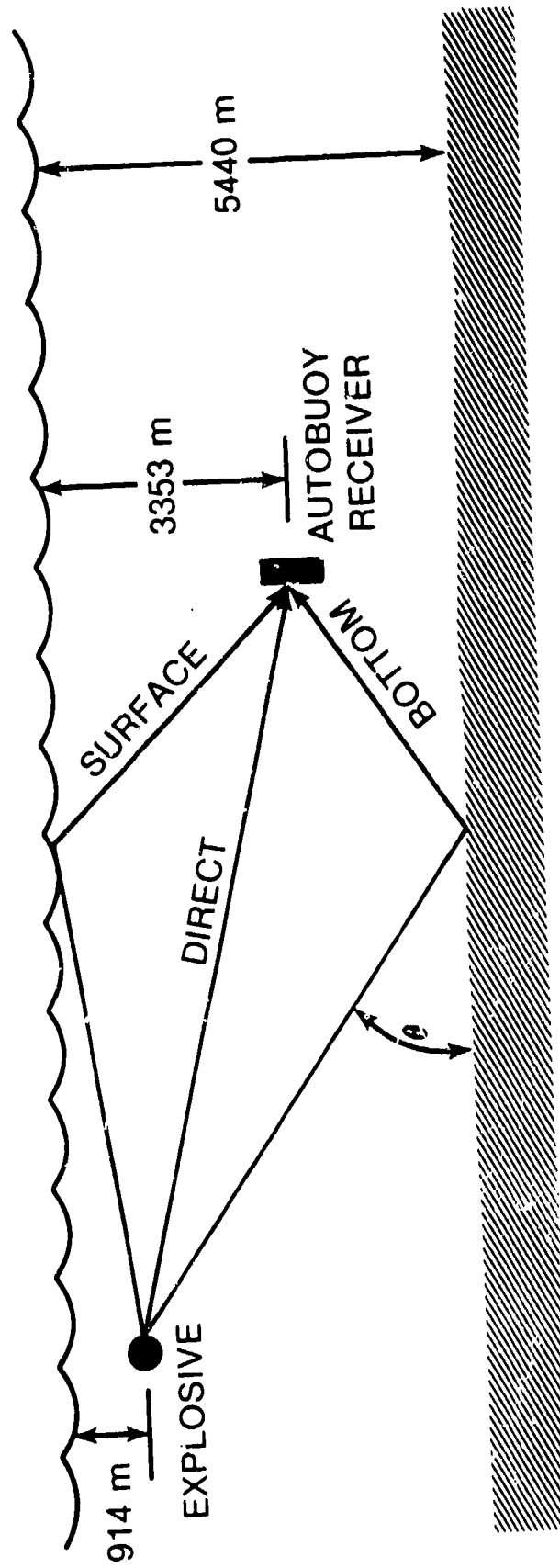


Figure 2. Typical Representation of Geometry for Bottom Loss Measurements (Station BL-3)

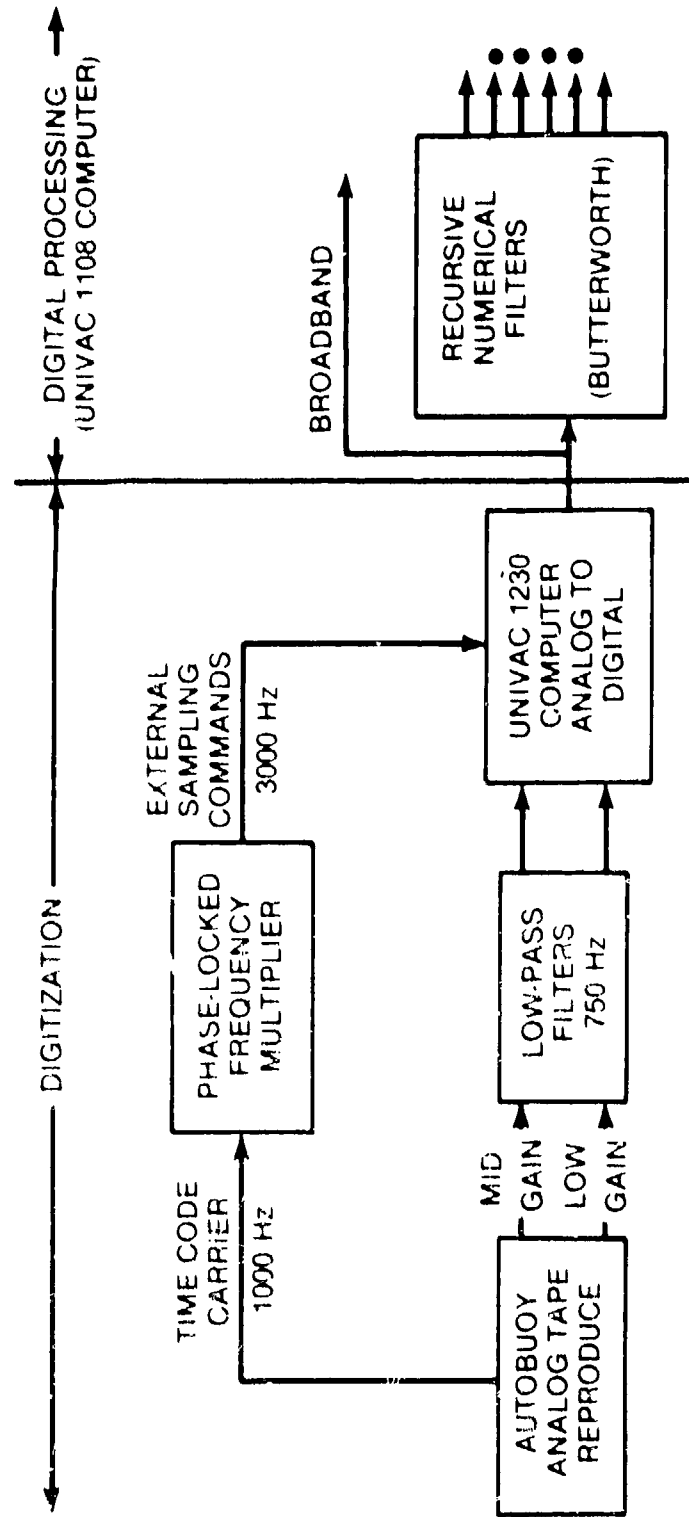


Figure 5. Block Diagram of Data Processing System for Bottom Loss Measurements

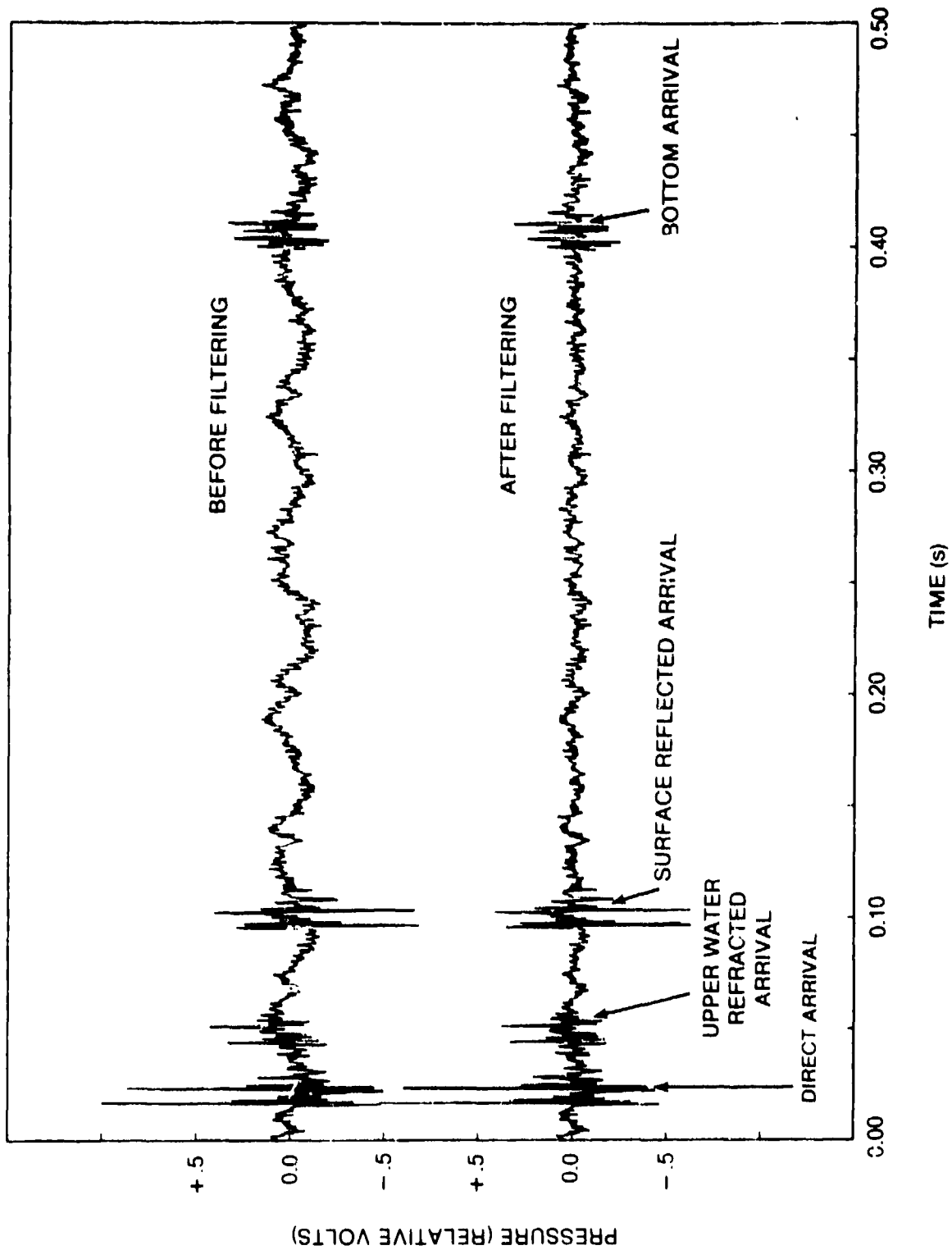


Figure 4. Sequence of Arrivals for a Typical Reception Before and After Filtering Line Components - (Station BL-1, AUTOBUOY No. 2,  $\theta_g = 13.0^\circ$ )

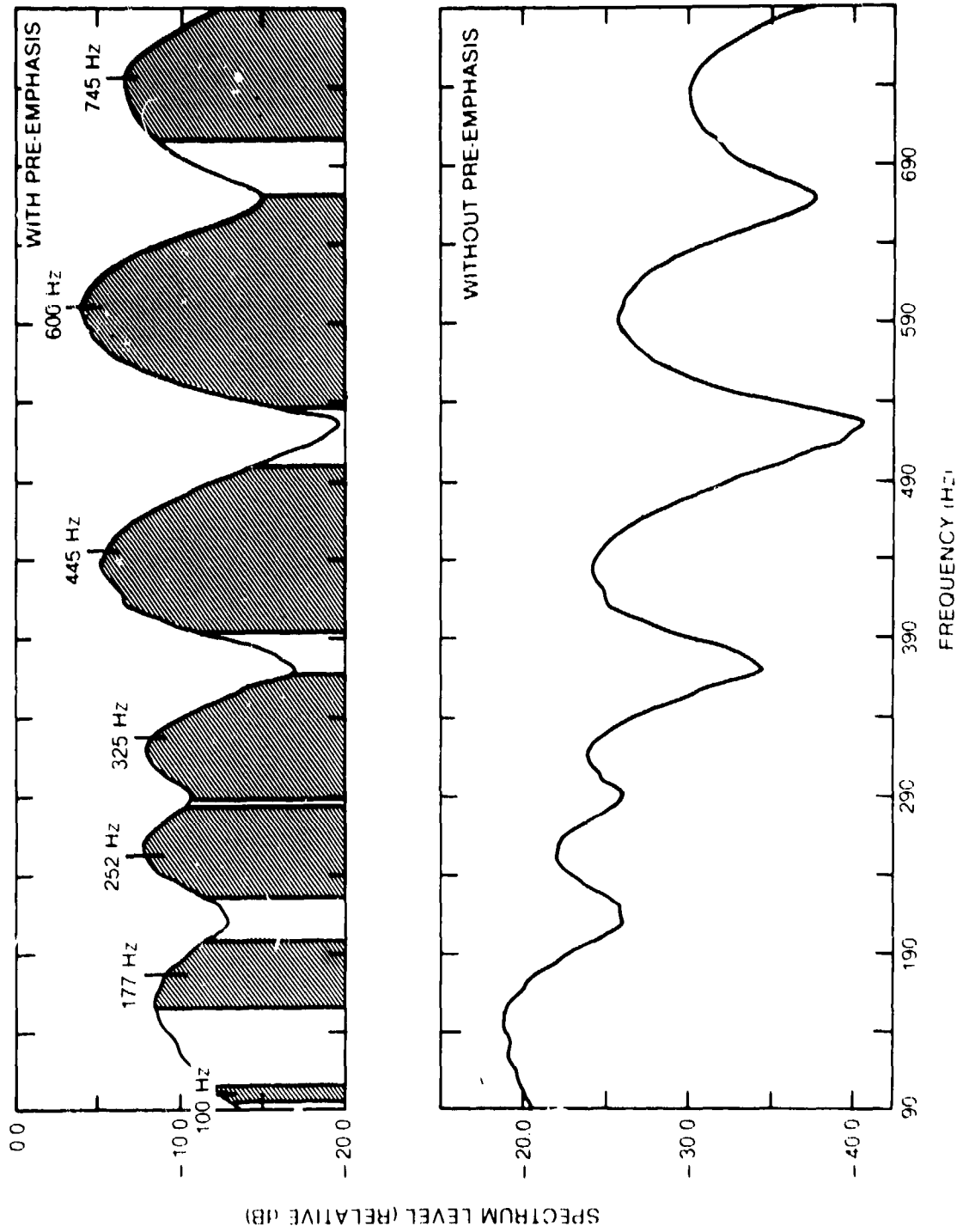


Figure 5. Averaged Direct Path Energy Spectrum (Average Source Depth 909 m)

SITE BL-1 UPPER BUOY  $\theta_g = 13^\circ$

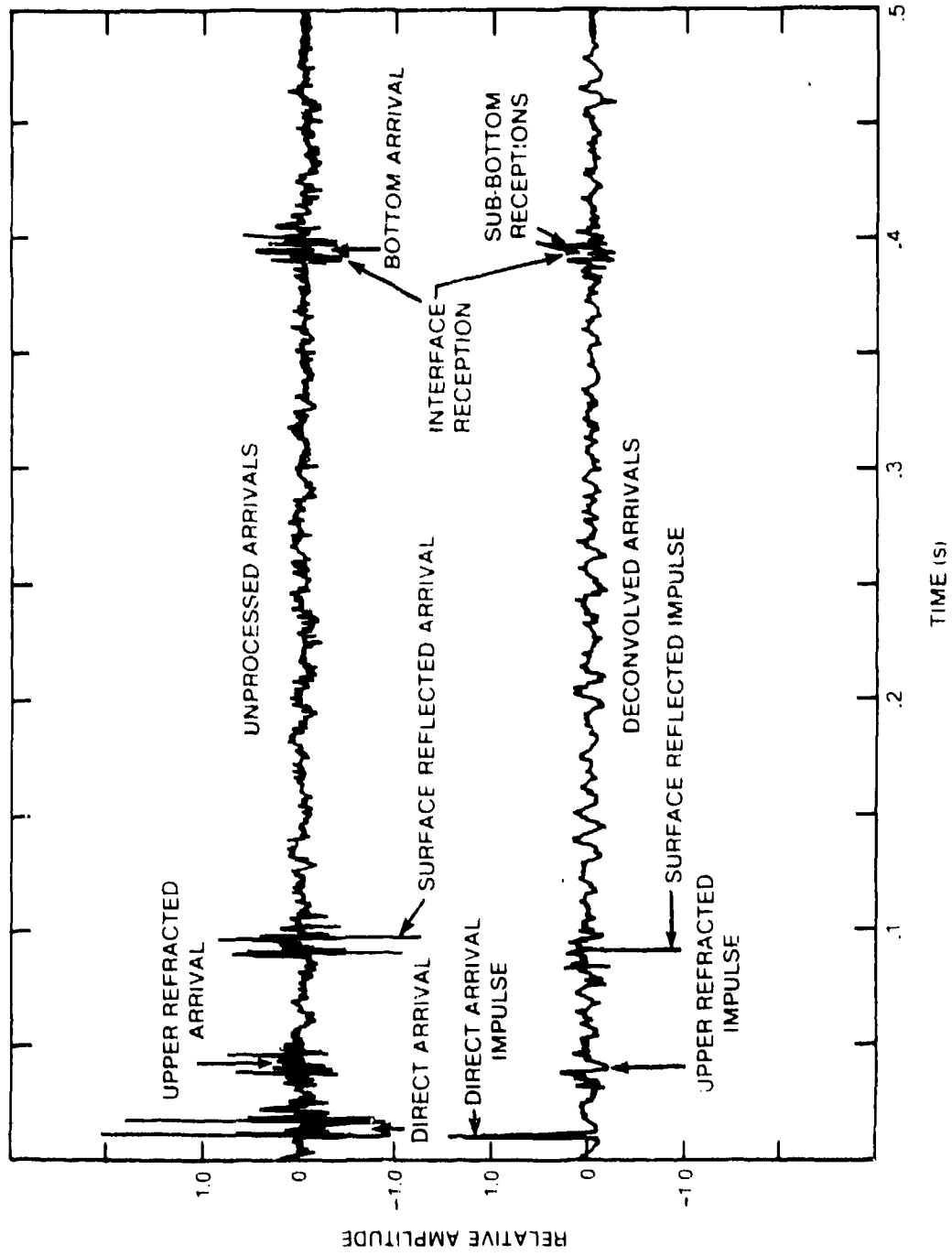


Figure 6. Example of Signal Enhancement Obtained Using Deconvolution

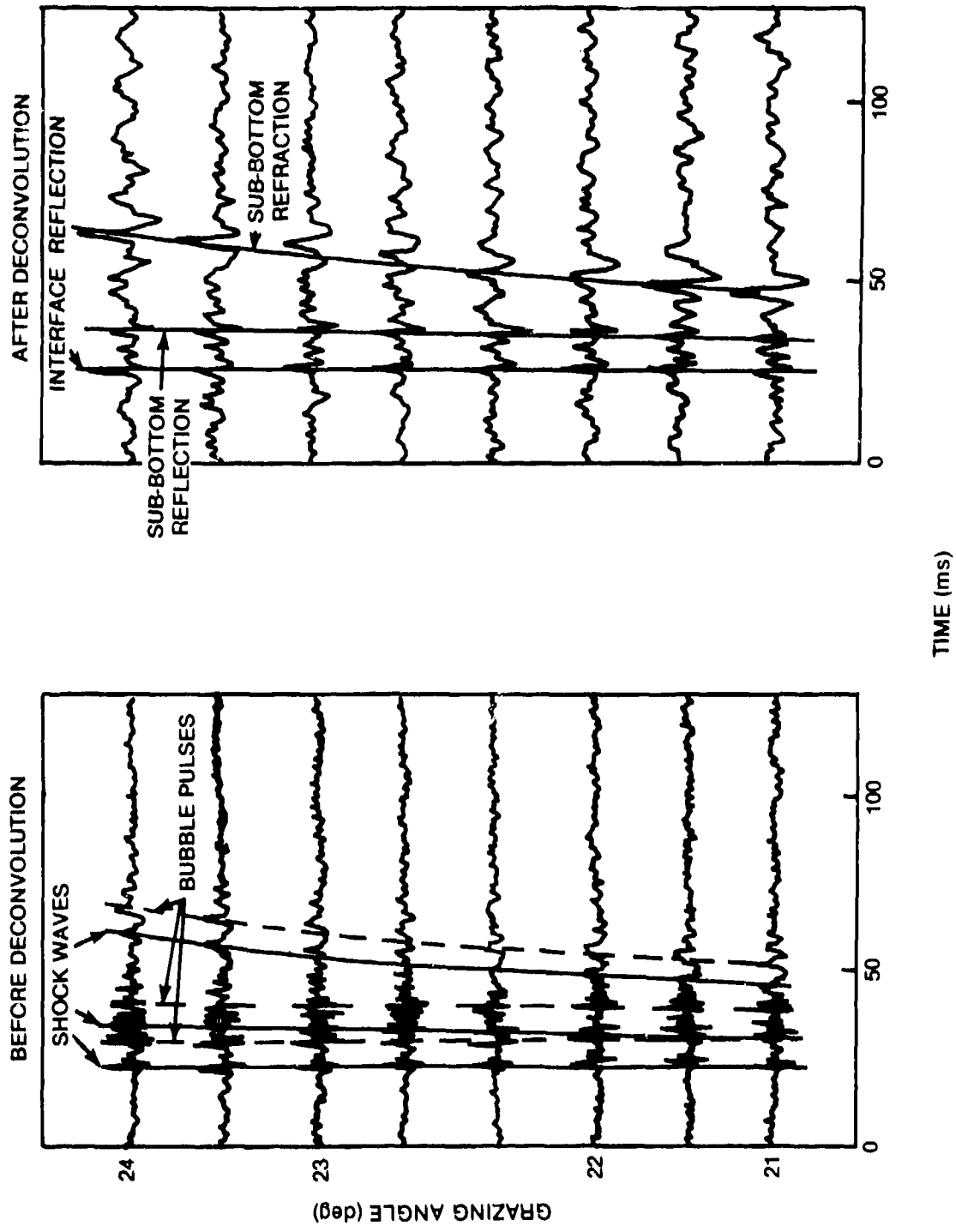


Figure 7. Consecutive Time Displays of Bottom Arrivals as a Function of Grazing Angle With Respect to Interface Reflected Angle (Station BL-1)

LAYER THICKNESS ESTIMATION - SITE BL-1

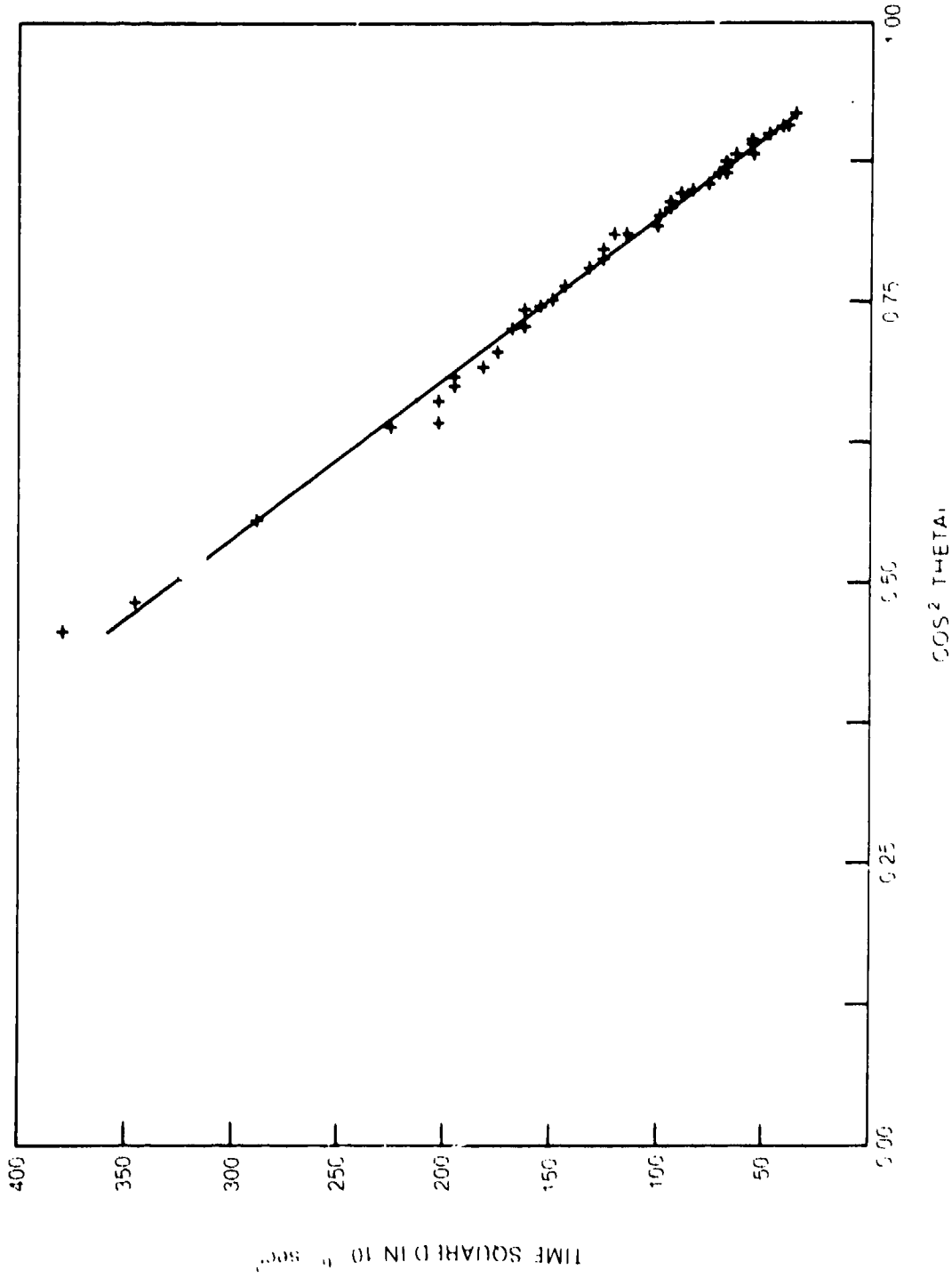


Figure 3. Squared Travel Time Difference Between Subbottom and Ocean Bottom Reflections As a Function of the Cosine Squared of the Ocean Bottom Grazing Angle

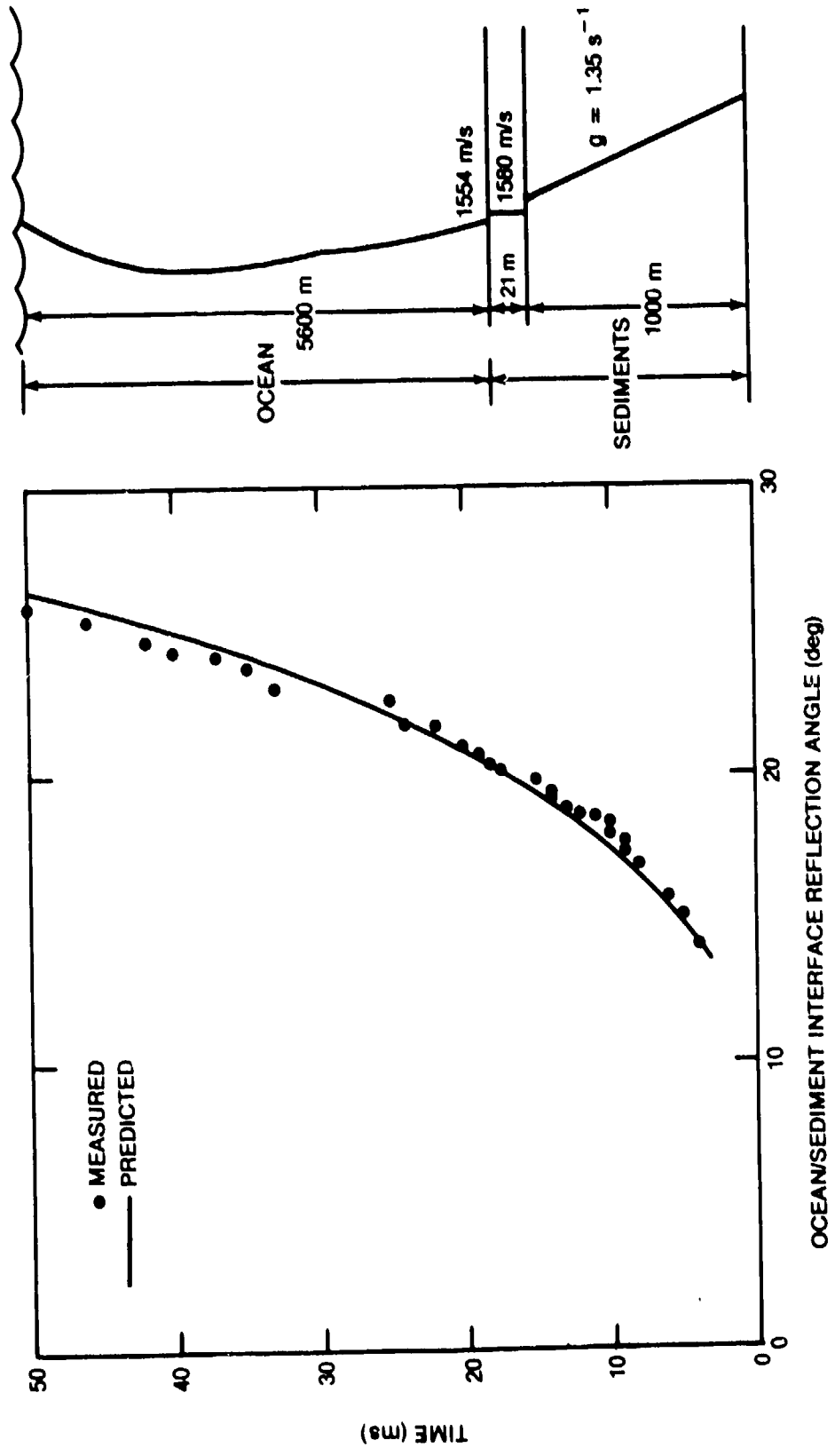


Figure 9. Measured and Predicted Travel Time Differences Between Ocean Bottom Reflected And Subbottom Refracted Arrivals

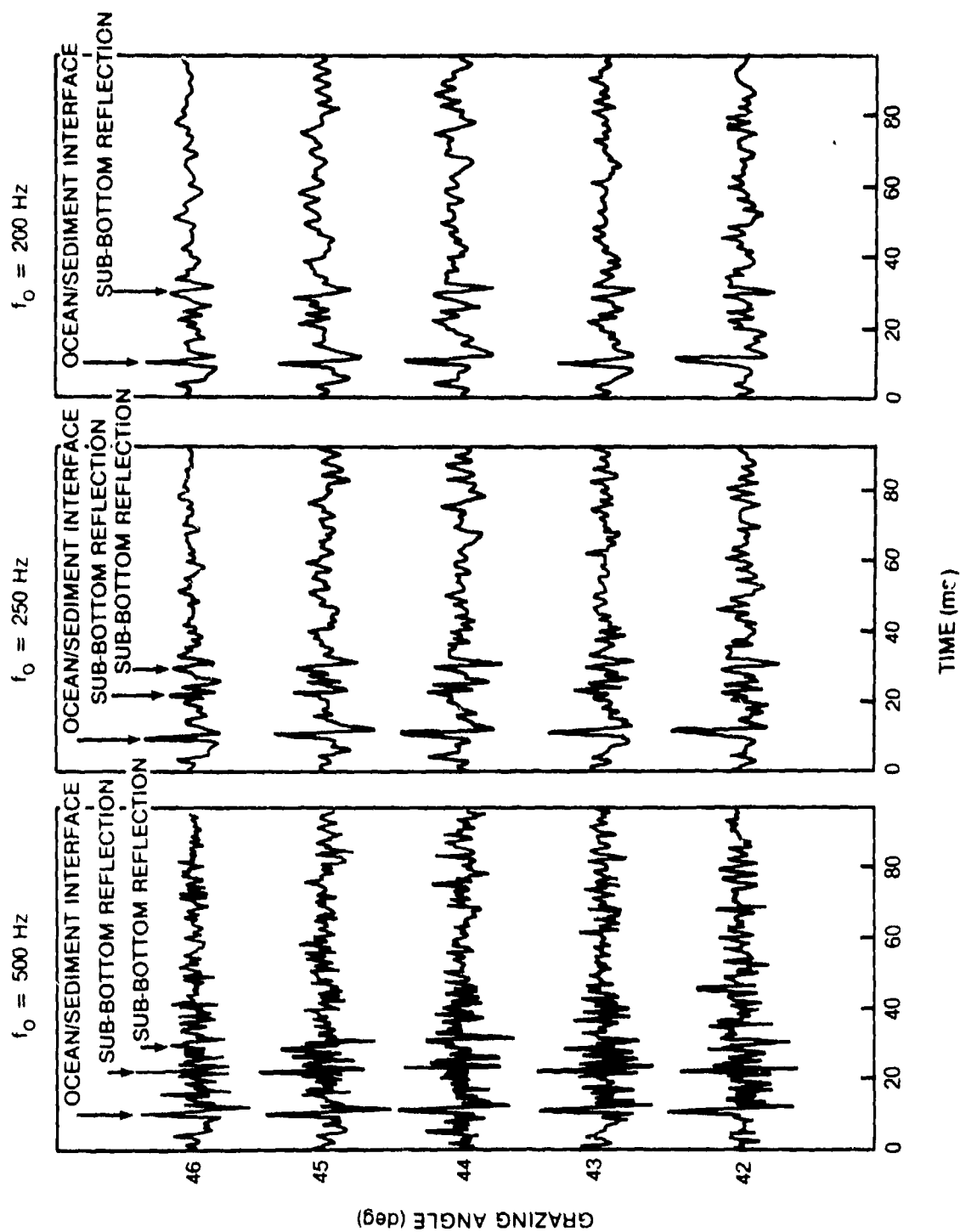


Figure 10. Deconvolved Sediment Interacted Signals Low Pass Filtered at Three Frequencies: 500, 250, and 200 Hz (Site BL-1, Upper Buoy)

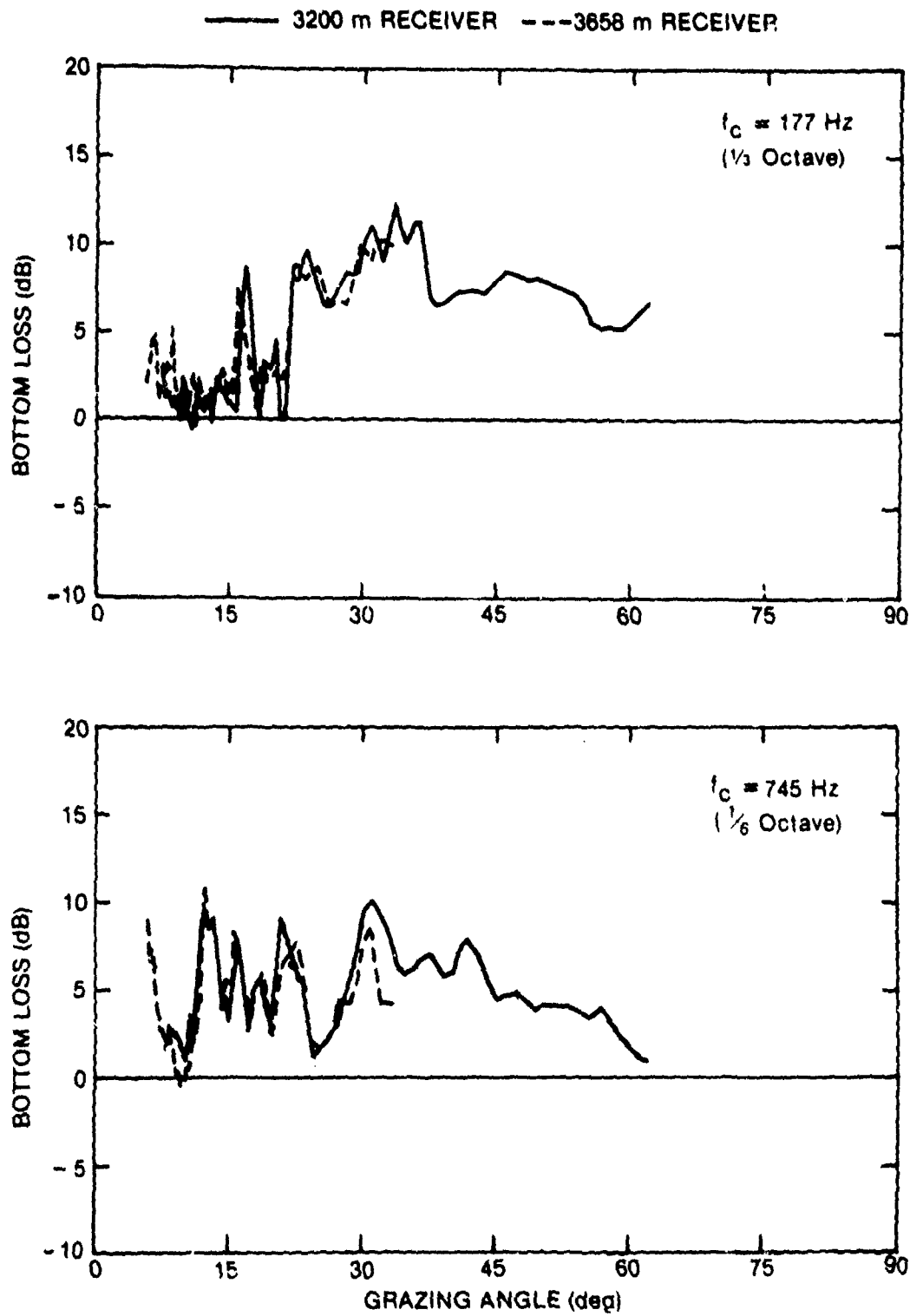


Figure 11. Comparison of Bottom Loss Versus Grazing Angle as a Function of Receiver Depth (Station BL-1)

MAINLOBE STATION BL-2 (28 30N 70 30W) 3353 METER RECEIVER

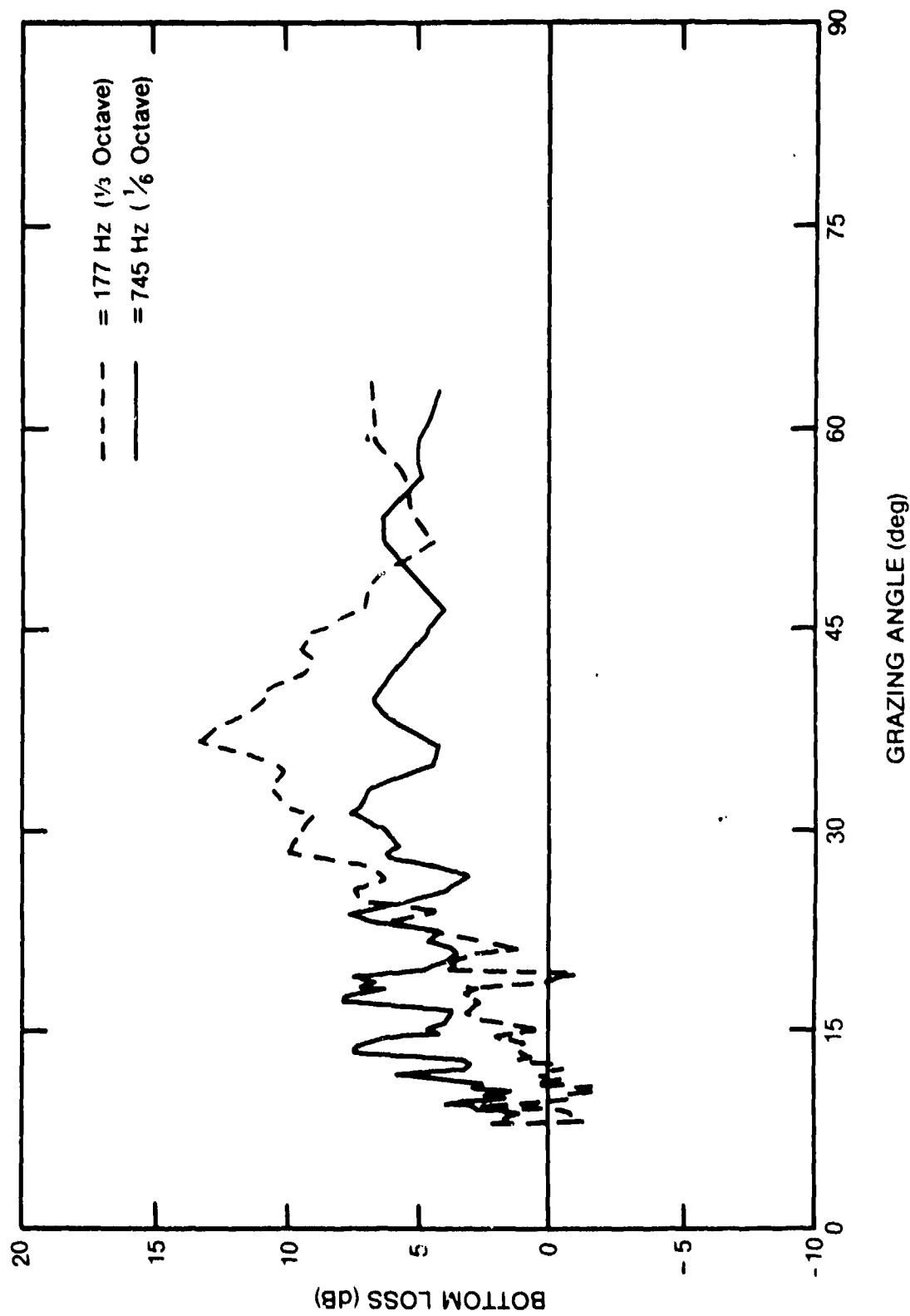


Figure 12. Frequency Variation of Bottom Loss Versus Grazing Angle

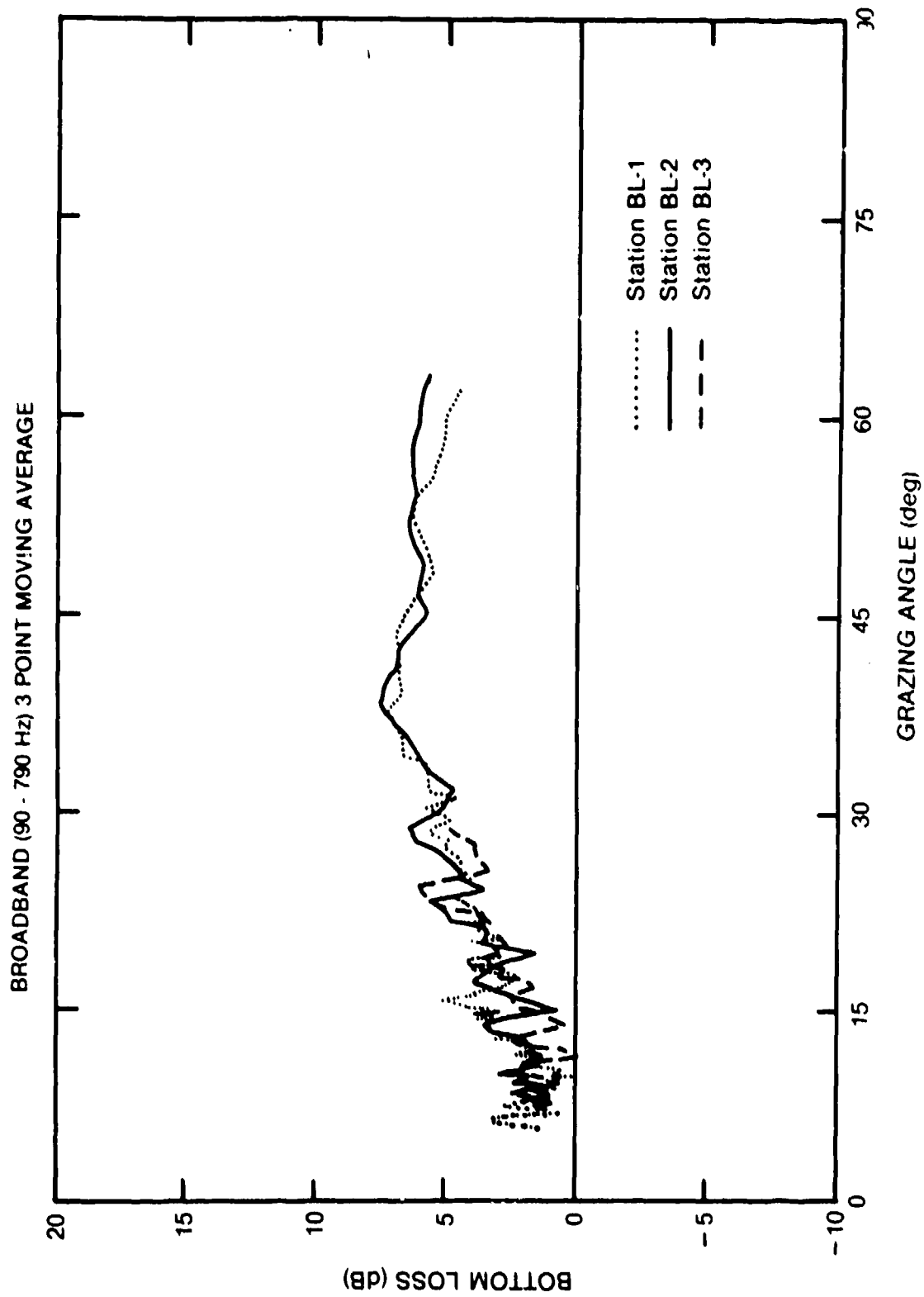


Figure 13. Geographical Variations of Bottom Loss Versus Grazing Angle Data (Broadband)

COMBINED STATIONS BROADBAND (90-790 Hz) BOTTOM LOSS

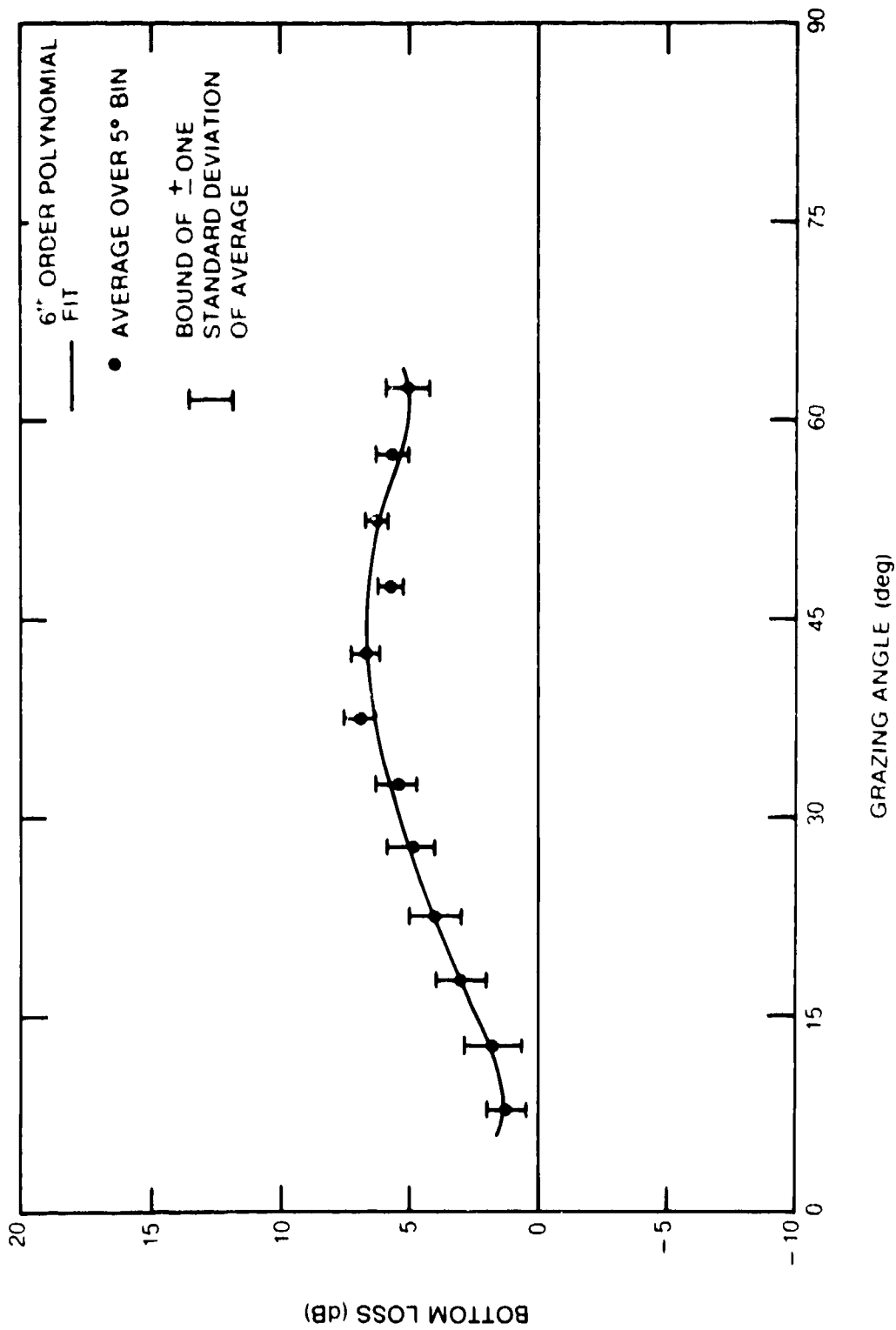


Figure 14. Polynomial Fitted and Averaged Broadband Bottom Loss Measured at Three Stations in the Hatteras Abyssal Plain

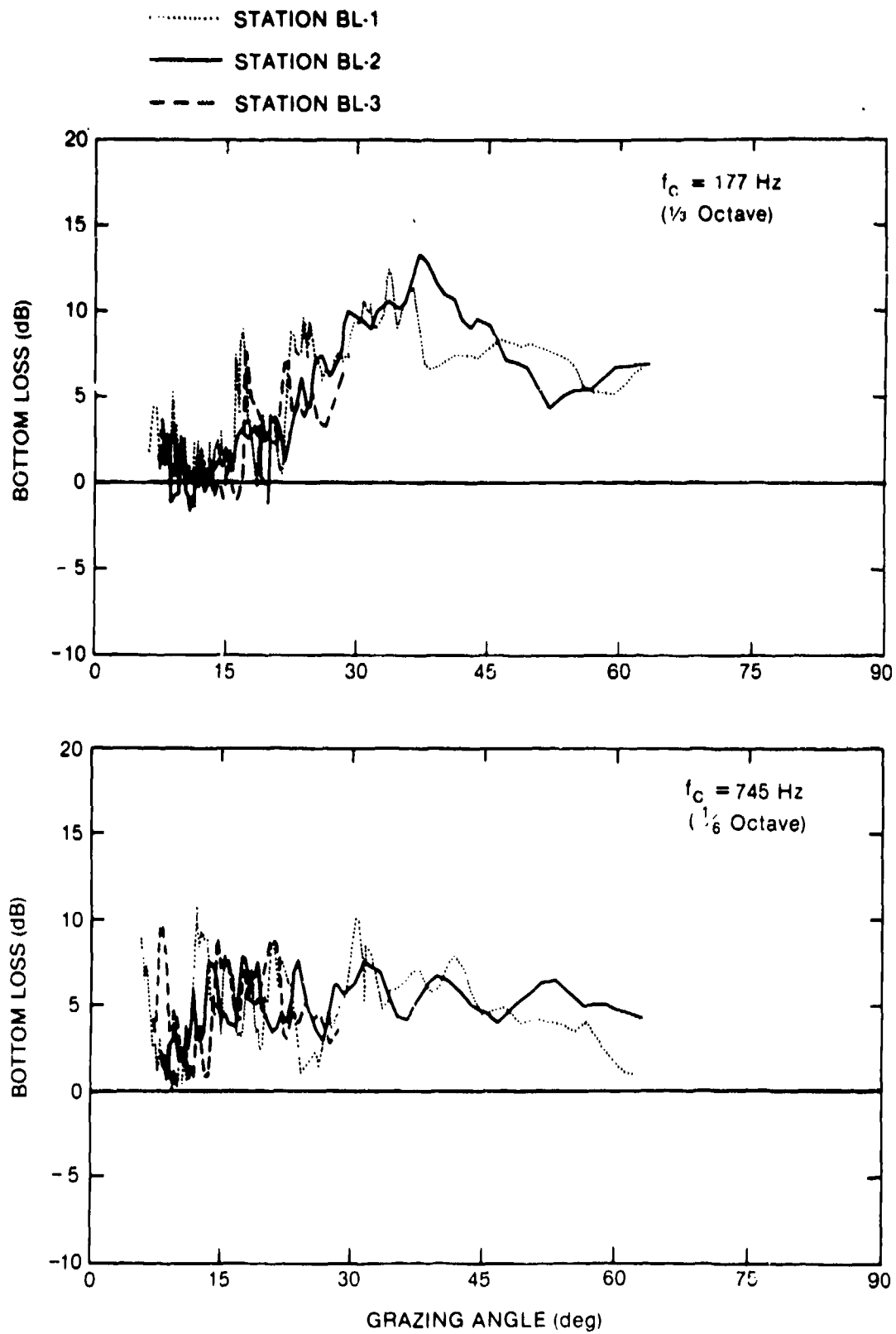


Figure 15. Geographical Variations in Bottom Loss (Narrowband)

## REFERENCES

1. R. S. Gozzo and R. L. Martin, AUTOBUOY, Present Capabilities and Planned Modifications, NUSC Technical Report 4505, June 1973 (UNCLASSIFIED).
2. X. LePichon, J. Ewing, and R. E. Houtz, "Deep Sea Sediment Velocity Determinations Made While Reflection Profiling," Journal of Geophysical Research, vol. 73, no. 8, 1968, pp. 2597-2614.
3. H. Weinberg, Navy Interim Surface Ship Model (NISSM) II, NUSC Technical Report 4527, November 1973 (UNCLASSIFIED).
4. R. E. Houtz, "Preliminary Study of Global Sediment Sound Velocities from Sonobuoy Data," from Physics of Sound in Marine Sediments, ed. Lloyd Hampton, Plenum Pub. Co., N.Y., N.Y.
5. R. E. Houtz and G. M. Bryan, "Determination of Near-Surface Velocity Functions From Artemis Sonobuoy Data," (unpublished manuscript).
6. C. C. Tyndale, "Instruction Manual Model 1890 Boomerang Sediment Corer IM1890," Benthos, Inc., MA, November 19, 1968.
7. S. R. Santaniello and R. K. Dullea, "MAINLOBE '73 Research Cruise Trip," NUSC Technical Memorandum TALL-203-73, 18 July 1973.
8. S. R. Santaniello, F. R. DiNapoli, R. K. Dullea, and P. D. Herstein, A Synopsis of Studies on the Interaction of Low Frequency Acoustic Signals with the Ocean Bottom, NUSC Technical Document 5337, July 1976 (UNCLASSIFIED).
9. S. R. Santaniello and P. D. Herstein, Labrador Basin Low Frequency Bottom Loss Measurements, NUSC Technical Report 4711, 12 March 1975 (UNCLASSIFIED).
10. S. R. van der Veen and S. R. Santaniello, Digital Processing of Explosive-Source Ocean-Bottom-Reflected Acoustic Signals, NUSC Technical Report 4337, 9 August 1972 (UNCLASSIFIED).
11. S. R. van der Veen, "A Program to Simulate Butterworth Filters on a Digital Computer," NUSC Technical Memorandum 2211-309-70, 1 October 1970.
12. J. M. Hoven, "Deconvolution for Removing the Effects of Bubble Pulses of Explosive Charges," JASA, Vol. 47, No. 1, 1970, pp. 281-284.
13. R. L. Dicus, "Synthetic Deconvolution of Explosive Source Acoustic Signals in Colored Noise," Naval Oceanographic Office, Technical Note 6130-3-76.

14. J. S. Cohen and L. T. Einstein, Continuous Gradient Ray Tracing System (CONGRATS) II: Eigenray Processing Programs, NUSC Technical Report 1069.
15. S. R. Santaniello, "Factors to Consider when Measuring Low Frequency Bottom Loss," NUSC TM TALL-50-76, 9 February 1976.
16. J. S. Hanna, "Some Complications in the Traditional Measurements of Bottom Loss," Science Applications, Inc., Report SAI-76-664-WA, November 1976.
17. D. C. Stickler, "Negative Bottom Loss Critical Angle Shift, and the Interpretation of the Bottom Reflection Coefficient, JASA, Vol. 61, No. 3 March 1977, pp. 707-710.
18. D. R. Horn, M. Ewing, B. M. Horn, and M. N. Delach, A Prediction of Sonic Properties of Deep-Sea Cores, Hatteras Abyssal Plain and Environs, Technical Report No. 1, CU-1-69 NAVSHIPS N00024-69-C-1184, November 1969.
19. M. Ewing, G. Carpenter, C. Windisch, and J. Ewing, "Sediment Distribution in the Oceans: The Atlantic," Geological Society of America Bulletin, Vol. 84, January 1973, pp. 71-88.
20. R. G. Houtz, personal communication, 5 September 1973.

## Appendix A

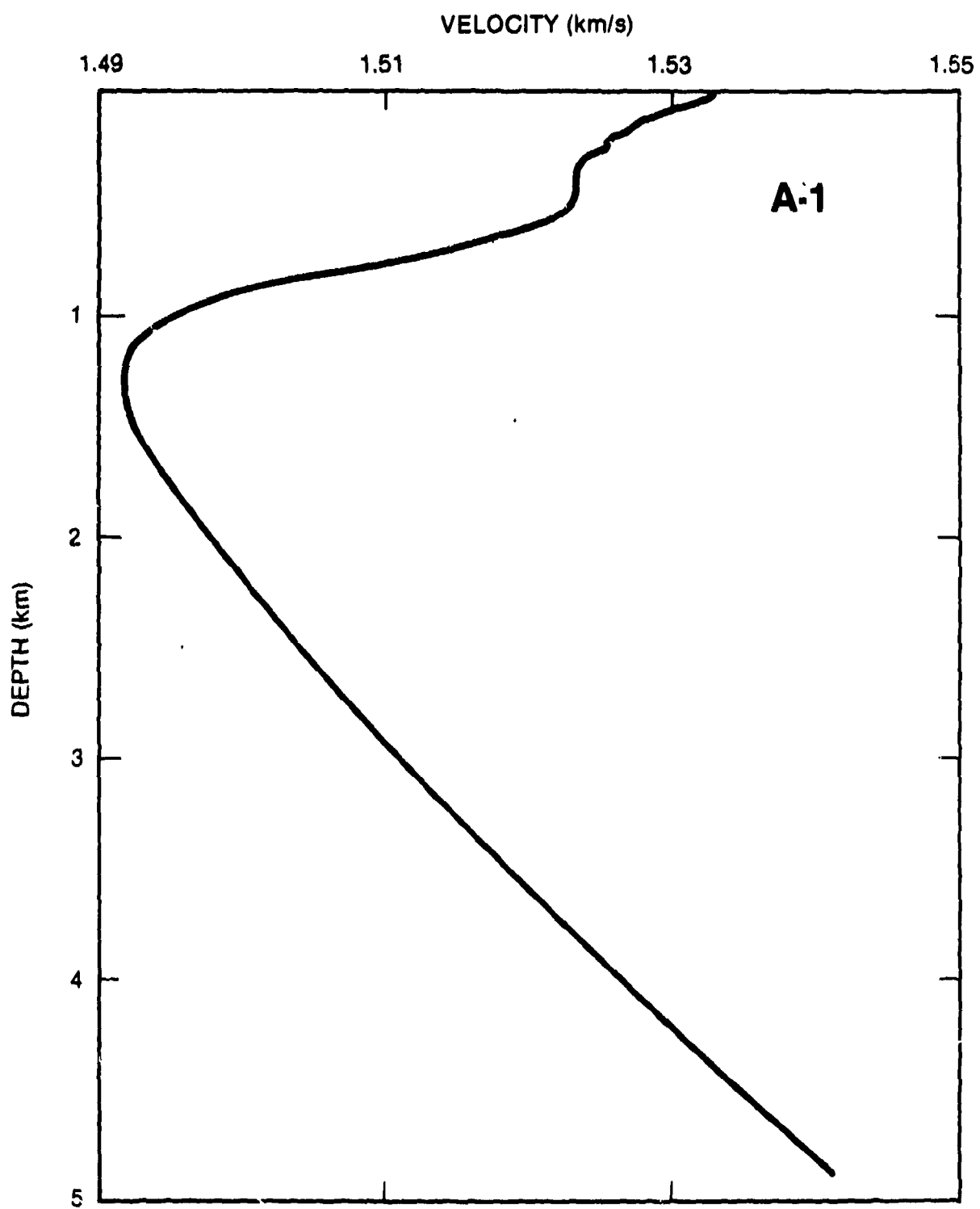
## SOUND SPEED VERSUS DEPTH PROFILES

Results of the deep velocimeter casts are presented in figures A-1 through A-5. Separate profiles were obtained as the velocimeter was lowered (down cast) and raised (up cast). Note that the velocimeter casts never reached bottom depths. The sound speed profile (SSP) was linearly extrapolated to the ocean bottom to obtain the full water column profile. Table A-1 lists the relevant parameter for each profile.

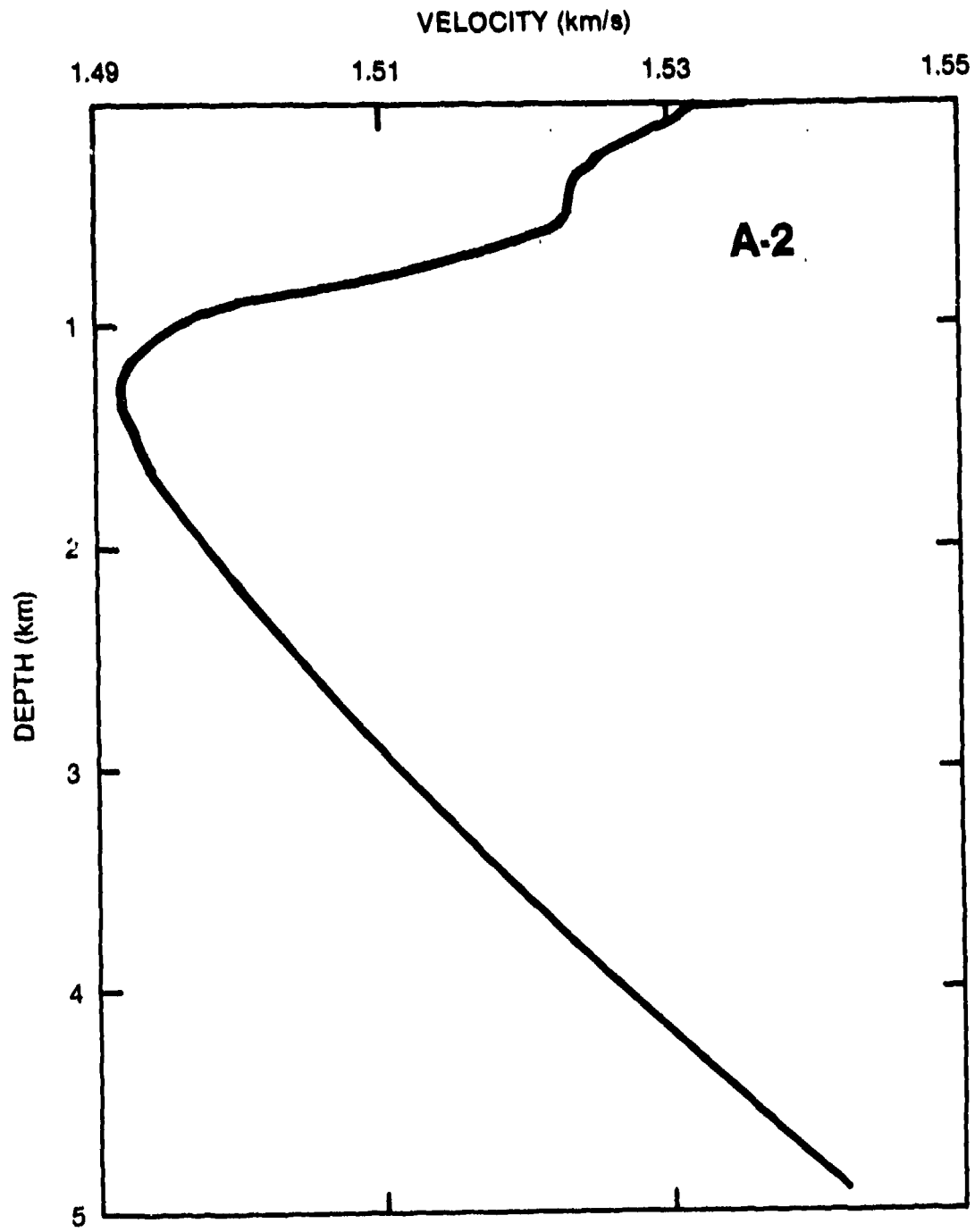
Table A-I. Sound Speed Profile Parameters

Figure No.	Station No.	Cast	Actual Depth (m)
A-1	BL-1	Down	5600
A-2	BL-1	Up	5600
A-3	BL-2	Down	5600
A-4	BL-3	Down	5439
A-5	BL-3	Up	5439

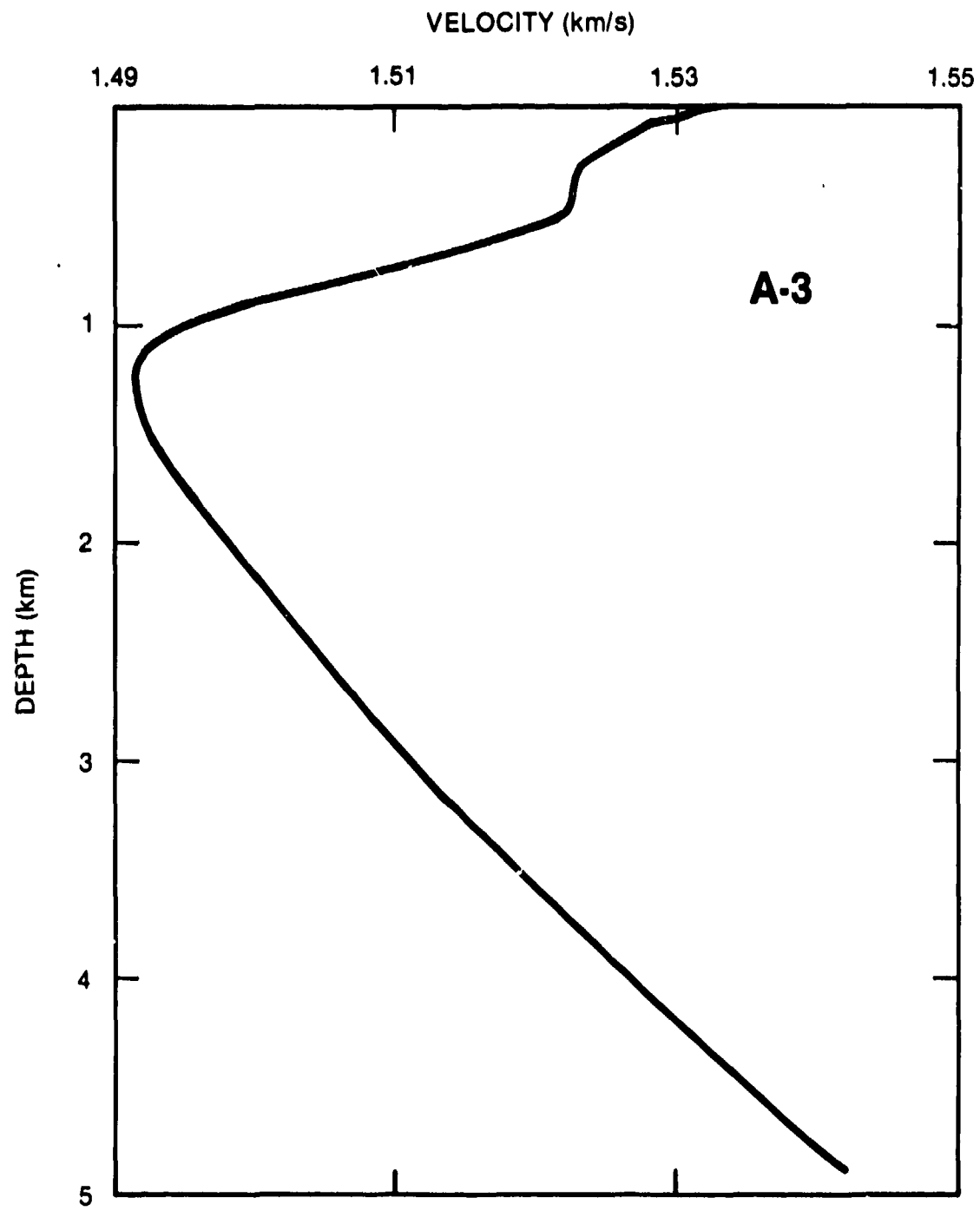
TR 5781

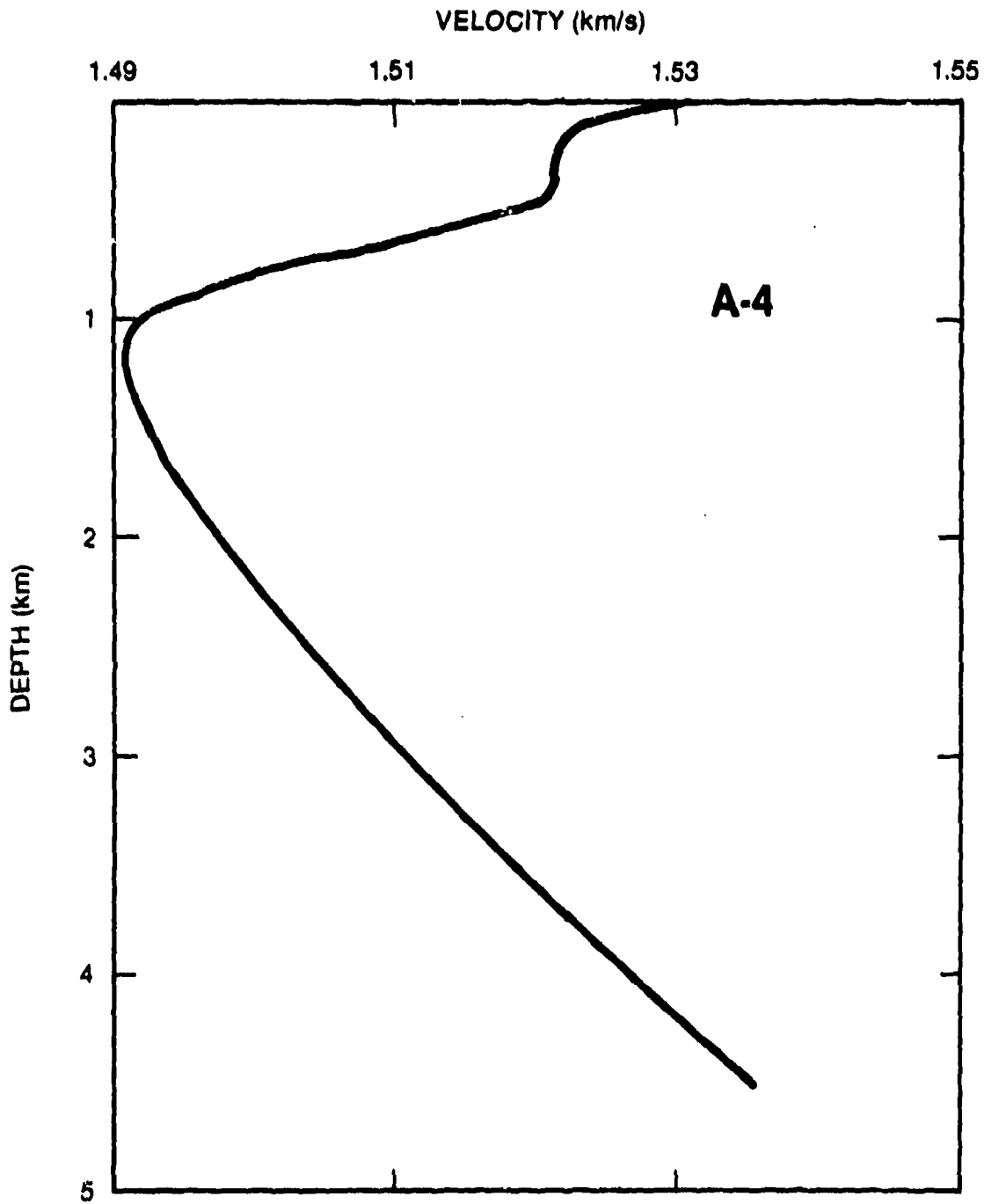


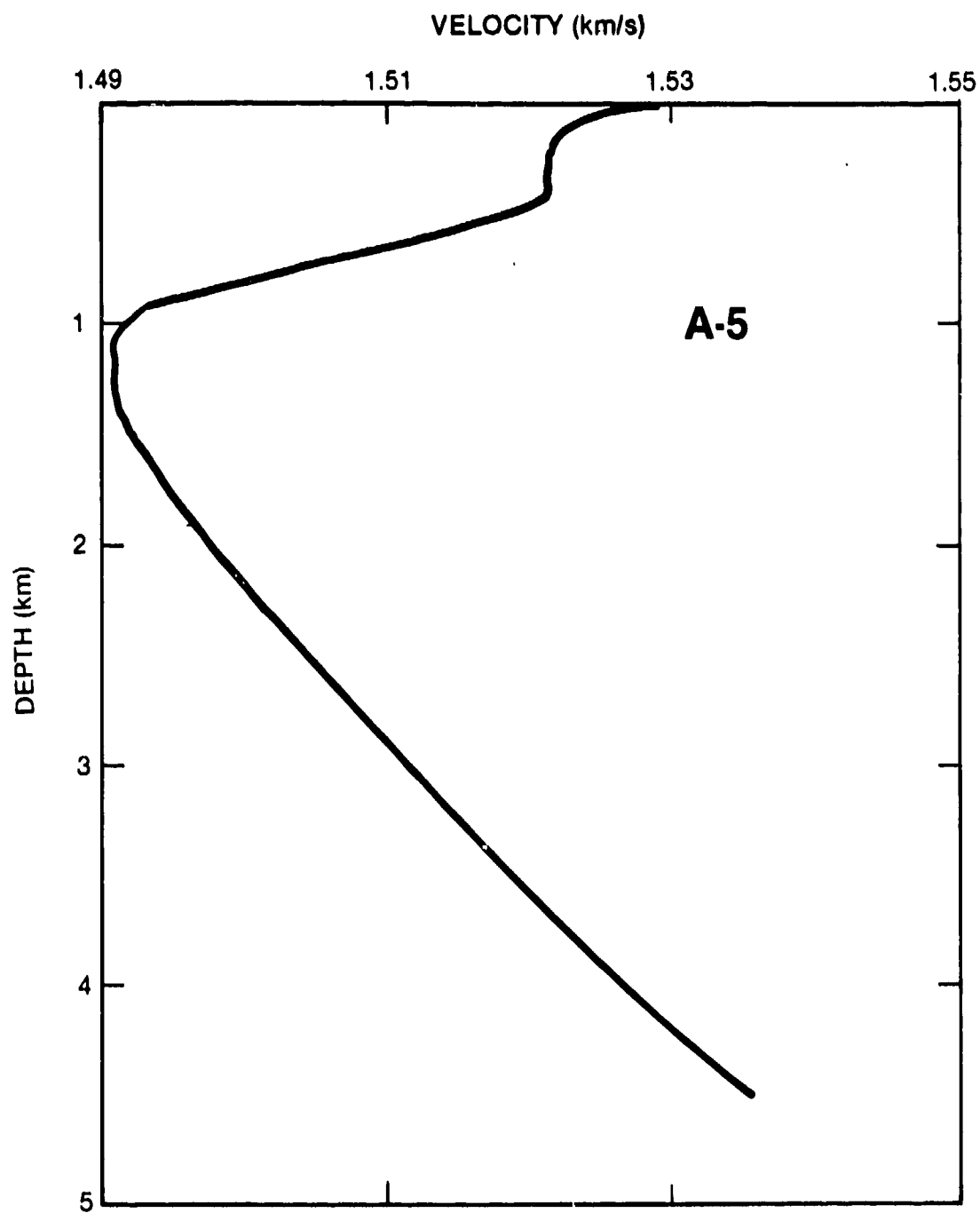
A-2



A-2







## Appendix B

PLOTS OF BOTTOM LOSS VERSUS GRAZING ANGLE  
(ALL STATIONS AND FREQUENCIES)

Table B-1 provides the key to the conditions during the bottom loss versus grazing angle depicted by the figures in this appendix.

Table B-1. Bottom Loss Versus Grazing Angle Data For All Stations and Frequencies

Figure Nos.	Station No.	Geometry Source Depth (m)	Receiver Depth (m)	Notes
B-1 through B-8	BL-1	914	3200	-
B-9 through B-16	BL-1	914	3658	-
B-17 through B-24	BL-1	914	3658	Expanded Scales
B-25 through B-32	BL-1	914	3658 + 3200	Combined Receivers
B-33 through B-40	BL-2	914	3353	-
B-41 through B-48	BL-3	914	3353	-
B-49 through B-56	BL-3	914	3353	Expanded Scales
B-57 through B-64	BL-1, 2, +3	914	3200, 3353, +3658	Combined Stations

BOTTOM LOSS VS GRAZING ANGLE  
MAINLOBE STATION BL-1 (28 C8N 70 30W) 3200 METER RECEIVER

B-2

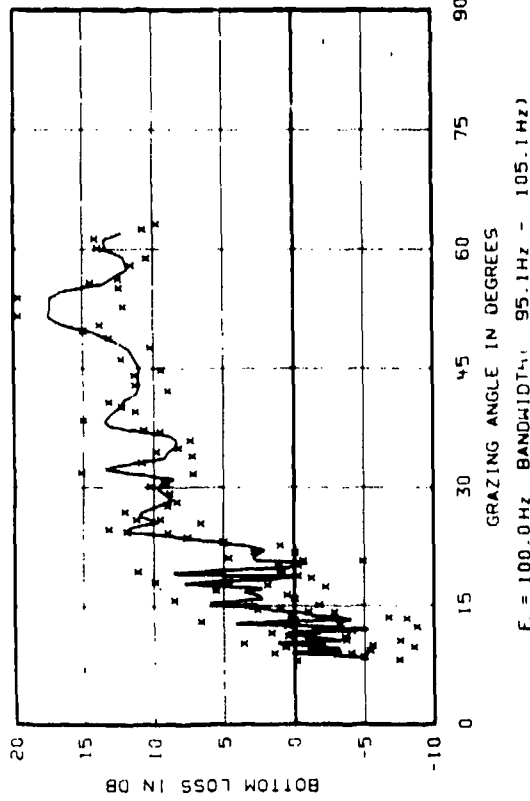


FIG B-1

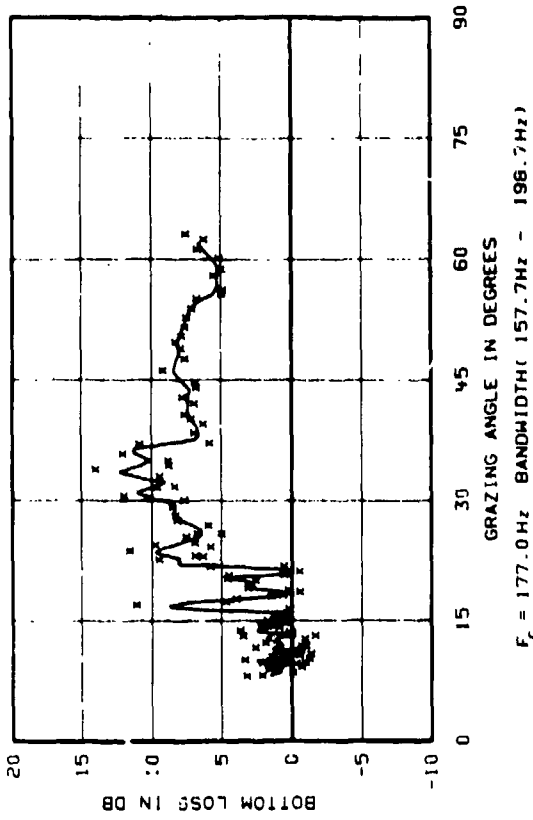


FIG B-2

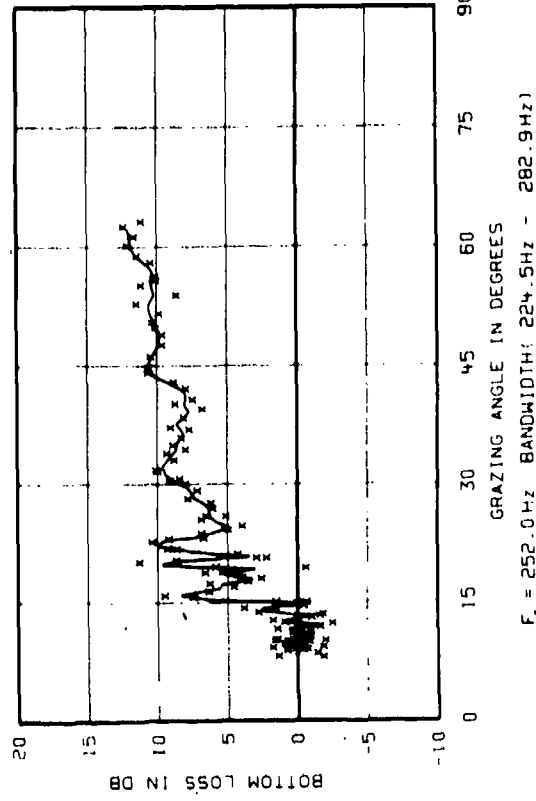


FIG B-3

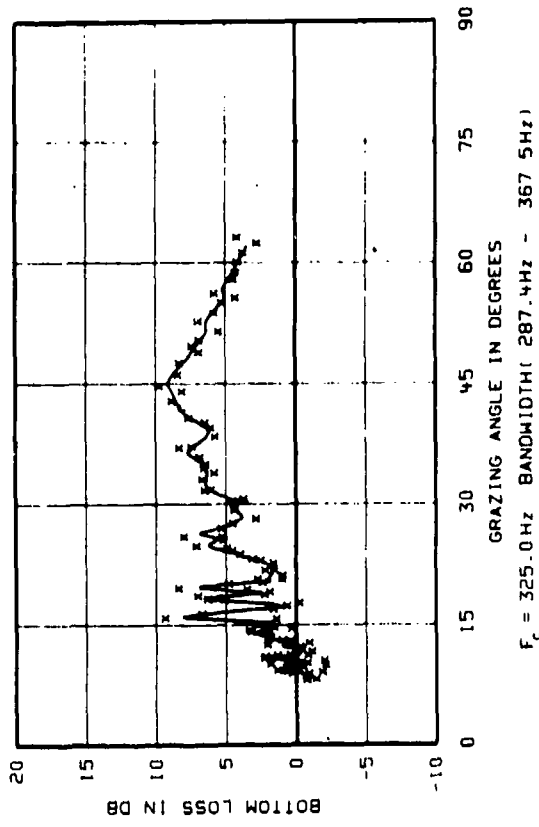


FIG B-4

MAINLOBE STATION BL-1 (28 08N 70 30W) 3200 METER RECEIVER

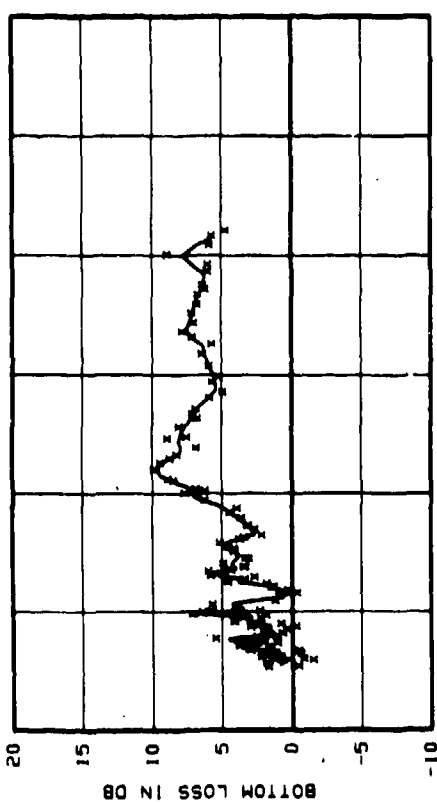


FIG. B-5  
 $F_c = 445.0 \text{ Hz}$  BANDWIDTH( 396.4 Hz - 499.5 Hz)

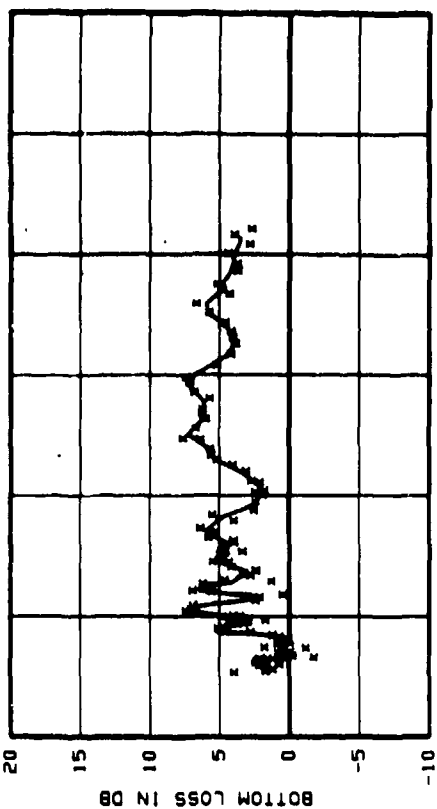


FIG. B-6  
 $F_c = 600.0 \text{ Hz}$  BANDWIDTH( 534.5 Hz - 673.5 Hz)

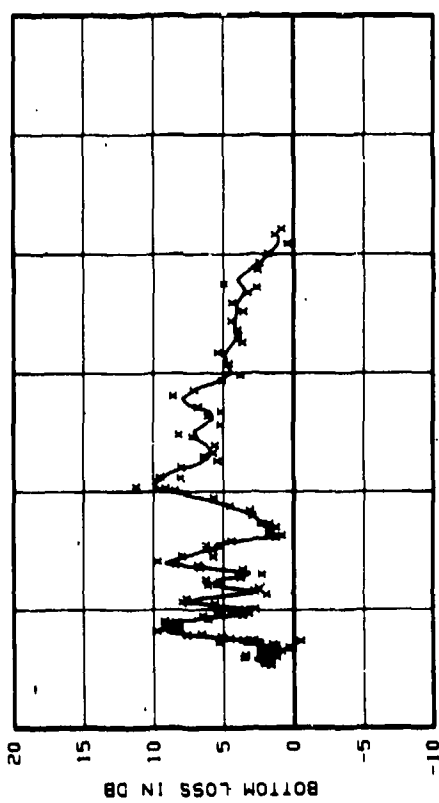


FIG. B-7  
 $F_c = 745.0 \text{ Hz}$  BANDWIDTH( 703.2 Hz - 789.3 Hz)

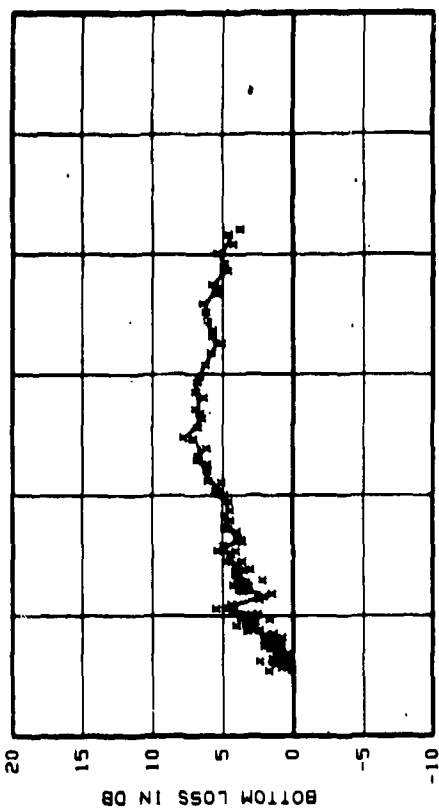


FIG. B-8  
 BROADBAND BANDWIDTH( 10.0 Hz - 750.0 Hz)

BOTTOM LOSS VS GRAZING ANGLE  
MAINLOBE STATION BL-1 (28 DBN 70 W) 3658 METER RECEIVER

B-4

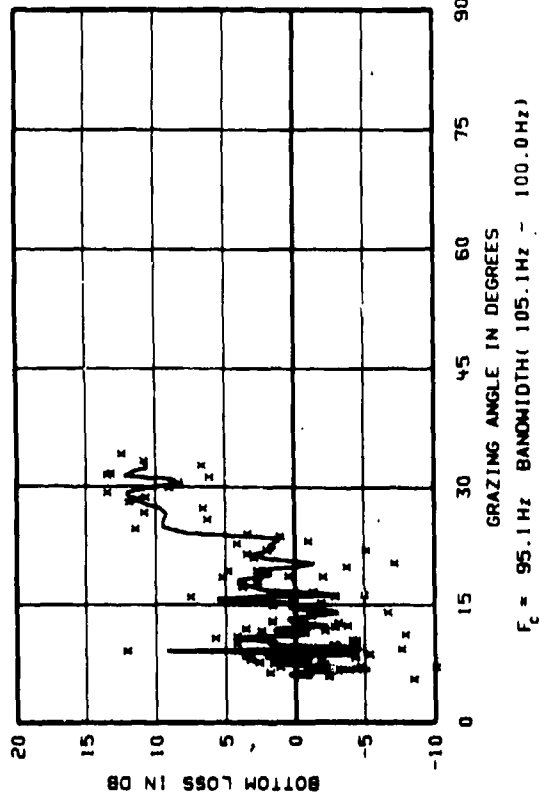


FIG B-9

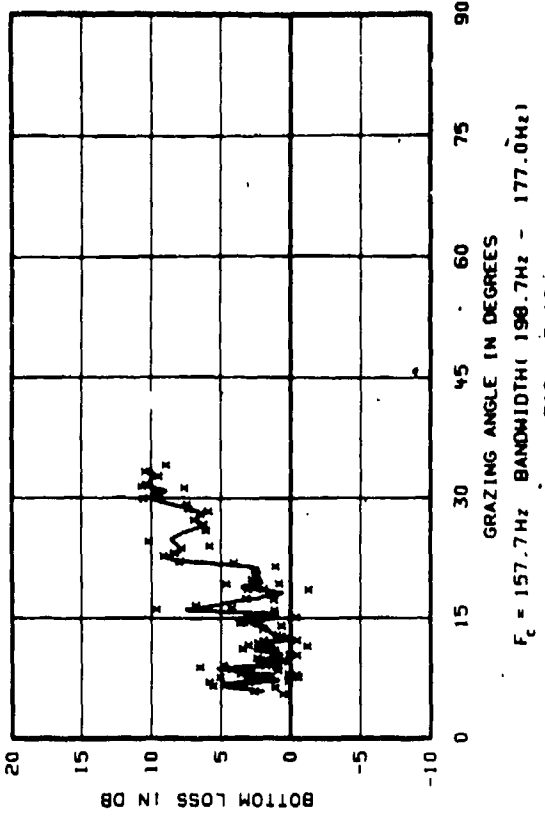


FIG B-10

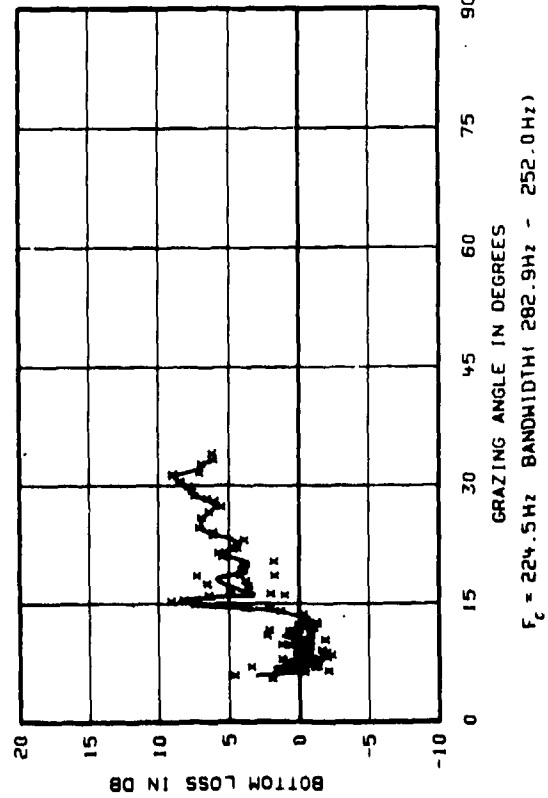


FIG B-11

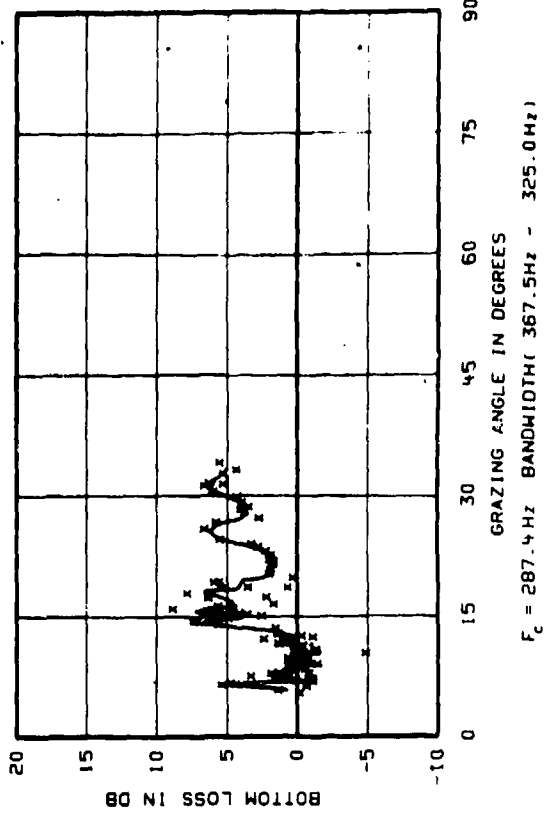


FIG B-12

MAINLOBE STATION BL-1 (28 08N 70 30W) 3658 METER RECEIVER

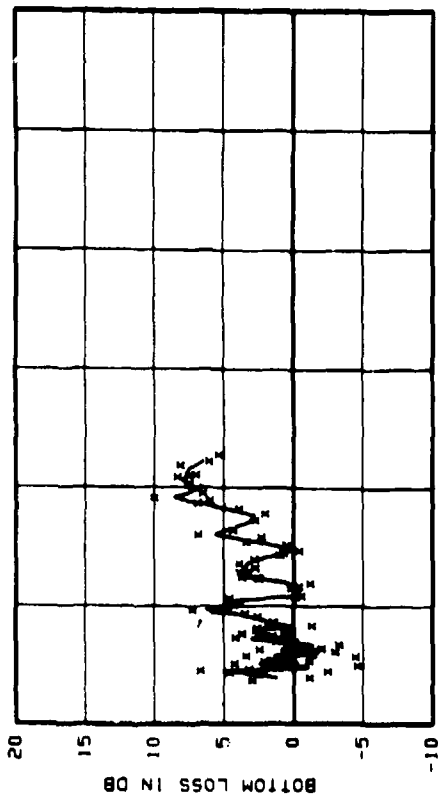


FIG 8-13  
 $F_c = 396.4 \text{ Hz}$  BANDWIDTH( 499.5Hz - 445.0Hz)

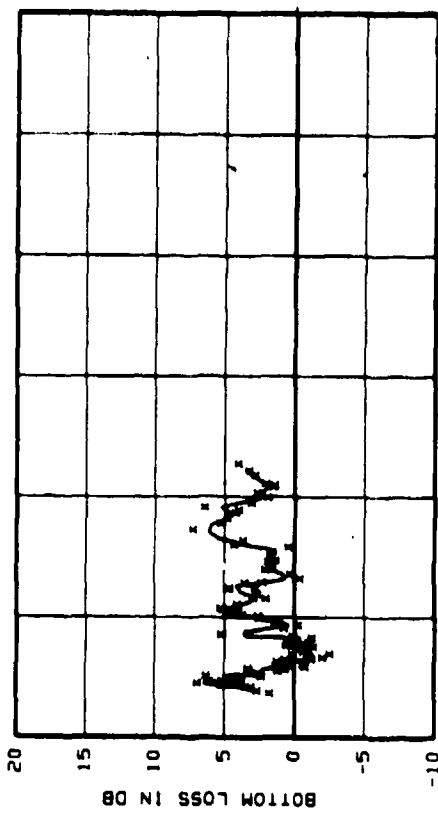


FIG 8-14  
 $F_c = 534.5 \text{ Hz}$  BANDWIDTH( 673.5Hz - 600.0Hz)

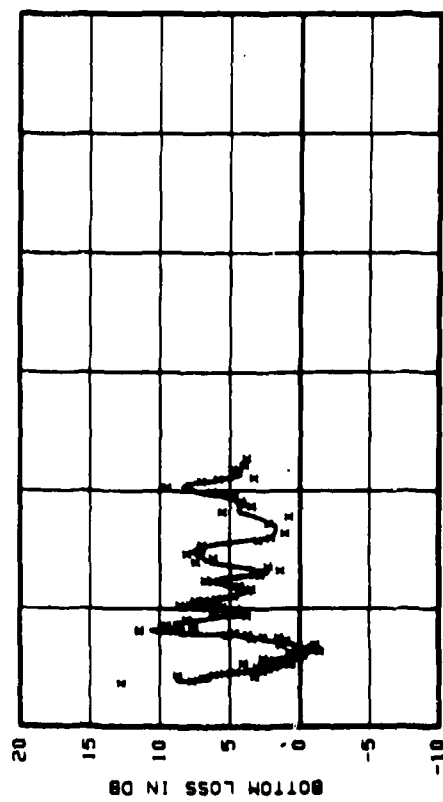


FIG 8-15  
 $F_c = 703.2 \text{ Hz}$  BANDWIDTH( 700.3Hz - 745.0Hz)

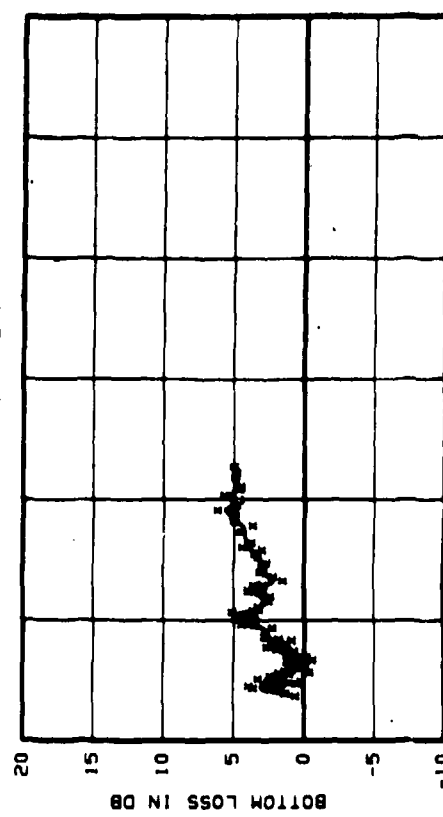


FIG 8-16  
 $F_c = 10.0 \text{ Hz}$  BANDWIDTH( 750.0Hz - 0.0Hz)

MAINLOBE STATION BL-1 (28 08N 70 30W) 3658 METER RECEIVER

B-6

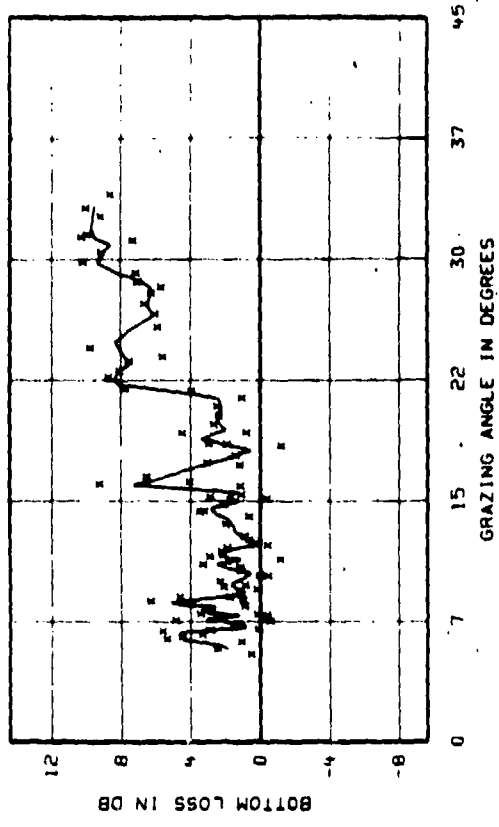


FIG 8-18  
 $F_c = 177.0 \text{ MHz}$  BANDWIDTH: 177.0 Hz

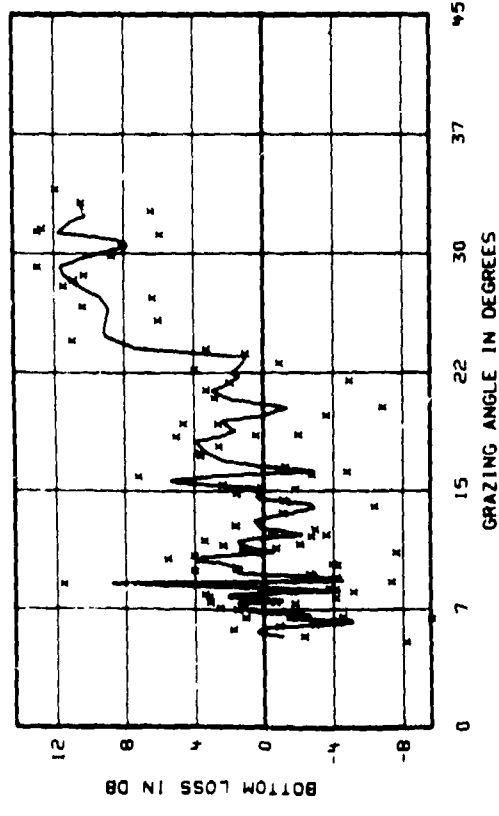


FIG 8-17  
 $F_c = 100.0 \text{ MHz}$  BANDWIDTH: 100.0 Hz

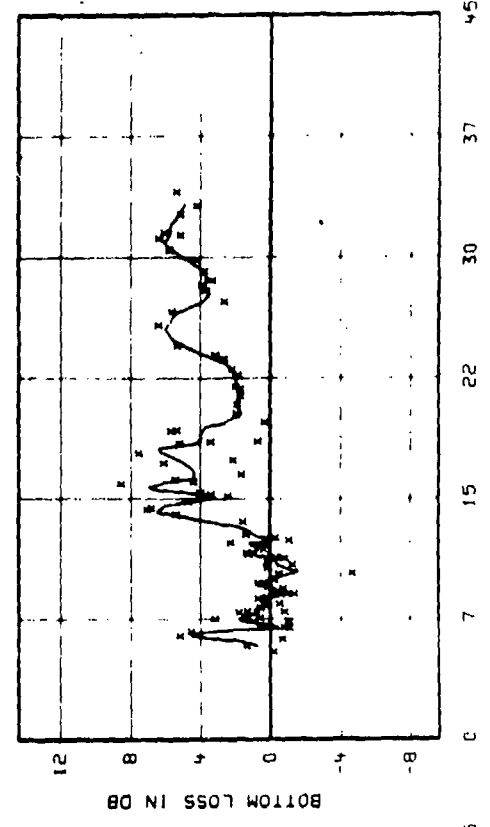


FIG 8-20  
 $F_c = 325.0 \text{ MHz}$  BANDWIDTH: 325.0 Hz

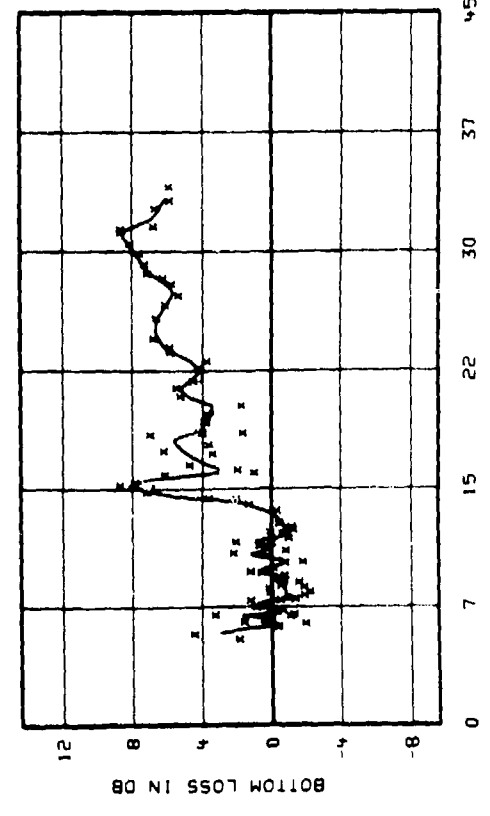
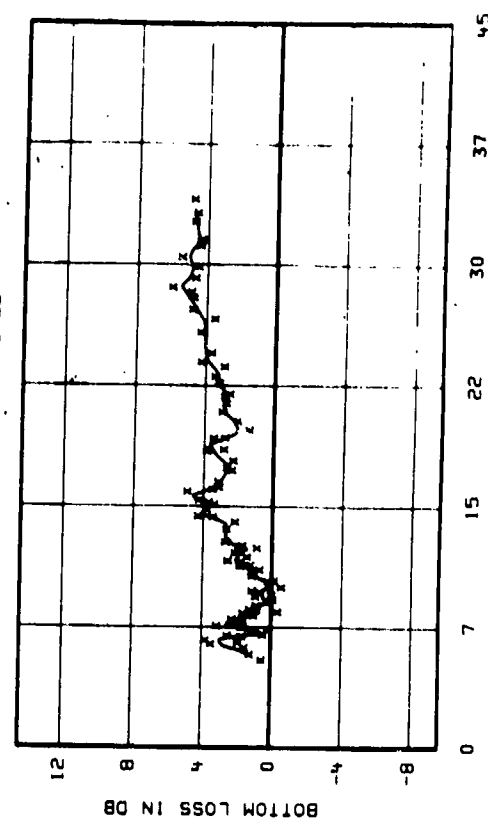
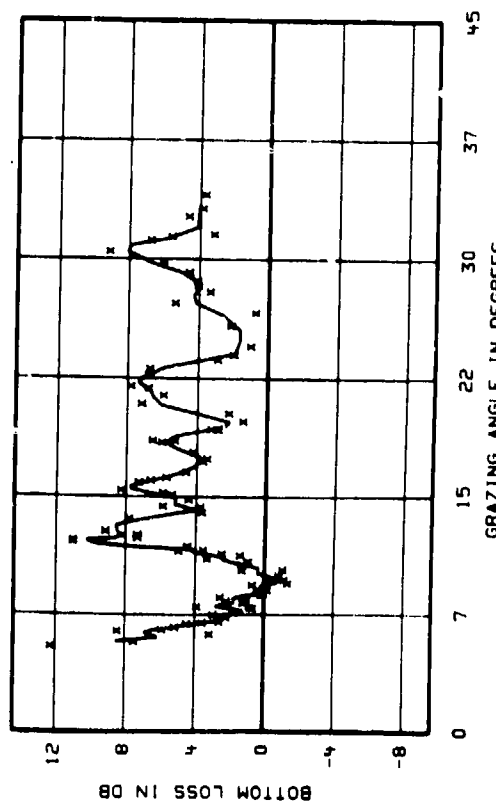
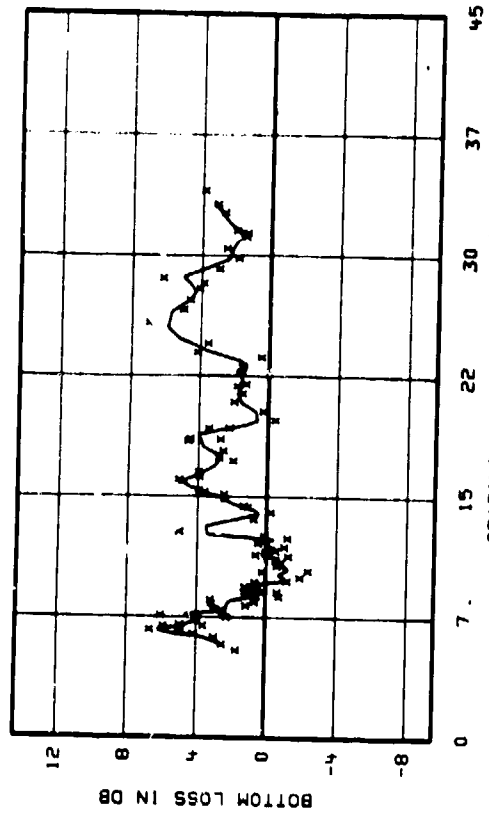
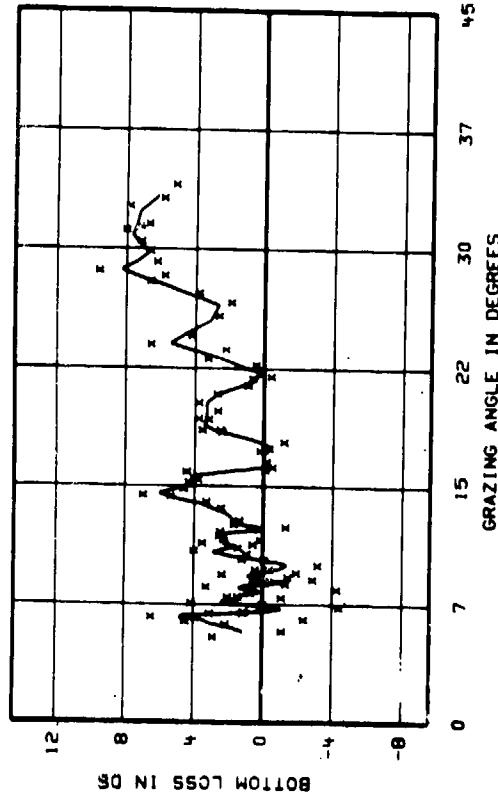


FIG 8-19  
 $F_c = 252.0 \text{ MHz}$  BANDWIDTH: 252.0 Hz

MAINLOBE STATION BL-1 (28 08N 70 30W) 3658 METER RECEIVER



MAINLOBE STATION BL-1 (28 DBN 70 30W) COMBINED RECEIVERS

BOTTOM LOSS VS GRAZING ANGLE

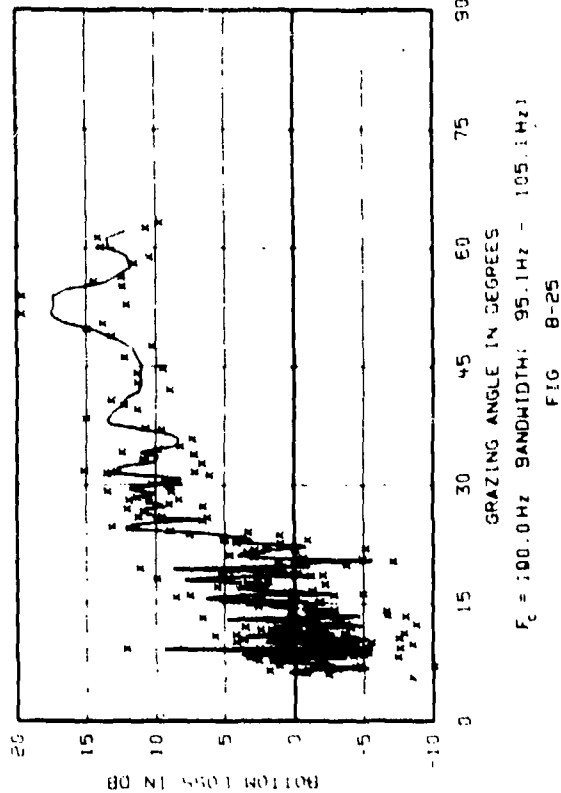


FIG 8-25

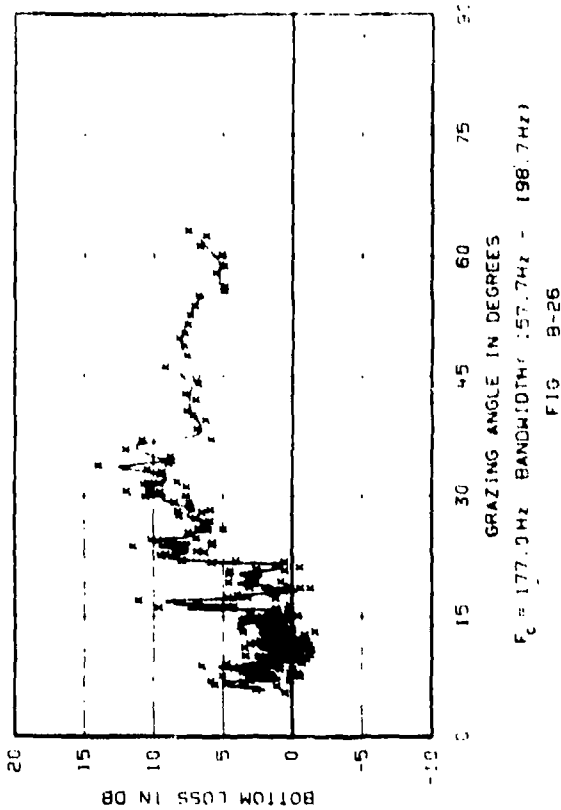


FIG 8-26

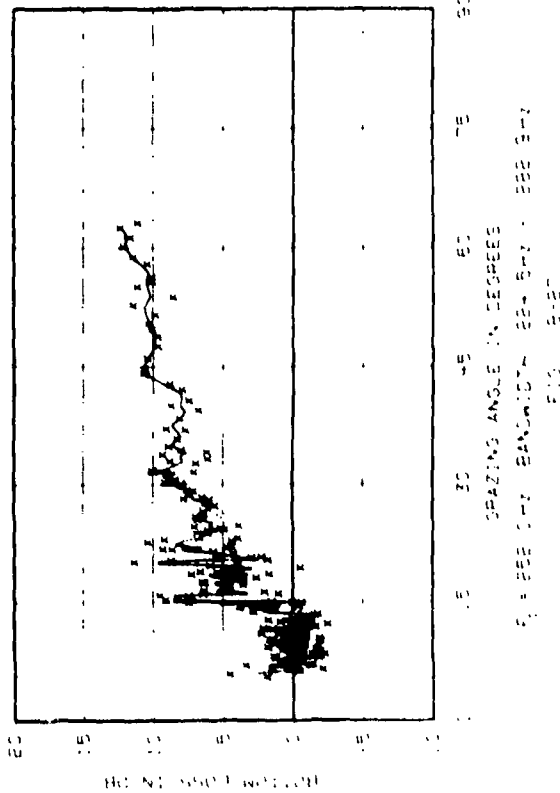


FIG 8-27

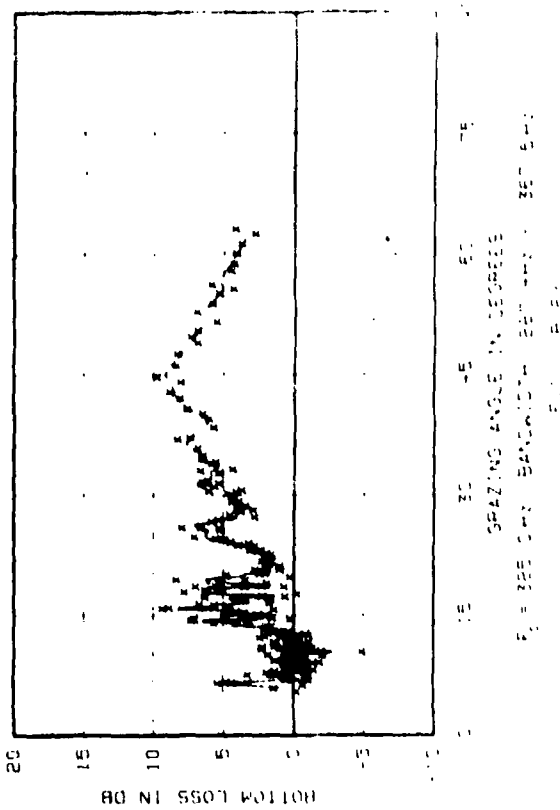
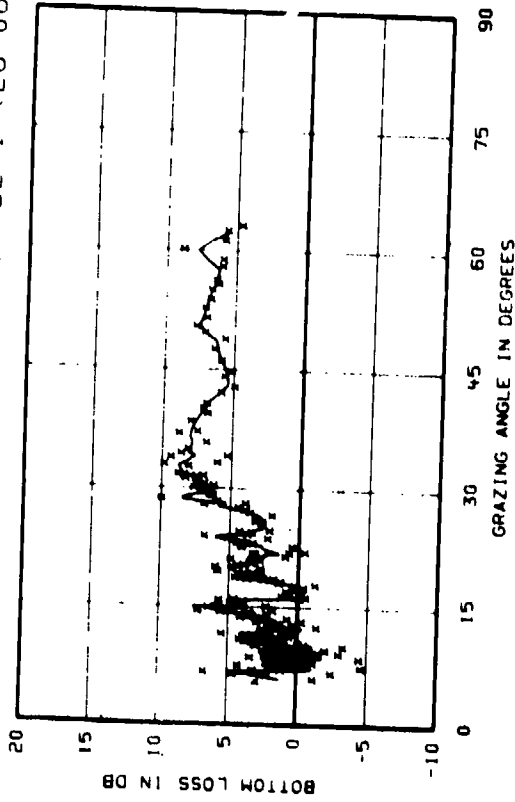
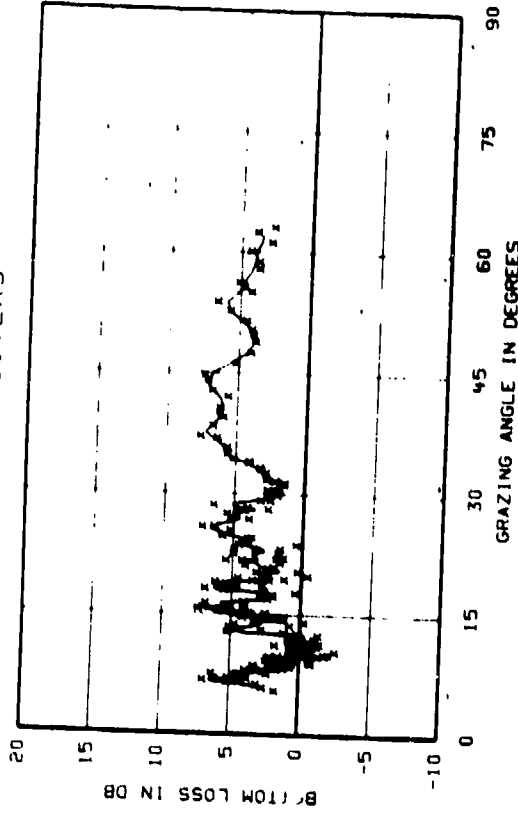


FIG 8-28

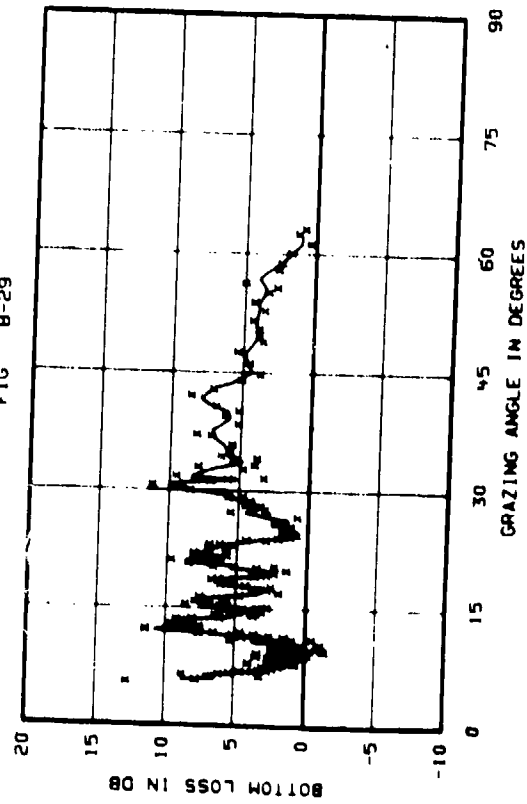
BOTTOM LOSS VS GRAZING ANGLE  
 MAINLOBE STATION BL-1 (28 08N 70 30W) COMBINED RECEIVERS



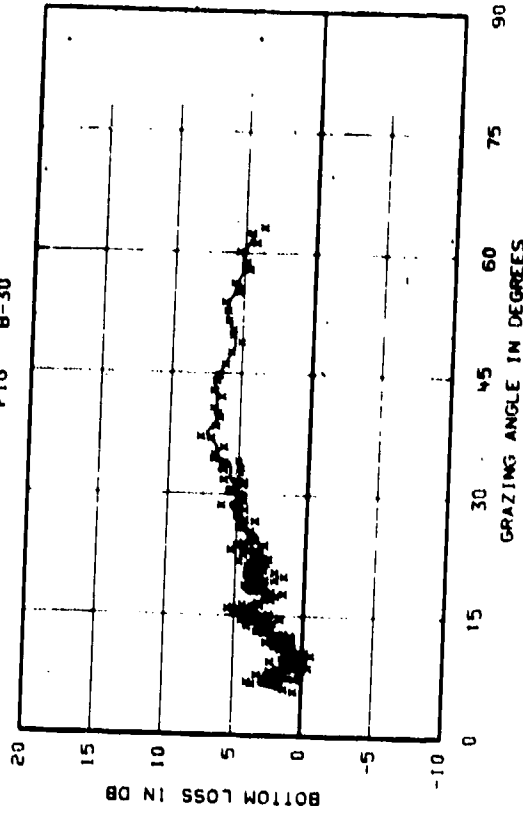
$F_c = 445.0 \text{ MHz}$  BANDWIDTH( 499.5 Hz )  
 FIG B-29



$F_c = 600.0 \text{ MHz}$  BANDWIDTH( 673.5 Hz )  
 FIG B-30

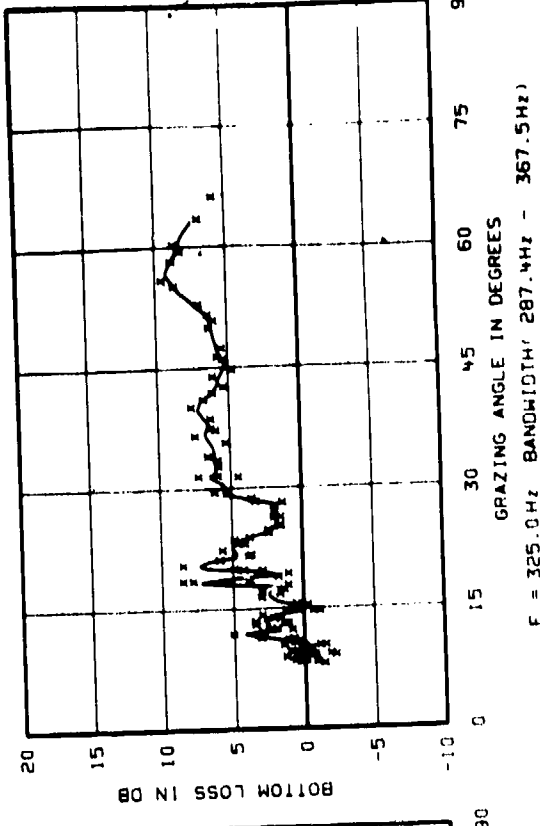
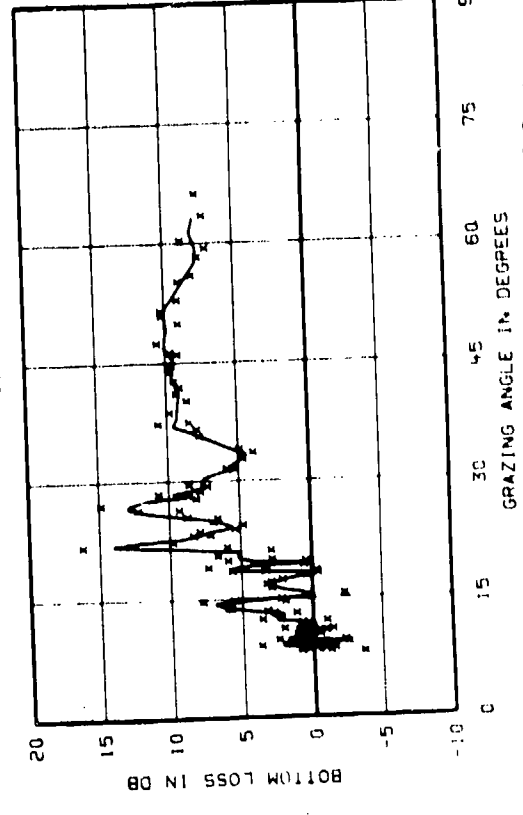
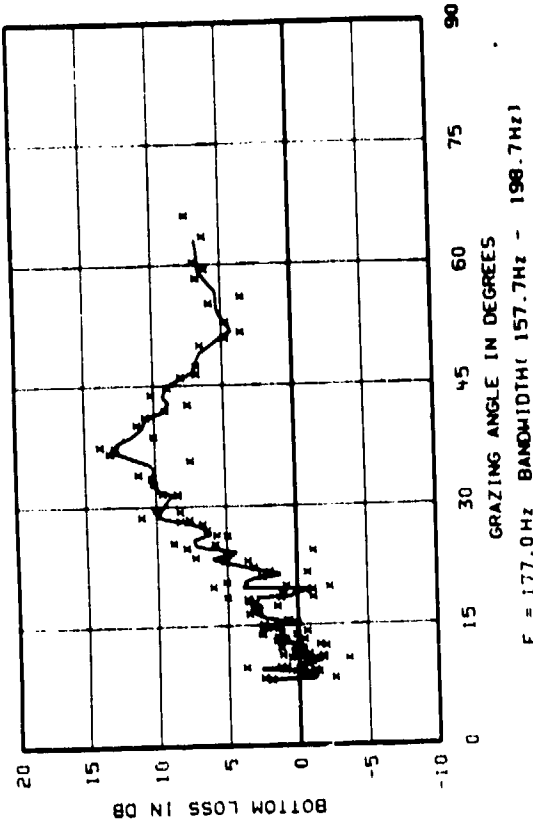
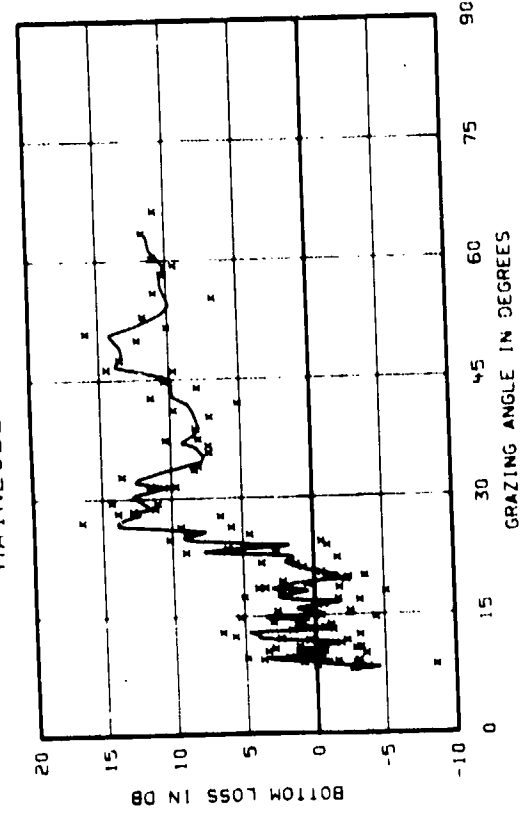


$F_c = 745.0 \text{ MHz}$  BANDWIDTH( 789.3 Hz )  
 FIG B-31



BROADBAND BANDWIDTH( 10.0 MHz )  
 BANDWIDTH( 750.0 Hz )  
 FIG B-32

MAINLOBE STATION BL-2 (28 30N 70 30W) 3353 METER RECEIVER



BOTTOM LOSS VS GRAZING ANGLE  
MAINLOBE STATION BL-2 (28 30N 70 30W) 3353 METER RECEIVER

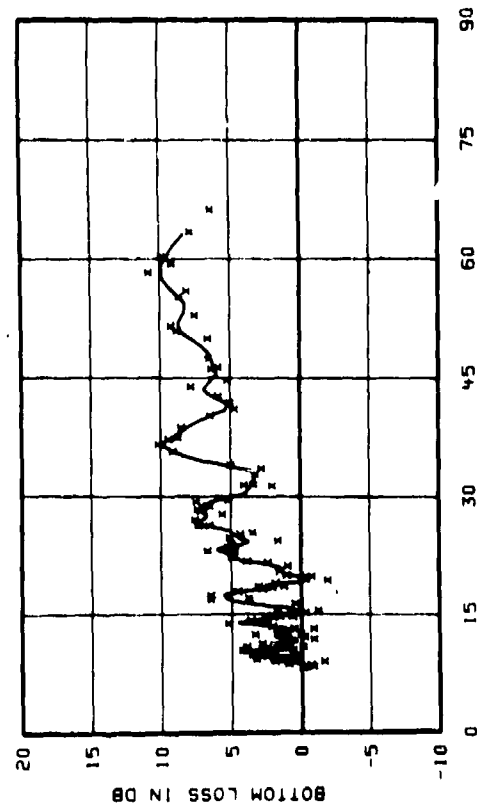


FIG B-37  
 $F_c = 499.5 \text{ Hz}$  BANDWIDTH( 396.4Hz - 499.5Hz)

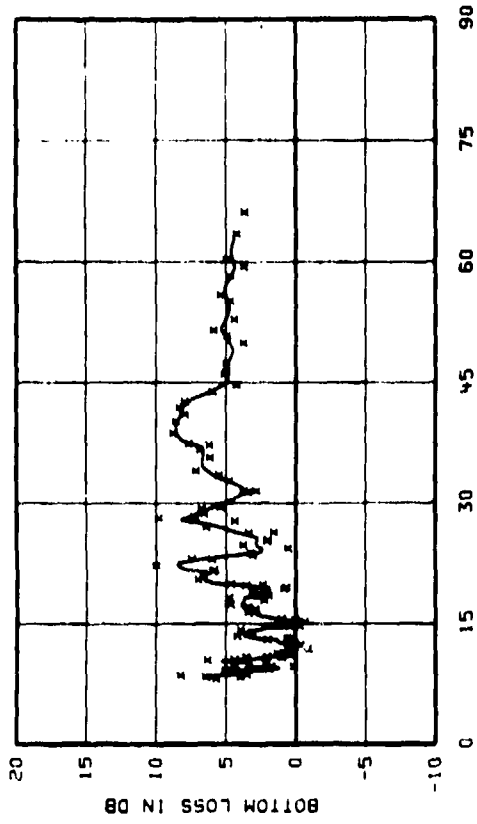


FIG B-38  
 $F_c = 673.5 \text{ Hz}$  BANDWIDTH( 534.5Hz - 673.5Hz)

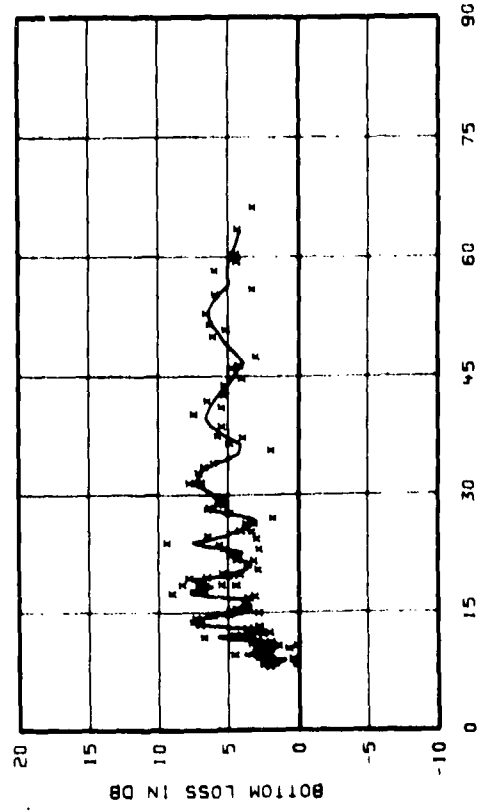


FIG B-39  
 $F_c = 789.3 \text{ Hz}$  BANDWIDTH( 703.2Hz - 789.3Hz)

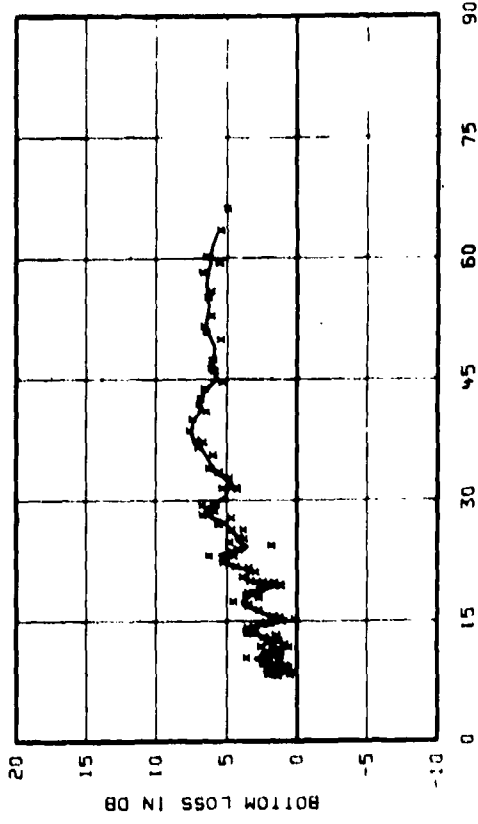
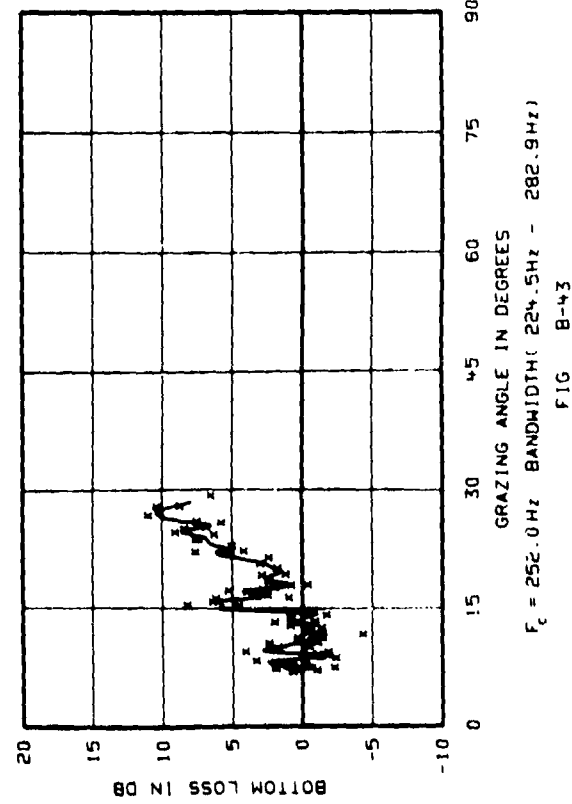
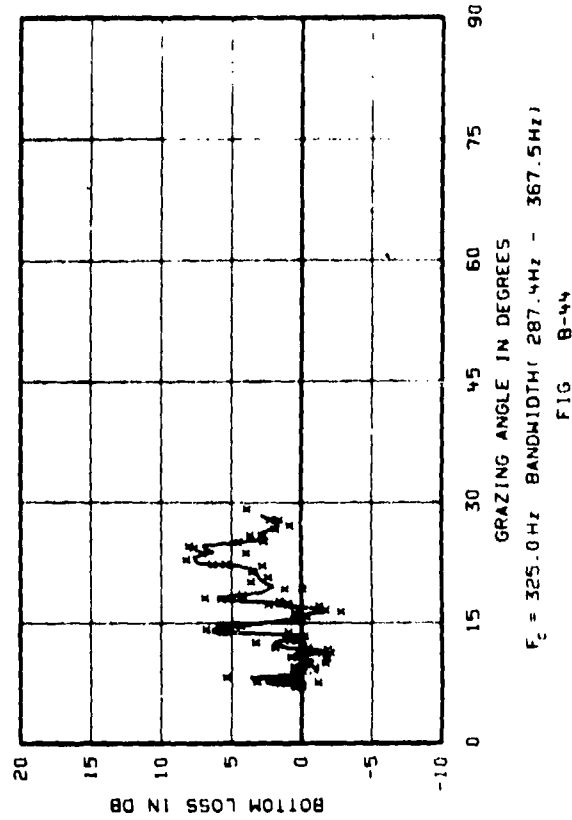
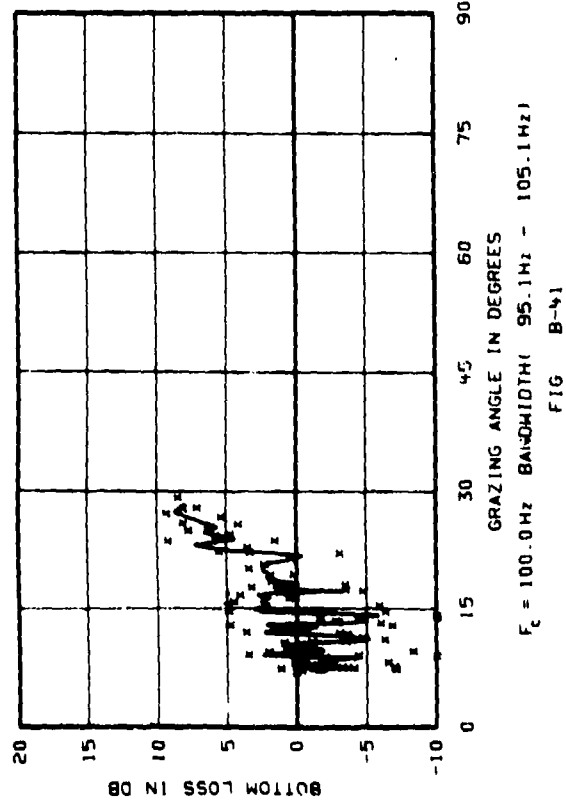
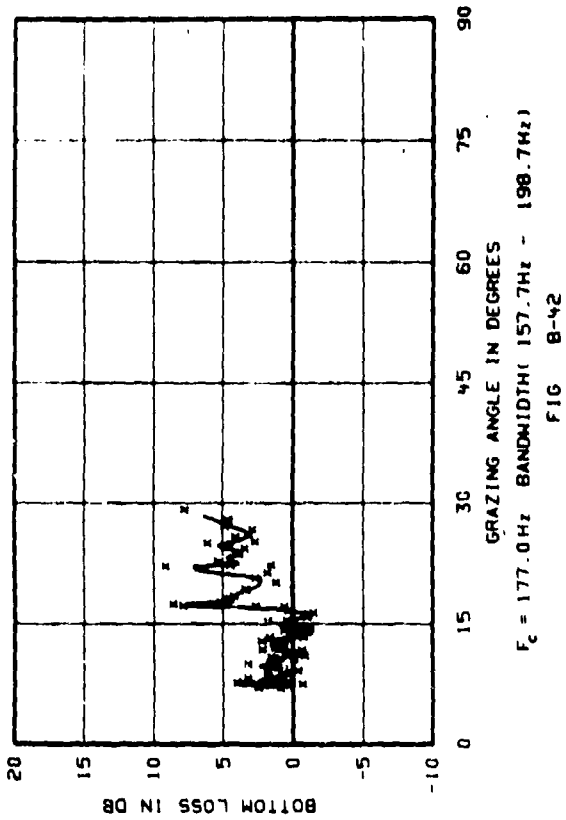


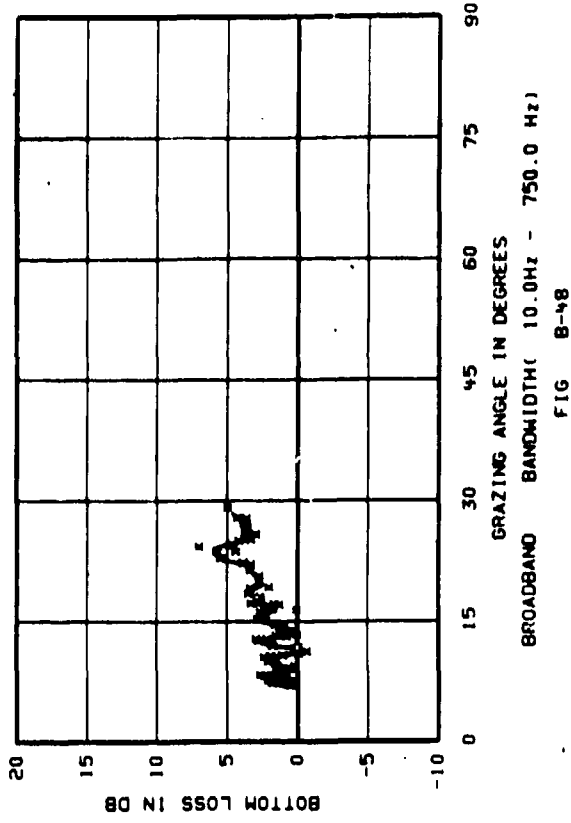
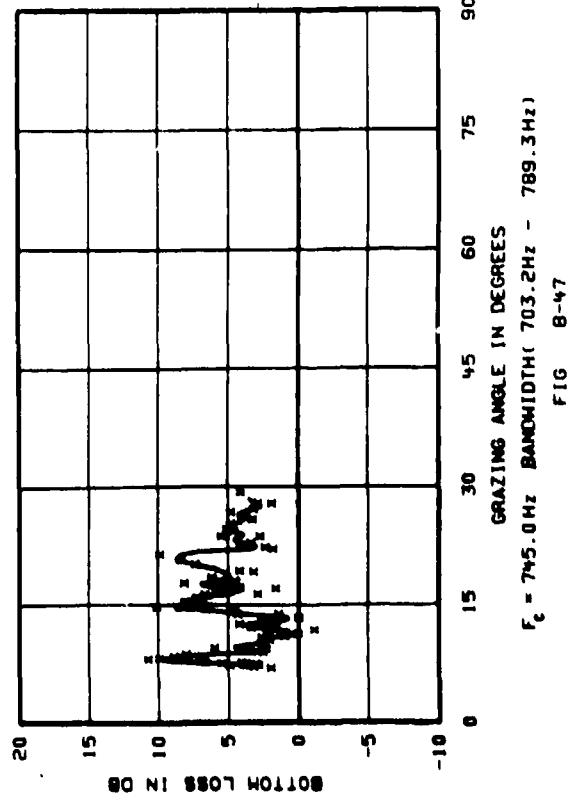
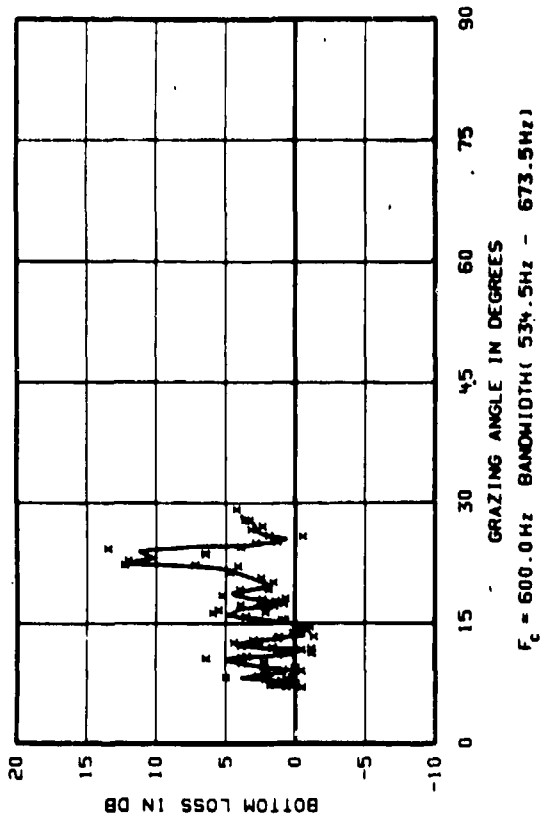
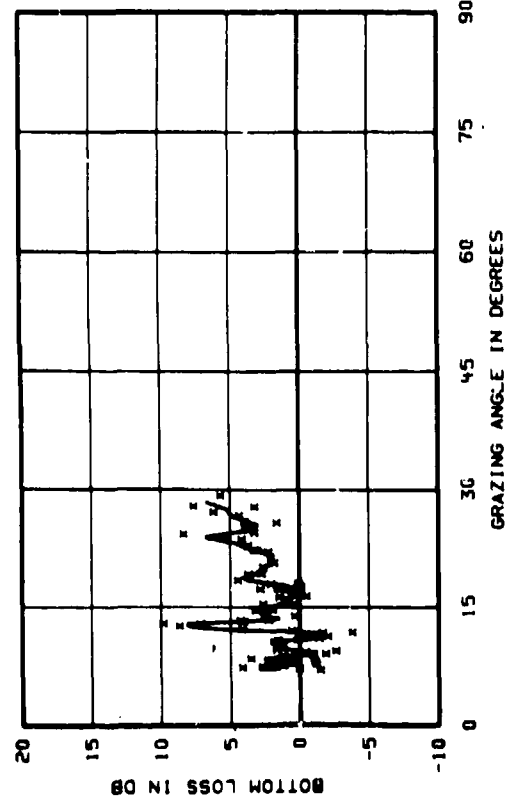
FIG B-40  
BROADBAND BANDWIDTH( 10.0Hz - 750.0 Hz)

BOTTOM LOSS VS GRAZING ANGLE  
MAINLOBE STATION BL-3 (29 00N 70 30W) 3363 METER RECEIVER

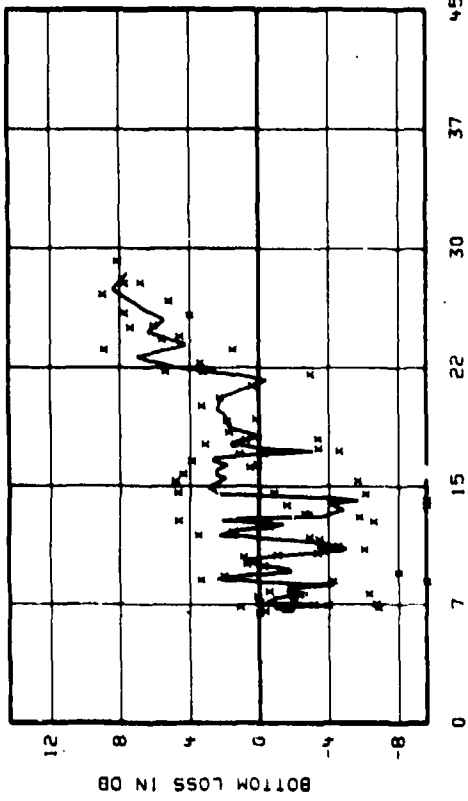
B-12



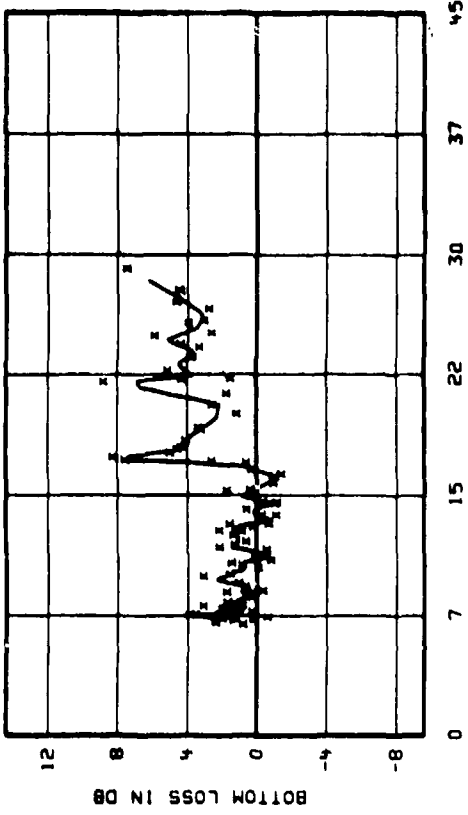
MAINLOBE STATION BL-3 (29 00N 70 30W) 3363 METER RECEIVER



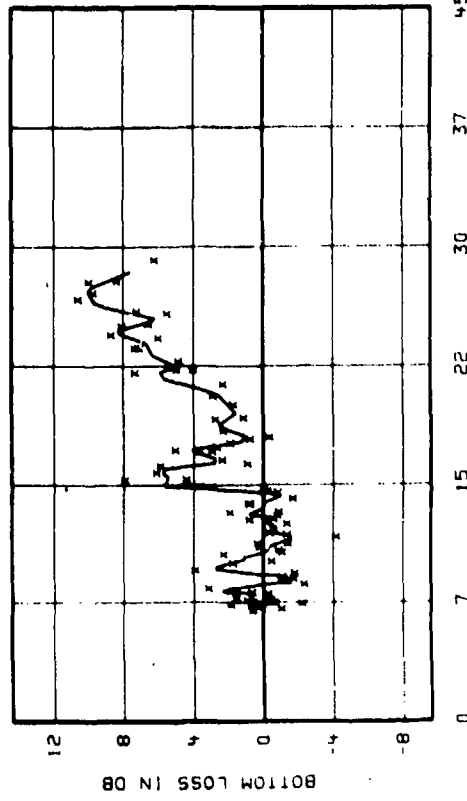
MAINLOBE STATION BL-3 (29 00N 70 30W) 3363 METER RECEIVER



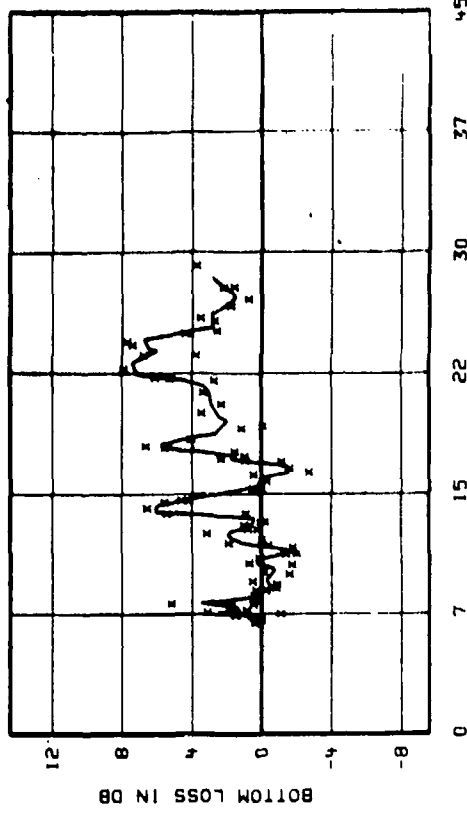
GRAZING ANGLE IN DEGREES  
 $F_c = 100.0 \text{ Hz}$  BANDWIDTH: 95.1 Hz - 105.1 Hz)  
 FIG B-49



GRAZING ANGLE IN DEGREES  
 $F_c = 177.0 \text{ Hz}$  BANDWIDTH: 157.7 Hz - 198.7 Hz)  
 FIG B-50



GRAZING ANGLE IN DEGREES  
 $F_c = 252.0 \text{ Hz}$  BANDWIDTH: 224.5 Hz - 282.9 Hz)  
 FIG B-51



GRAZING ANGLE IN DEGREES  
 $F_c = 325.0 \text{ Hz}$  BANDWIDTH: 287.4 Hz - 367.5 Hz)  
 FIG B-52

MAINLOBE STATION BL-3 (29 00N 70 30W) 3363 METER RECEIVER

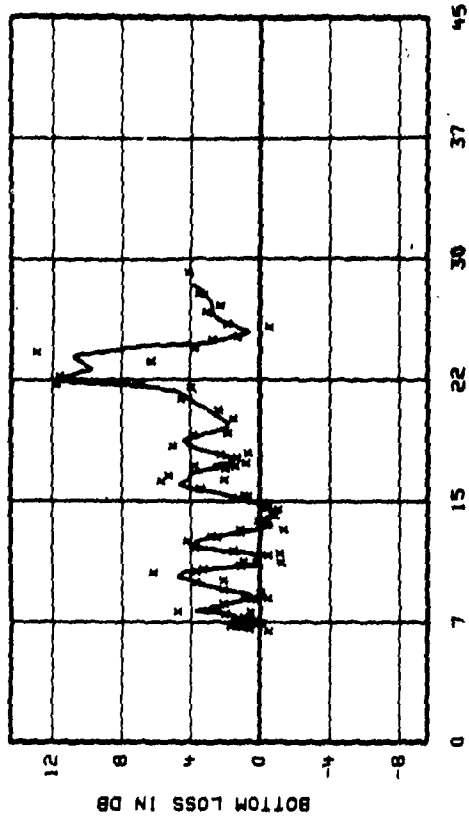


FIG 8-54  
 $f_c = 600.0 \text{ Hz}$  BANDWIDTH( 534.5Hz - 673.5Hz)

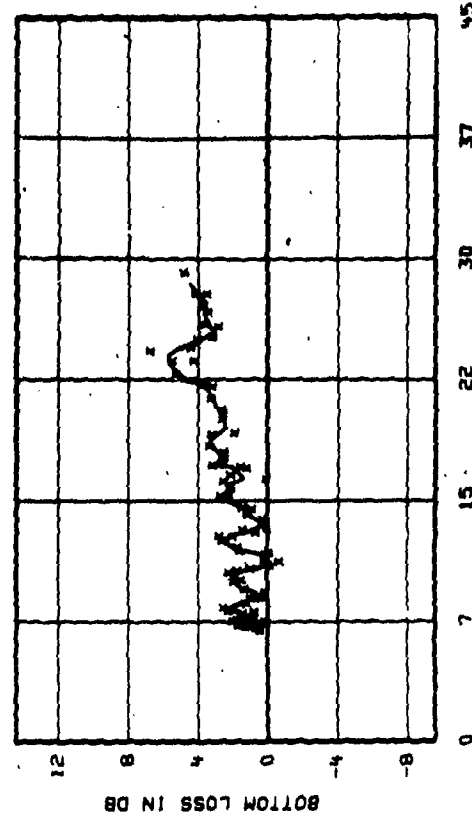


FIG 8-55  
 BROADBAND BANDWIDTH( 10.0Hz - 750.0 Hz)

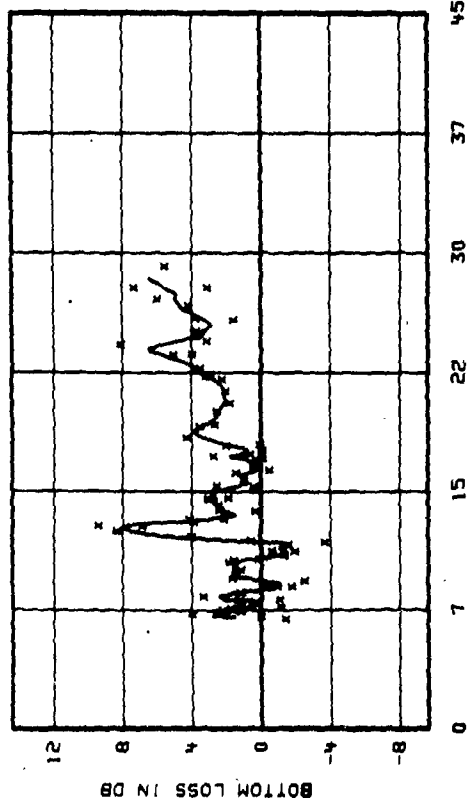


FIG 8-53  
 $f_c = 445.0 \text{ Hz}$  BANDWIDTH( 396.4Hz - 499.5Hz)

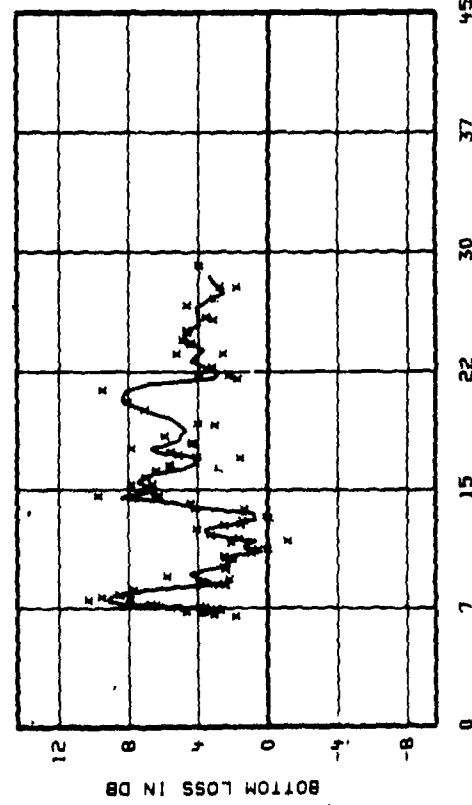
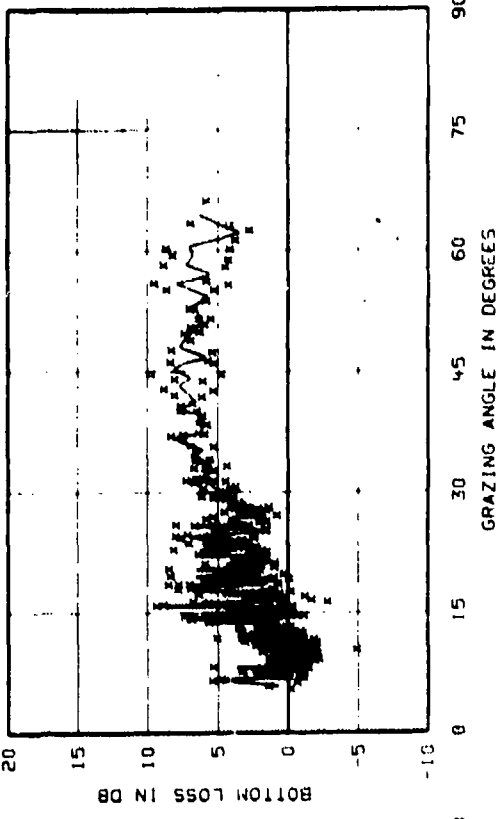
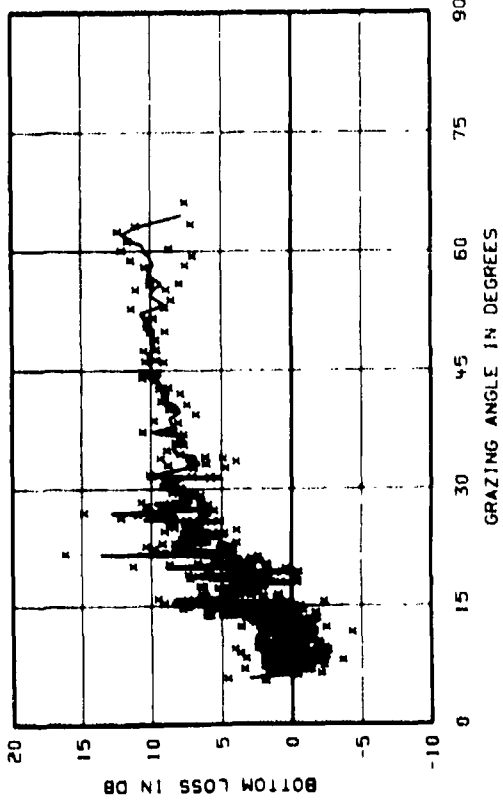
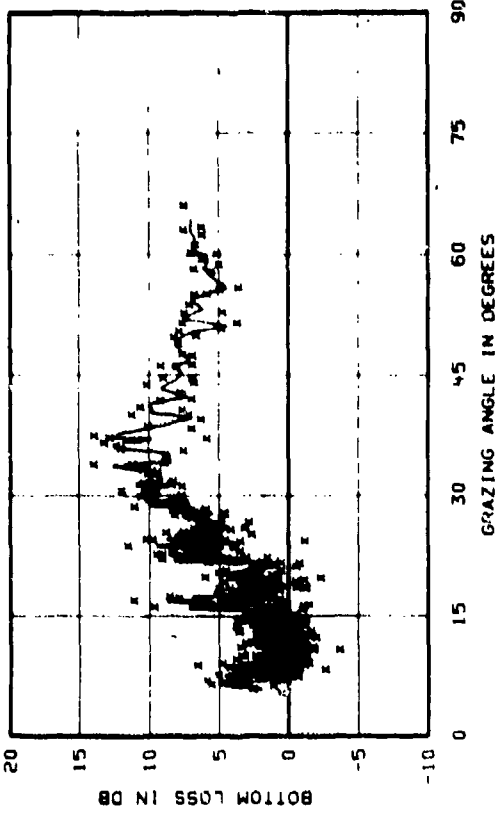
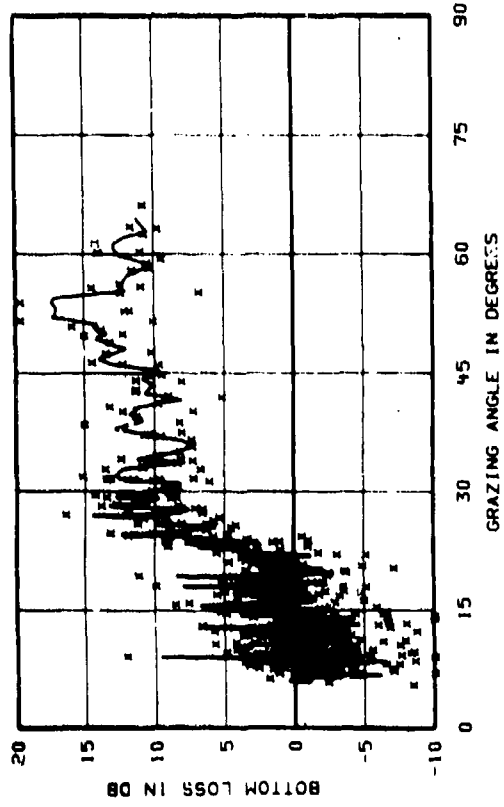


FIG 8-55  
 $f_c = 745.0 \text{ Hz}$  BANDWIDTH( 703.2Hz - 789.3Hz)

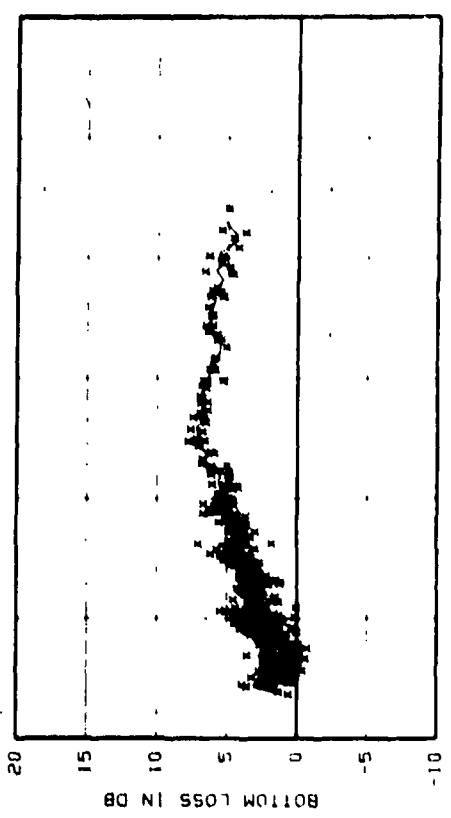
BOTTOM LOSS VS GRAZING ANGLE  
MAINLOBE COMBINED STATIONS BL-1(U), BL-U(L), BL-2, AND BL-3



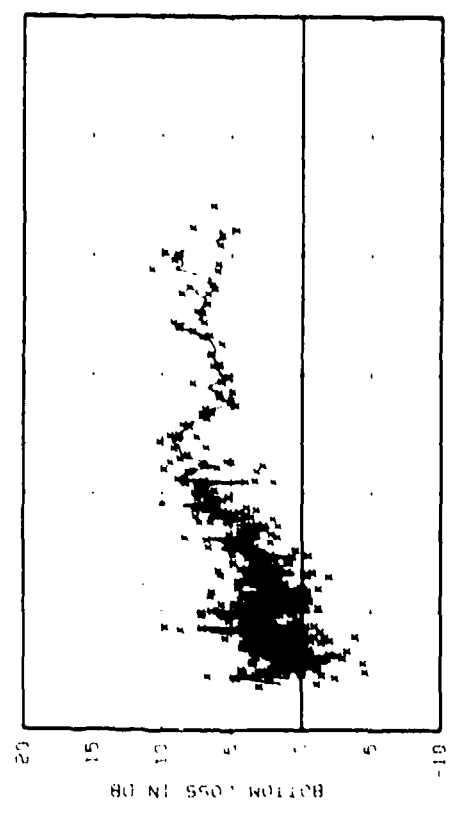
BOTTOM LOSS VS GRAZING ANGLE  
MAINLOBE COMBINED STATIONS BL-1(U), BL-U(L), BL-2, AND BL-3



GRAZING ANGLE IN DEGREES  
 $F_c = 524.5 \text{ Hz}$  BANDWIDTH: 524.5 Hz - 673.5 Hz  
FIG B-62



GRAZING ANGLE IN DEGREES  
BROADBAND BANDWIDTH: 10.0 Hz - 750.0 Hz  
FIG B-64



GRAZING ANGLE IN DEGREES  
 $F_c = 499.5 \text{ Hz}$  BANDWIDTH: 396.4 Hz - 499.5 Hz  
FIG B-61



GRAZING ANGLE IN DEGREES  
 $F_c = 789.3 \text{ Hz}$  BANDWIDTH: 733.2 Hz - 789.3 Hz  
FIG B-63

Appendix C  
SIXTH-ORDER POLYNOMIAL REPRESENTATIONS  
OF BOTTOM LOSS DATA

The sixth-order polynomial curves, which are shown in figures C-1 through C-32, were fitted to the corresponding three-point moving average curves of the bottom-loss data presented in appendix B. At station BL-1 the data from the combined AUTOBUOY receivers have been used in forming the polynomials given in table C-1. The polynomial expression for the determination of bottom-loss as a function of grazing angle  $\theta$  is given by

$$BL_{(\theta)} = X_0 + X_1\theta + X_2\theta^2 + \dots + X_6\theta^6, \quad (C-1)$$

where

BL = bottom loss (dB),

$\theta$  = bottom grazing angle (deg), and

$X_i$  = constants of polynomial expansion ( $i = 0, 1, 2, \dots, 6$ ).

Table C-1. Constants of Polynomial Expression for the Determination of Bottom Loss Versus Grazing Angle

Station BL-1 (Combined Receivers)				
Constants*	(Valid Grazing Angle Range: 5.8° to 62.1°)			
	Broadband (30-790 Hz) (Fig. C-1)**	100 Hz (Fig. C-2)	177 Hz (Fig. C-3)	252 Hz (Fig. C-4)
X <sub>0</sub>	.875214827 E+01	-.996819305 E+01	.141804373 E+02	.249716005 E+02
X <sub>1</sub>	-.242179233 E+01	.299106264 E+01	-.245824680 E+01	-.776497072 E+01
X <sub>2</sub>	.280501705 E+00	-.391519502 E+00	.127868425 E+00	.846308872 E+00
X <sub>3</sub>	-.143824805 E-01	.250281091 E-01	.391411595 E-05	-.409829742 E-01
X <sub>4</sub>	.378098823 E-03	-.751327345 E-03	-.117009775 E-03	.100516500 E-02
X <sub>5</sub>	-.491776893 E-05	.105527171 E-04	.243001486 E-05	-.121801005 E-04
X <sub>6</sub>	.249037244 E-07	-.561741080 E-07	-.148923927 E-07	.579131596 E-07
RMS Difference (dB)	+ 0.69	+ 2.87	+ 1.64	+ 1.39

Constants	Station BL-1 (Combined Receivers)		
	325 Hz (Fig. C-5)	445 Hz (Fig. C-6)	600 Hz (Fig. C-7)
X <sub>0</sub>	.224609866 E+02	-.866894865 E+01	.406983104 E+02
X <sub>1</sub>	-.705697352 E+01	.303438401 E+01	-.111192998 E+01
X <sub>2</sub>	.814366192 E+00	-.338486280 E+00	.116450271 E+01
X <sub>3</sub>	-.427845209 E-01	.183257326 E-01	-.575632718 E-01
X <sub>4</sub>	.113794157 E-02	-.486391502 E-03	.145763980 E-02
X <sub>5</sub>	-.148040177 E-04	.616504161 E-05	-.182157439 E-04
X <sub>6</sub>	.745440447 E-07	-.299346525 E-07	.888339899 E-07
RMS Difference (dB)	+ 1.45	+ 1.50	+ 1.49

Constants	Station BL-1 (Combined Receivers)	
	745 Hz (Fig. C-8)	745 Hz (Fig. C-8)
X <sub>0</sub>	.783022976 E+01	.783022976 E+01
X <sub>1</sub>	-.222431964 E+01	-.222431964 E+01
X <sub>2</sub>	.328629628 E+00	.328629628 E+00
X <sub>3</sub>	-.198238418 E-01	-.198238418 E-01
X <sub>4</sub>	.576876155 E-03	.576876155 E-03
X <sub>5</sub>	-.800266378 E-05	-.800266378 E-05
X <sub>6</sub>	.422778248 E-07	.422778248 E-07
RMS Difference (dB)	+ 2.32	+ 2.32

Table C-1. Constants of Polynomial Expansion for the Determination of Bottom Loss Versus Grazing Angle (Cont'd)

Station BL-2			
(Valid Grazing Angle Range: 8.14° to 63.11°)			
Constants	Broadband (90-790 Hz) (Fig. C-9)	100 Hz (Fig. C-10)	177 Hz (Fig. C-11)
		252 Hz (Fig. C-12)	
X <sub>0</sub>	-.573874915 E+01	-.327064214 E+02	-.245251811 E+02
X <sub>1</sub>	.187094015 E+01	.937724149 E+01	.682016575 E+01
X <sub>2</sub>	-.189635359 E+00	-.103299007 E+01	-.731356986 E+00
X <sub>3</sub>	.997438398 E-02	.553058935 E-01	.381499934 E-01
X <sub>4</sub>	-.261121451 E-03	-.147534334 E-02	-.977176867 E-03
X <sub>5</sub>	.327930826 E-05	.189866157 E-04	.119030954 E-04
X <sub>6</sub>	-.158164133 E-07	-.940503870 E-07	-.552458088 E-07
RMS Difference (dB)	+ 0.67	+ 2.49	+ 1.08
			+ 2.11
Constants	325 Hz (Fig. C-13)	445 Hz (Fig. C-14)	600 Hz (Fig. C-15)
			745 Hz (Fig. C-16)
X <sub>0</sub>	-.237087226 E+02	-.216302495 E+02	-.556942663 E+02
X <sub>1</sub>	.531366575 E+01	.619847584 E+01	-.125548052 E+02
X <sub>2</sub>	-.438213807 E+00	-.644709460 E+00	.110113597 E+01
X <sub>3</sub>	.189212477 E-01	.331093241 E-01	-.468022614 E-01
X <sub>4</sub>	-.438353134 E-03	-.864365065 E-03	.105043758 E-02
X <sub>5</sub>	.516014092 E-05	.110274624 E-04	-.119725554 E-04
X <sub>6</sub>	-.241661164 E-07	-.545182948 E-07	.544997509 E-07
RMS Difference (dB)	+ 1.41	+ 1.52	+ 1.53
			+ 1.20

Table C-1. Constants of Polynomial Expression for the Determination of Bottom Loss Versus Grazing Angle (cont'd)

Station BL-3			
(Valid Grazing Angle Range: 7.0° to 28.4°)			
Constants	Broadband (90-790 Hz) (Fig. C-17)	100 Hz (Fig. C-18)	177 Hz (Fig. C-19)
		252 Hz (Fig. C-20)	
X <sub>0</sub>	.297321839 E+02	-.181682774 E+03	-.577045708 E+02
X <sub>1</sub>	-.130850651 E+02	.717318676 E+02	.230068774 E+02
X <sub>2</sub>	.243859845 E+01	-.132087078 E+02	-.324075133 E+01
X <sub>3</sub>	-.233994871 E+00	.114505659 E+01	.200795468 E+00
X <sub>4</sub>	.120719894 E-01	-.533421817 E-01	-.502451253 E-02
X <sub>5</sub>	-.314386511 E-03	.127335728 E-02	.122607617 E-04
X <sub>6</sub>	.322914062 E-05	-.122158987 E-04	.890847296 E-06
RMS Difference (dB)	+ 0.70	+ 2.11	+ 1.41
			+ 1.49
Constants	325 Hz (Fig. C-21)	445 Hz (Fig. C-22)	600 Hz (Fig. C-23)
			745 Hz (Fig. C-24)
X <sub>0</sub>	.286842651 E+03	.453970509 E+03	.148855671 E+03
X <sub>1</sub>	-.117706892 E+03	-.186163340 E+03	-.738332911 E+02
X <sub>2</sub>	.192852466 E+02	.302855525 E+02	.144166272 E+02
X <sub>3</sub>	-.161596254 E+01	-.250387770 E+01	-.140372002 E+01
X <sub>4</sub>	.732111400 E-01	.111511655 E+00	.720836259 E-01
X <sub>5</sub>	-.170145417 E-02	-.254824644 E-02	-.185805486 E-02
X <sub>6</sub>	.158700689 E-04	.234505060 E-04	.188925467 E-04
RMS Difference (dB)	+ 1.77	+ 1.75	+ 1.95
			+ 1.75

Table C-1. Constants of Polynomial Expression for the Determination of Bottom Loss Versus Grazing Angle (cont'd)

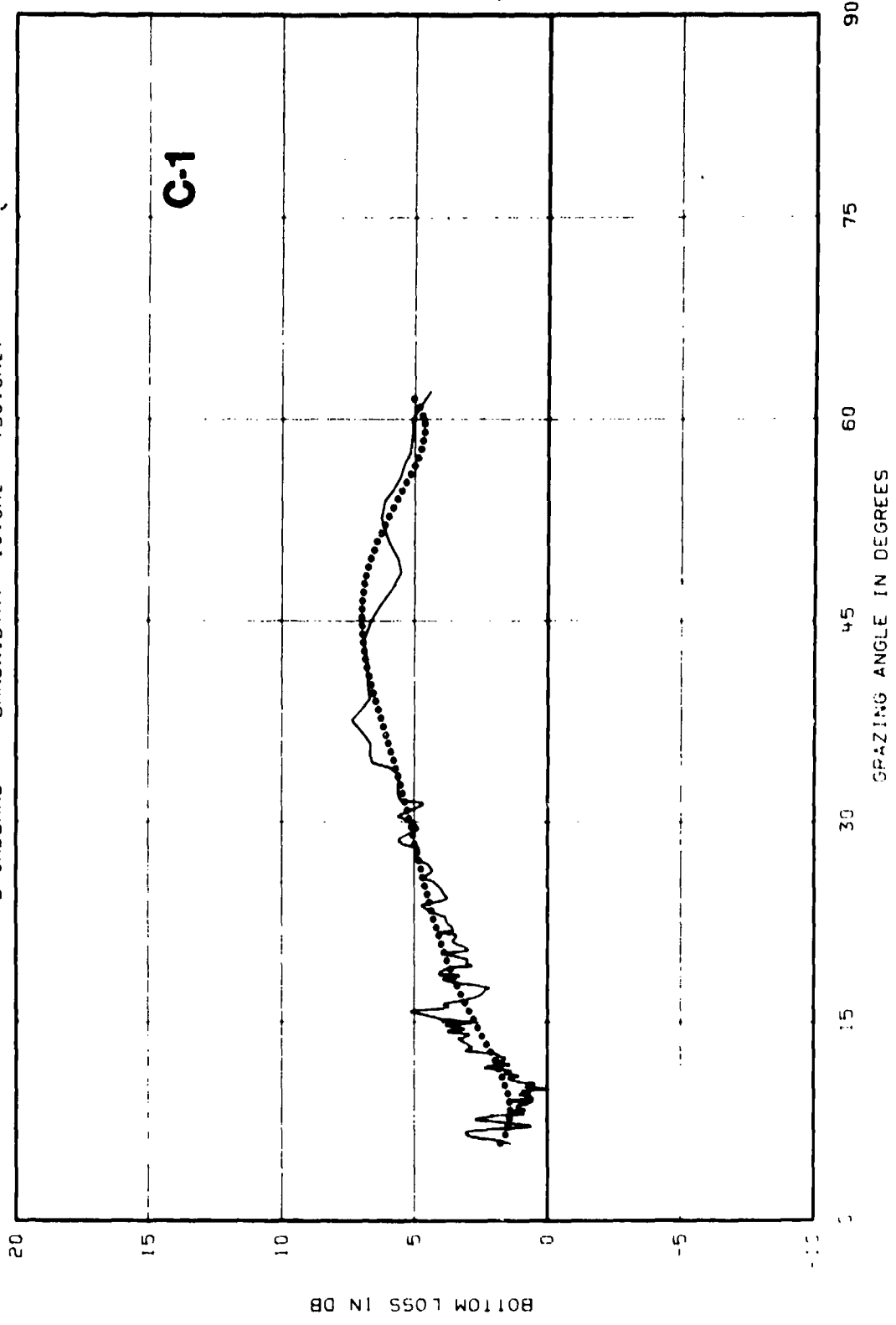
Combined Stations BL-1, BL-2, and BL-3						
(Valid Grazing Angle Range: 5.8° to 64.0°)						
Constants	Broadband (90-790 Hz) (Fig. C-25)	100 Hz (Fig. C-26)	177 Hz (Fig. C-27)	252 Hz (Fig. C-28)		
X <sub>0</sub>	.560086393 E+01	-.113910916 E+02	.121729850 E+02	.179510930 E+02		
X <sub>1</sub>	-.132892999 E+01	.322699046 E+01	-.223816055 E+01	-.541475642 E+01		
X <sub>2</sub>	.144024288 E+00	-.398151614 E+00	.132135527 E+00	.566338584 E+00		
X <sub>3</sub>	-.662424578 E-02	.243508061 E-01	-.173084228 E-02	-.255201887 E-01		
X <sub>4</sub>	.160135764 E-03	-.706230974 E-03	-.311854646 E-04	.577666142 E-03		
X <sub>5</sub>	-.197024147 E-05	.960723980 E-05	.833508729 E-06	-.644278492 E-05		
X <sub>6</sub>	.960718716 E-08	-.495682637 E-07	-.466745176 E-08	.281617416 E-07		
RMS Difference (db)	+ 0.63	+ 2.55	+ 1.50	+ 1.56		
Constants	325 Hz (Fig. C-29)	445 Hz (Fig. C-30)	600 Hz (Fig. C-31)	745 Hz (Fig. C-32)		
X <sub>0</sub>	.162710426 E+02	-.115514543 E+02	.303867466 E+02	.129873908 E+02		
X <sub>1</sub>	-.497141385 E+01	.372512093 E+01	-.777050853 E+01	-.311559811 E+01		
X <sub>2</sub>	.558345005 E+00	-.401805848 E+00	.775966026 E+00	.371003885 E+00		
X <sub>3</sub>	-.280752869 E-01	.212145394 E-01	-.364346607 E-01	-.197046443 E-01		
X <sub>4</sub>	.713506866 E-03	-.557084131 E-03	.881444132 E-03	.522186820 E-03		
X <sub>5</sub>	-.888792090 E-05	.704795542 E-05	-.105926100 E-04	-.672778395 E-05		
X <sub>6</sub>	.429866902 E-07	-.343035689 E-07	.499146622 E-07	.334563537 E-07		
RMS Difference (db)	+ 1.46	+ 1.42	+ 1.60	+ 1.88		

\* In FORTRAN scientific notation, base 10.

\*\* Designations within parentheses indicate corresponding appendix C figure numbers.

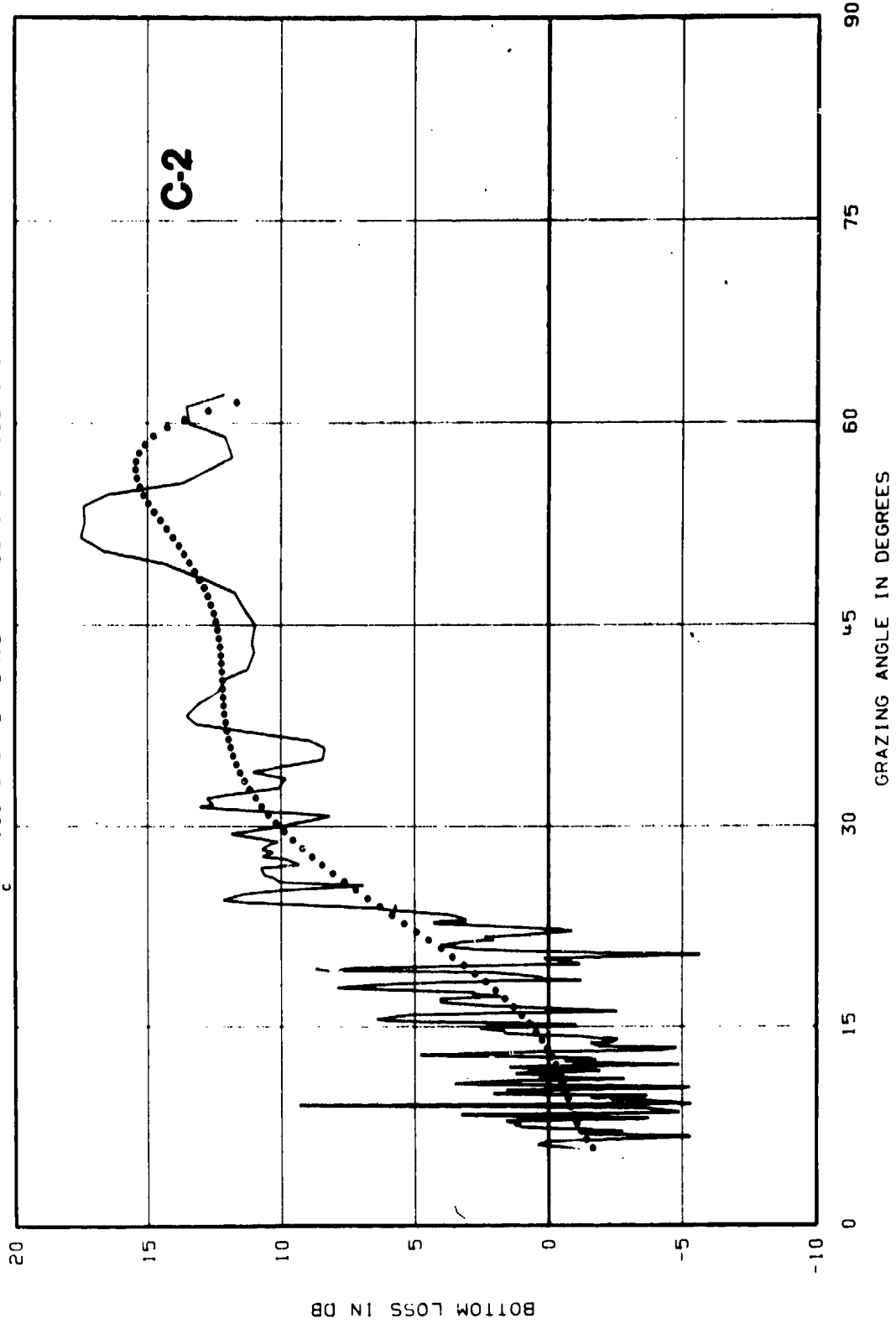
\*\*\* With respect to difference between polynomial values and values for 3-point moving average if nine significant digits are used for X<sub>i</sub>. (If only five significant digits are used, polynomial evaluations can differ by as much as 1.5 dB for larger values of 0).

BOTTOM LOSS VS GRAZING ANGLE  
MAINLOBE STATION BL-1 (28 08N 70 30W) COMBINED RECEIVERS  
SOLID LINE-3 PT. MOVING AVG, DOTTED LINE-POLYNOMIAL (ORDER 6)  
BROADBAND BANDWIDTH( 10.0Hz - 750.0Hz)

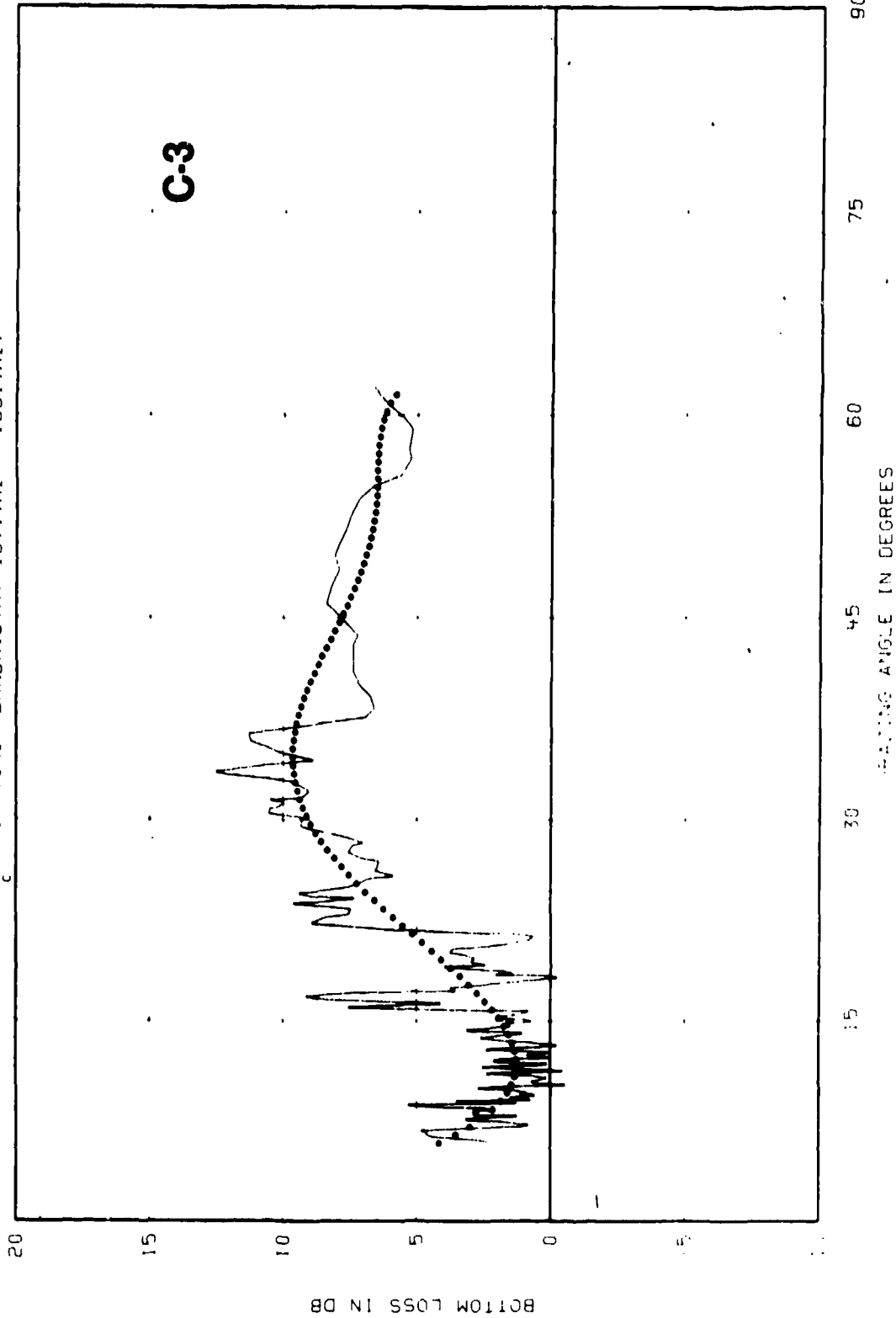


C-1

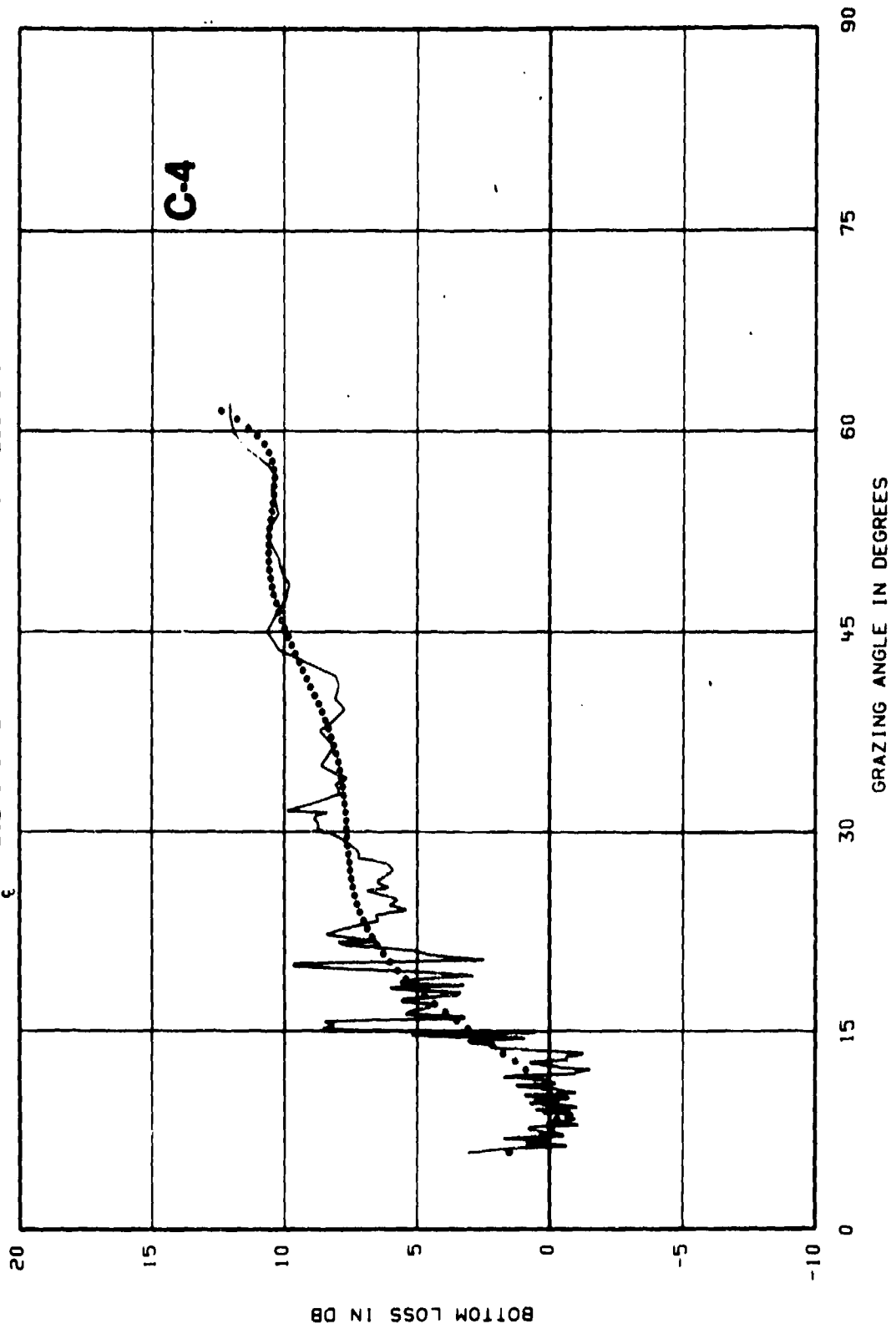
BOTTOM LOSS VS GRAZING ANGLE  
MAINLOBE STATION BL-1 (28 08N 70 30W) COMBINED RECEIVERS  
SOLID LINE-3 PT. MOVING AVG, DOTTED LINE-POLYNOMIAL (ORDER 6)  
 $F_c = 100.0\text{Hz}$  BANDWIDTH( 95.1Hz - 105.1Hz)



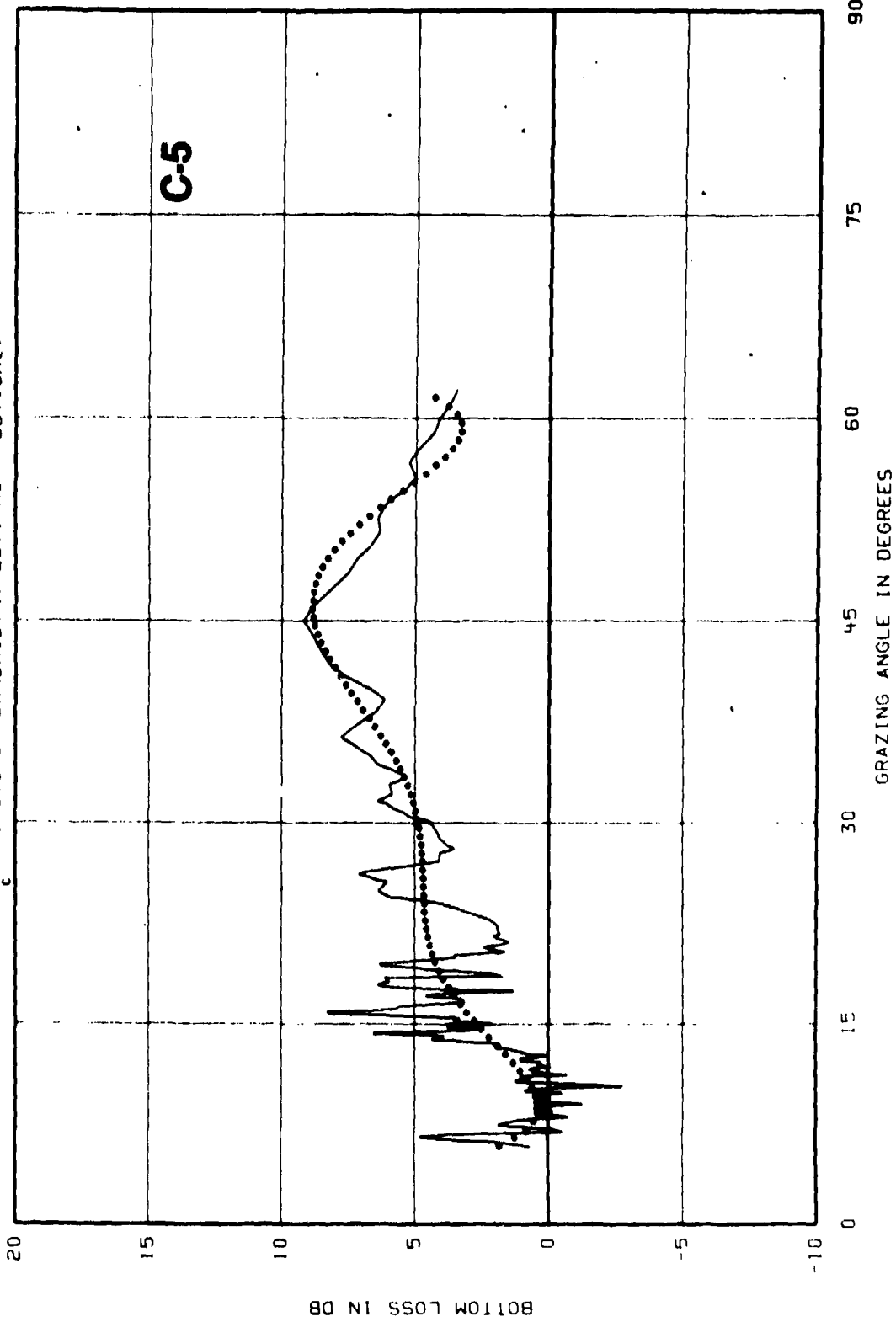
BOTTOM LOSS VS GRAZING ANGLE  
MAINLOBE STATION BL-1 (28 08N 70 30W) COMBINED RECEIVERS  
SOLID LINE-3 PT. MOVING AVG, DOTTED LINE-POLYNOMIAL (ORDER 6)  
 $F_c = 177.0\text{Hz}$  BANDWIDTH 157.7Hz - 198.7Hz



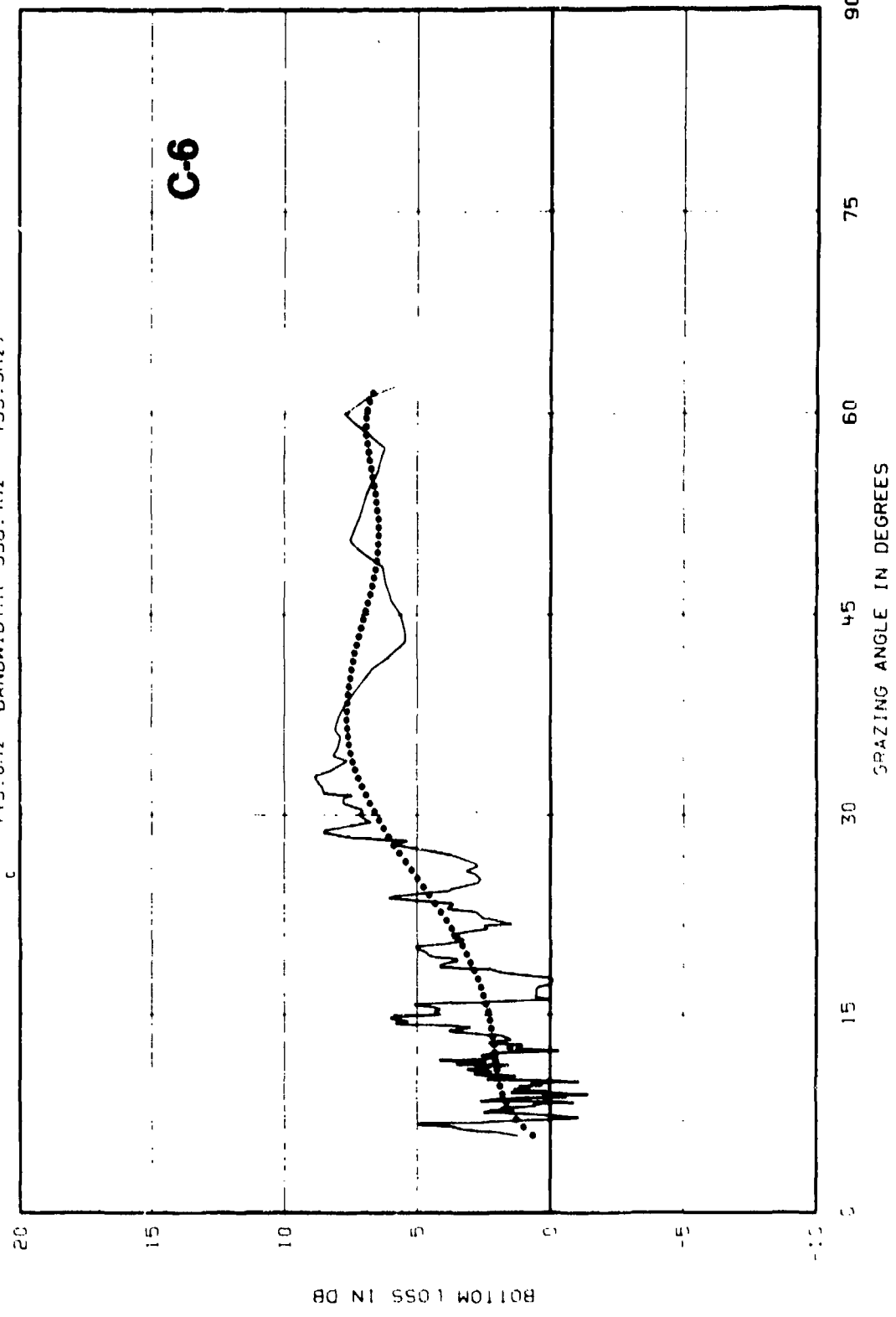
BOTTOM LOSS VS GRAZING ANGLE  
MAINLOBE STATION BL-1 (28 08N 70 30W) COMBINED RECEIVERS  
SOLID LINE-3 PT. MOVING AVG, DOTTED LINE-POLYNOMIAL (ORDER 6)  
 $f_c = 252.0\text{Hz}$  BANDWIDTH( 224.5Hz - 282.9Hz)



BOTTOM LOSS VS GRAZING ANGLE  
MAINLOBE STATION BL-1 (28 08N 70 30W) COMBINED RECEIVERS  
SOLID LINE-3 PT. MOVING AVG, DOTTED LINE-POLYNOMIAL (ORDER 6)  
 $F_c = 325.0\text{Hz}$  BANDWIDTH( 287.4Hz - 367.5Hz)

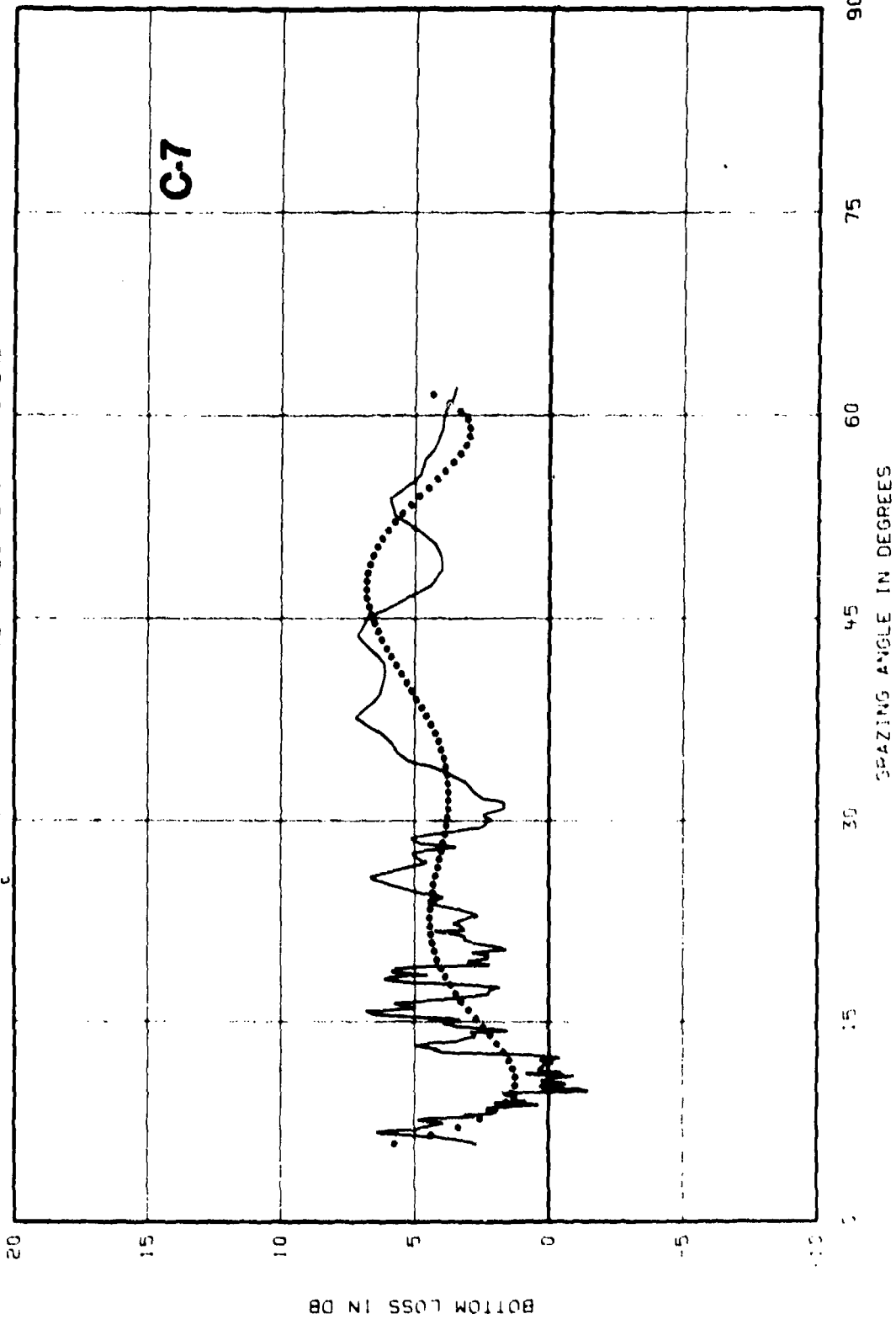


BOTTOM LOSS VS GRAZING ANGLE  
MAINLOBE STATION BL-1 (28 08N 70 30W) COMBINED RECEIVERS  
SOLID LINE-3 PT. MOVING AVG, DOTTED LINE-POLYNOMIAL (ORDER 6)  
 $F_c = 445.0\text{Hz}$  BANDWIDTH( 396.4Hz - 499.5Hz)

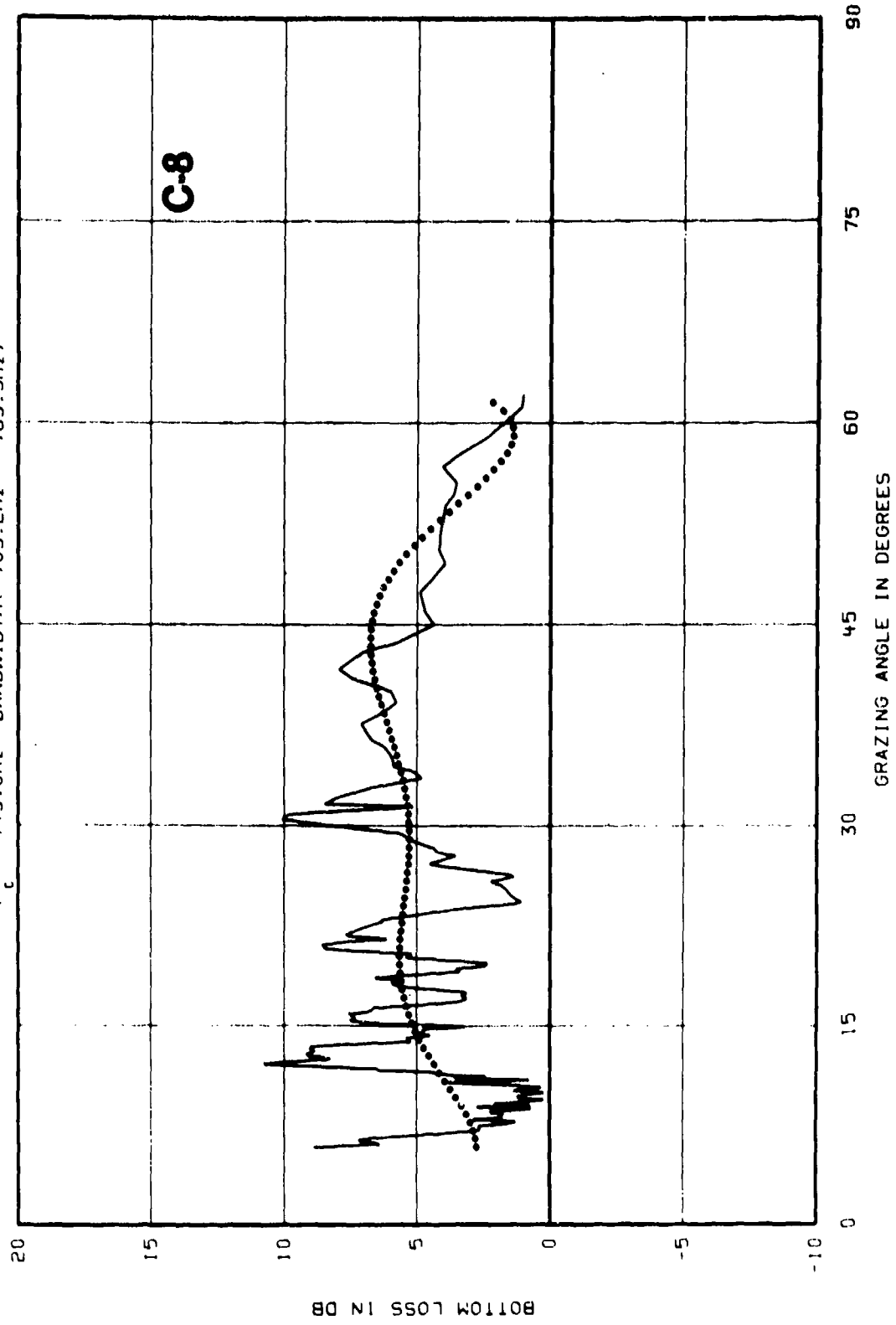


BOTTOM LOSS VS GRAZING ANGLE  
MAINLOBE STATION BL-1 (28 08N 70 30W) COMBINED RECEIVERS  
SOLID LINE-3 PT. MOVING AVG., DOTTED LINE-POLYNOMIAL (ORDER 6)

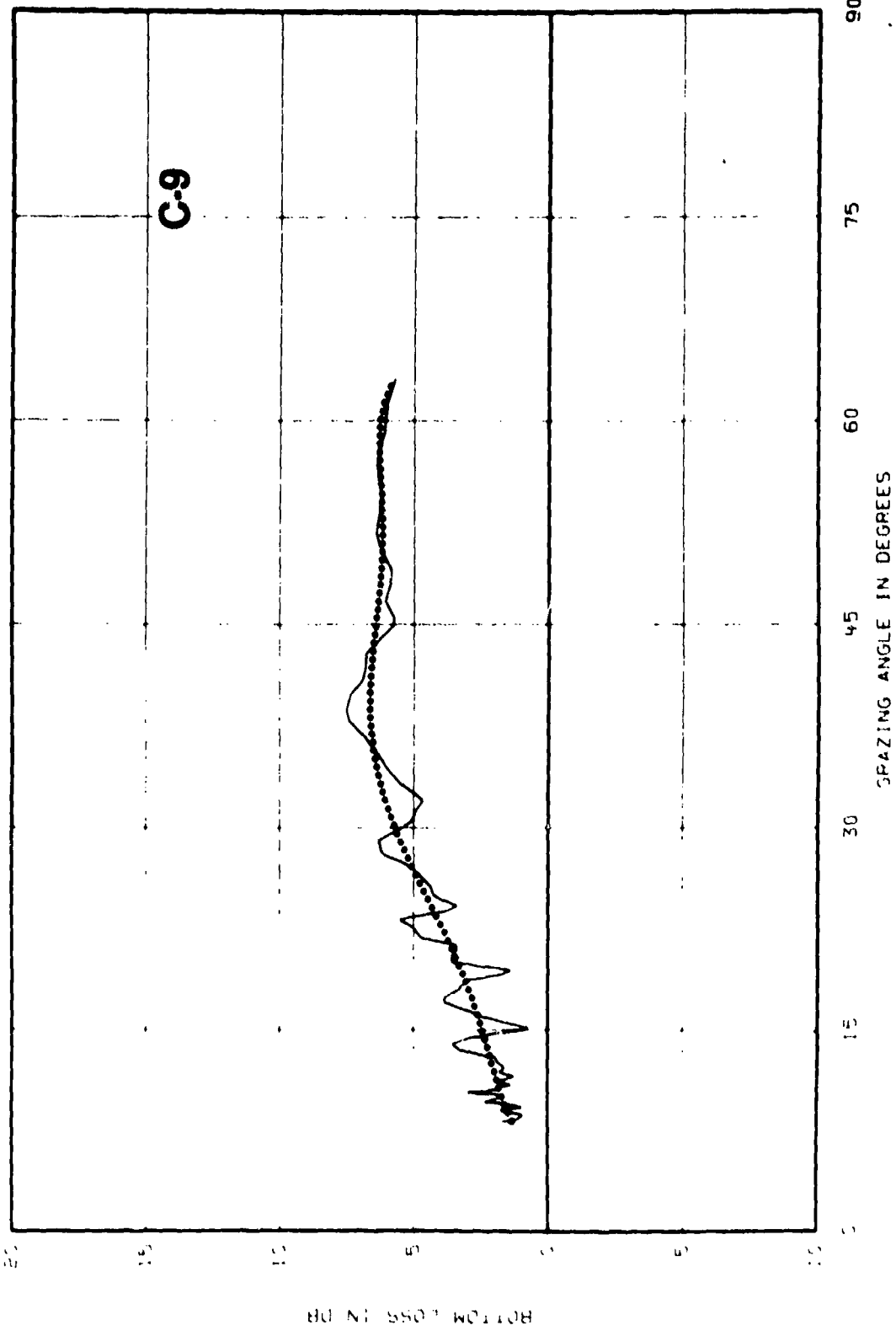
$F_c = 600.0\text{Hz}$  BANDWIDTH( 534.5Hz - 673.5Hz)



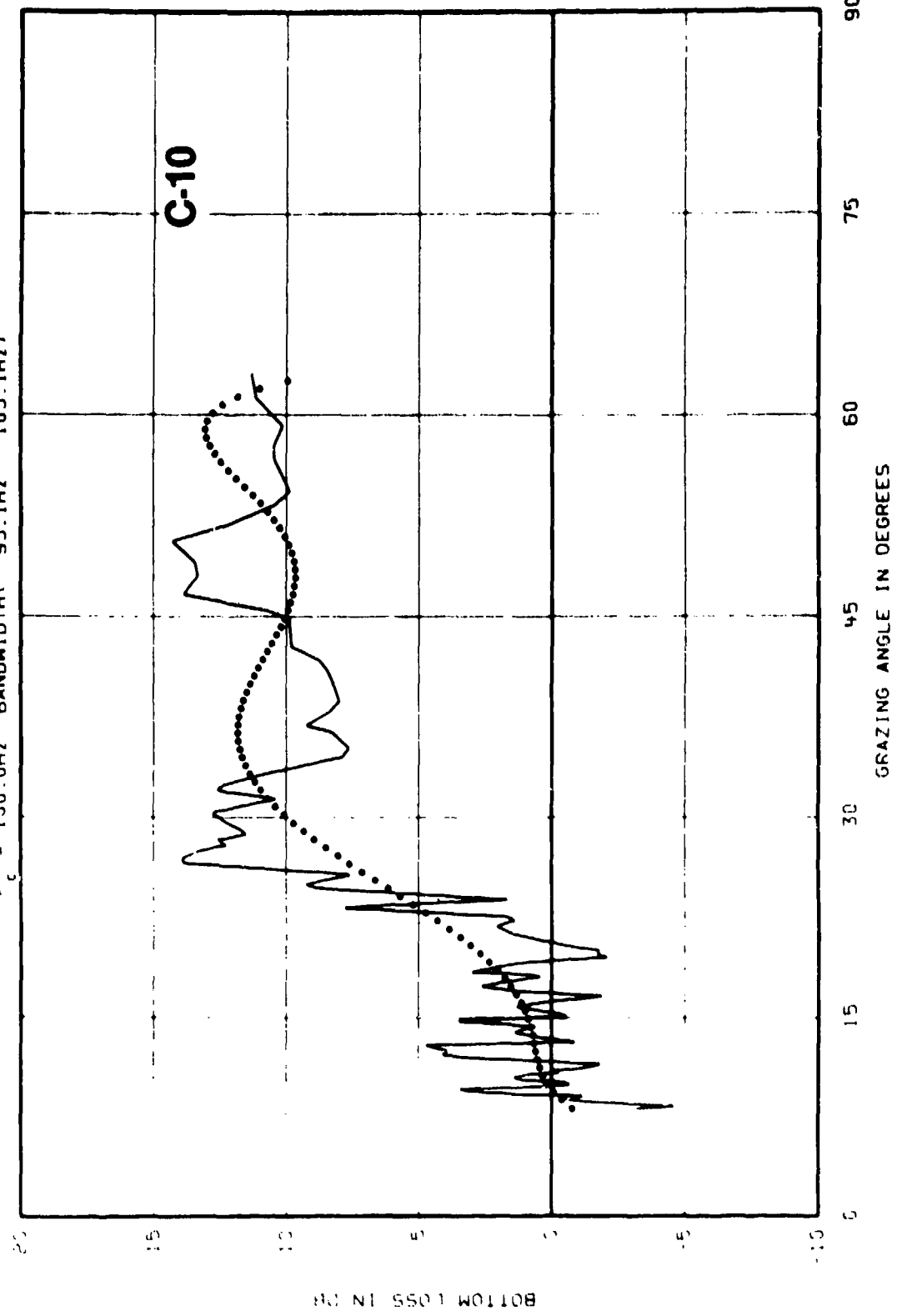
BOTTOM LOSS VS GRAZING ANGLE  
MAINLOBE STATION BL-1 (28 08N 70 30W) COMBINED RECEIVERS  
SOLID LINE-3 PT. MOVING AVG, DOTTED LINE-POLYNOMIAL (ORDER 6)  
 $F_c = 745.0\text{Hz}$  BANDWIDTH( 703.2Hz - 789.3Hz)



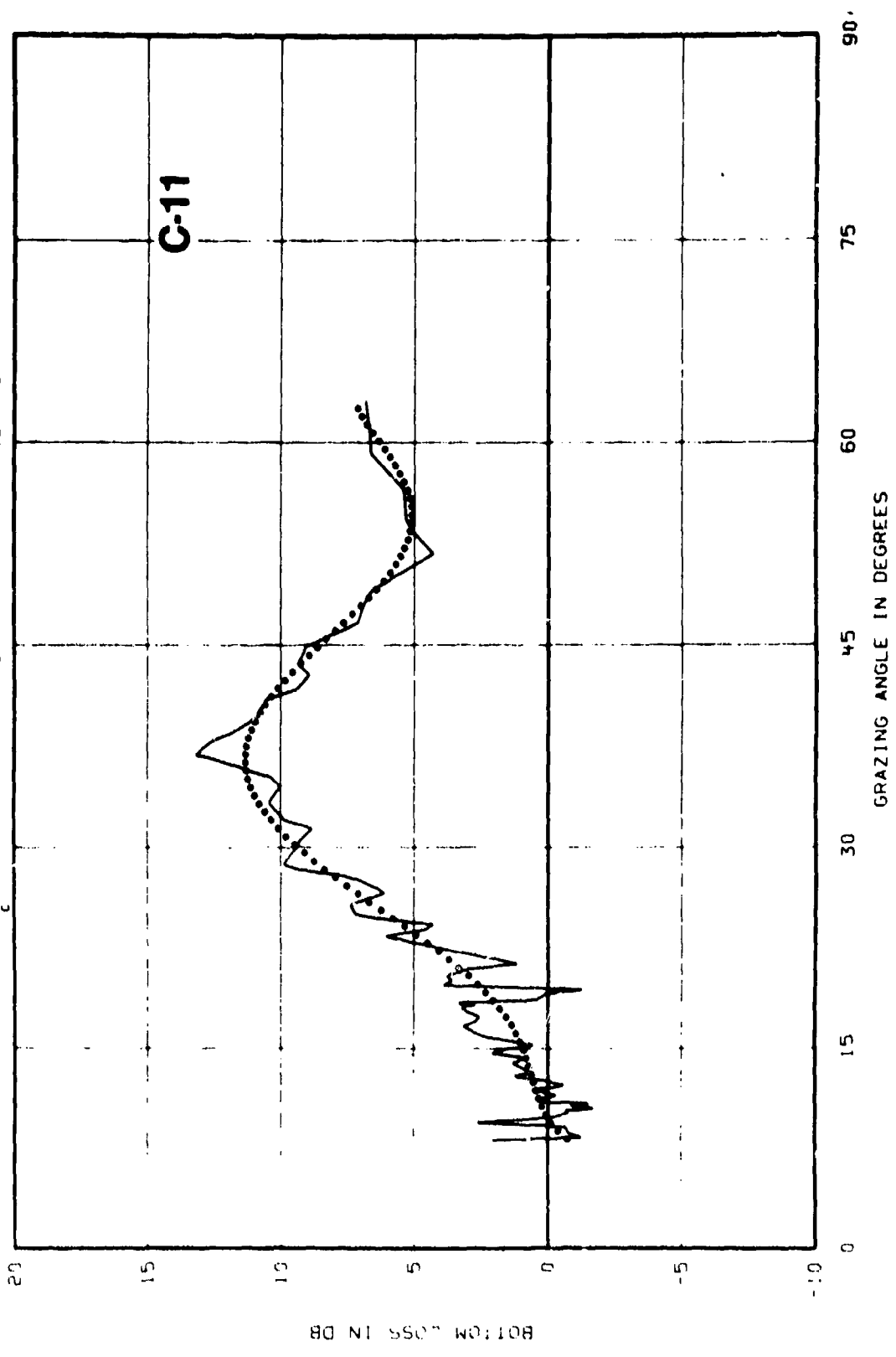
BOTTOM LOSS VS GRAZING ANGLE  
MAIN LOBE STATION BL-2 (28 30N 70 30W) 3353 METER RECEIVER  
SOLID LINE - 3 PT. MOVING AVG. DOTTED LINE - POLYNOMIAL (ORDER 6)  
BROADBAND BANDWIDTH: 10.0Hz - 750.0Hz



BOTTOM LOSS VS GRAZING ANGLE  
MAINLOBE STATION BL-2 (28 30N 70 30W) 3353 METER RECEIVER  
30.10 LINE-3 PT. MOVING AVG, DOTTED LINE-POLYNOMIAL (ORDER 6)  
F<sub>c</sub> = 100.0Hz BANDWIDTH( 95.1Hz - 105.1Hz)

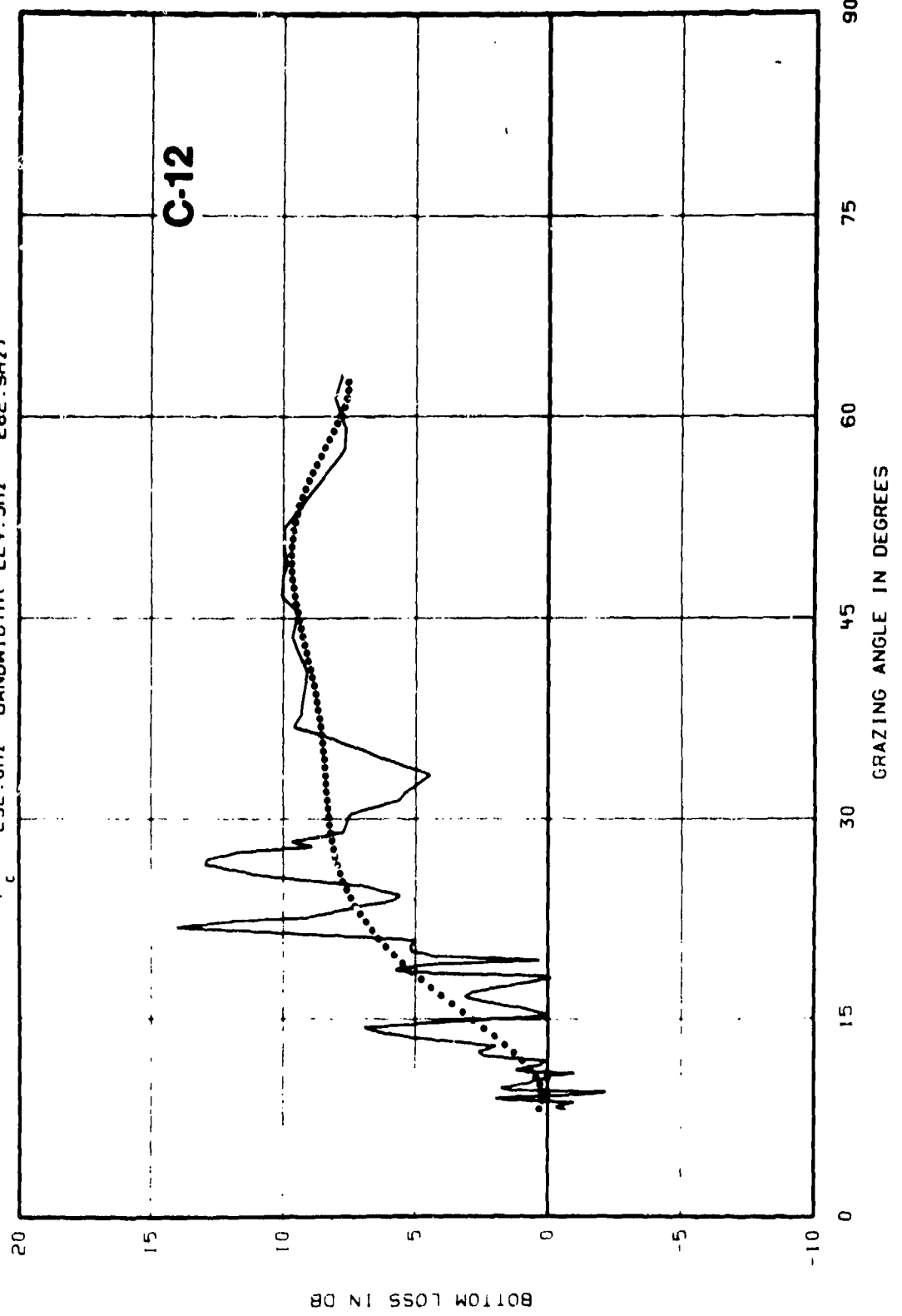


BOTTOM LOSS VS GRAZING ANGLE  
MAINLOBE STATION BL-2 (28 30N 70 30W) 3353 METER RECEIVER  
SOLID LINE-3 PT. MOVING AVG, DOTTED LINE-POLYNOMIAL (ORDER 6)  
 $F_c = 177.0\text{Hz}$  BANDWIDTH( 157.7Hz - 198.7Hz)

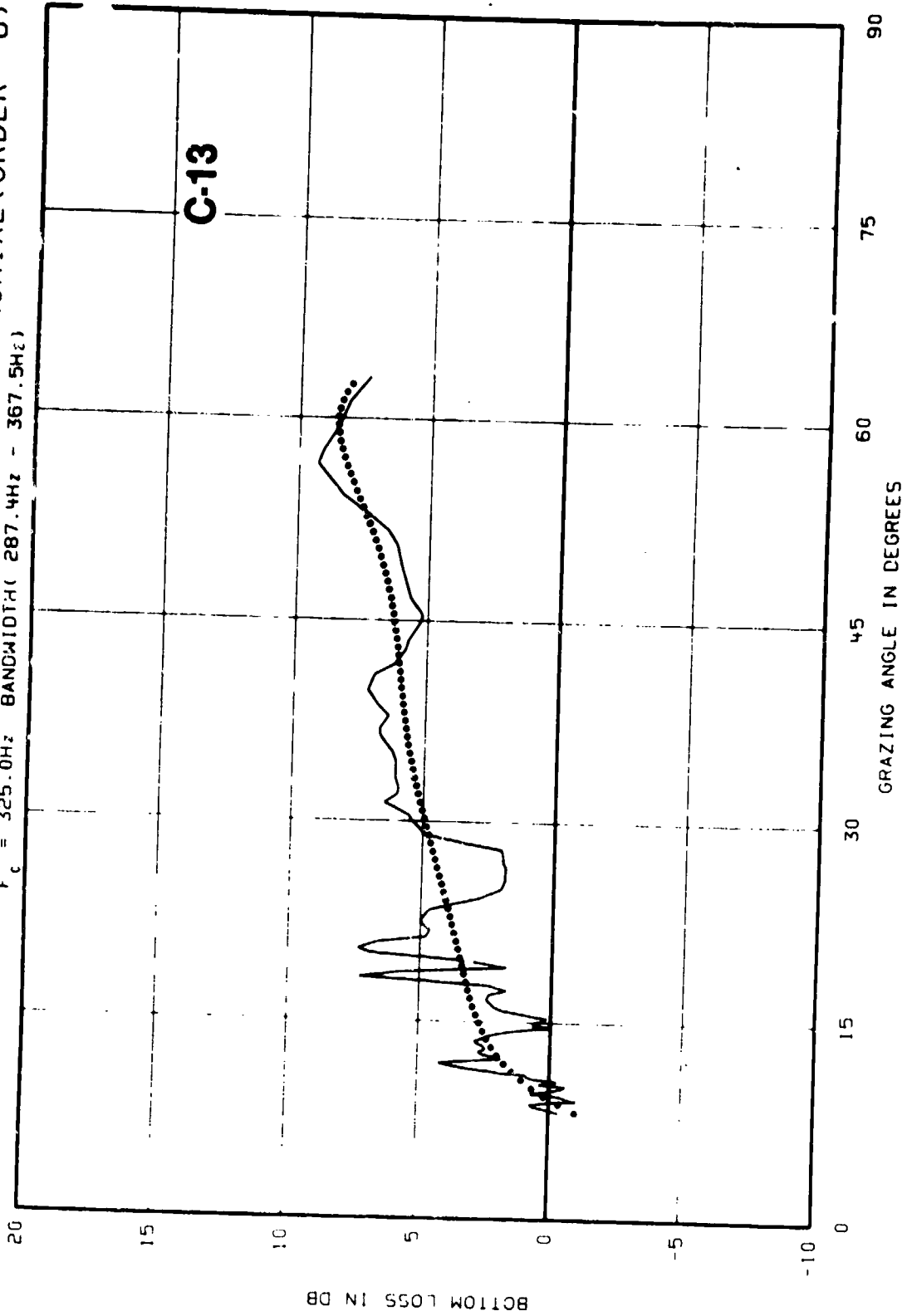


C-11

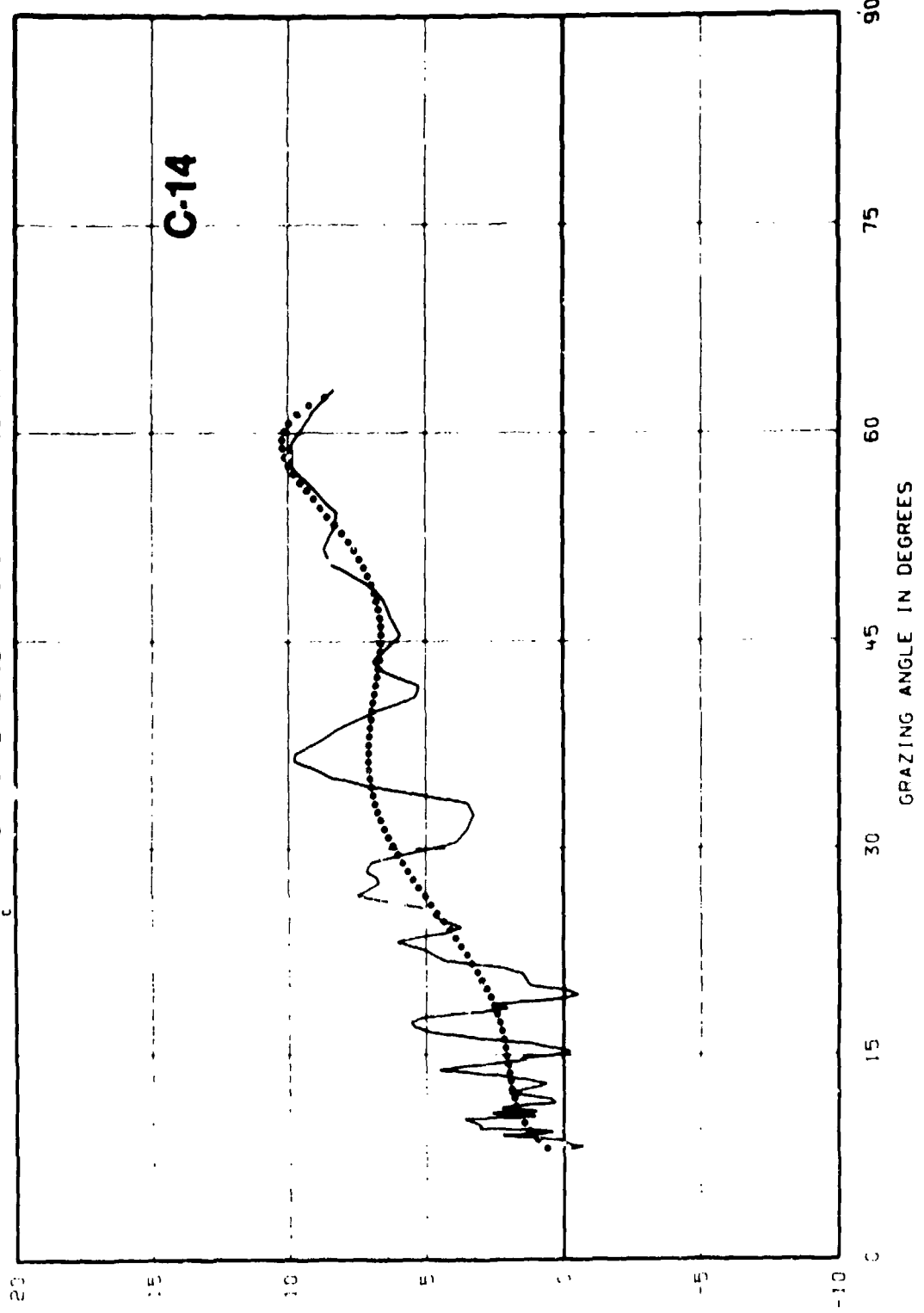
BOTTOM LOSS VS GRAZING ANGLE  
MAINLOBE STATION BL-2 (28 30N 70 30W) 3353 METER RECEIVER  
SOLID LINE-3 PT. MOVING AVG, DOTTED LINE-POLYNOMIAL (ORDER 6)  
 $F_c = 252.0\text{Hz}$  BANDWIDTH 224.5Hz - 282.9Hz



BOTTOM LOSS VS GRAZING ANGLE  
MAINLOPE STATION BL-2 (28 30N 70 30W) 3353 METER RECEIVER  
SOLID LINE-3 PT. MOVING AVG, DOTTED LINE-POLYNOMIAL (ORDER 6)  
 $f_c = 325.0\text{Hz}$  BANDWIDTH( 287.4Hz - 367.5Hz)



BOTTOM LOSS VS GRAZING ANGLE  
MAINLOBE STATION BL-2 (28 30N 70 30W) 3353 METER RECEIVER  
SOLID LINE-3 PT. MOVING AVG, DOTTED LINE-POLYNOMIAL (ORDER 6)  
 $F_c = 445.0\text{MHz}$  BANDWIDTH( 396.4Hz - 499.5Hz)

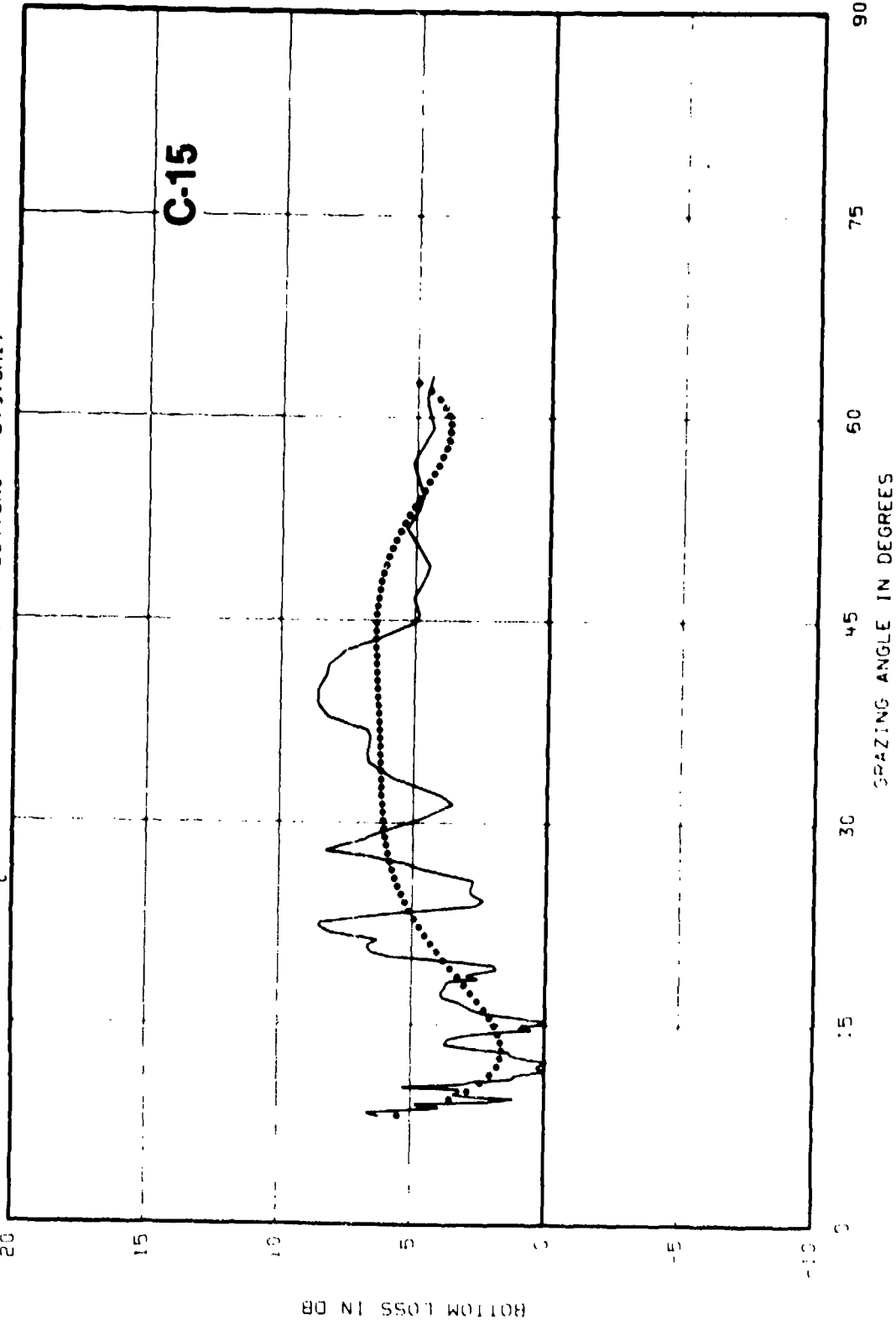


C-14

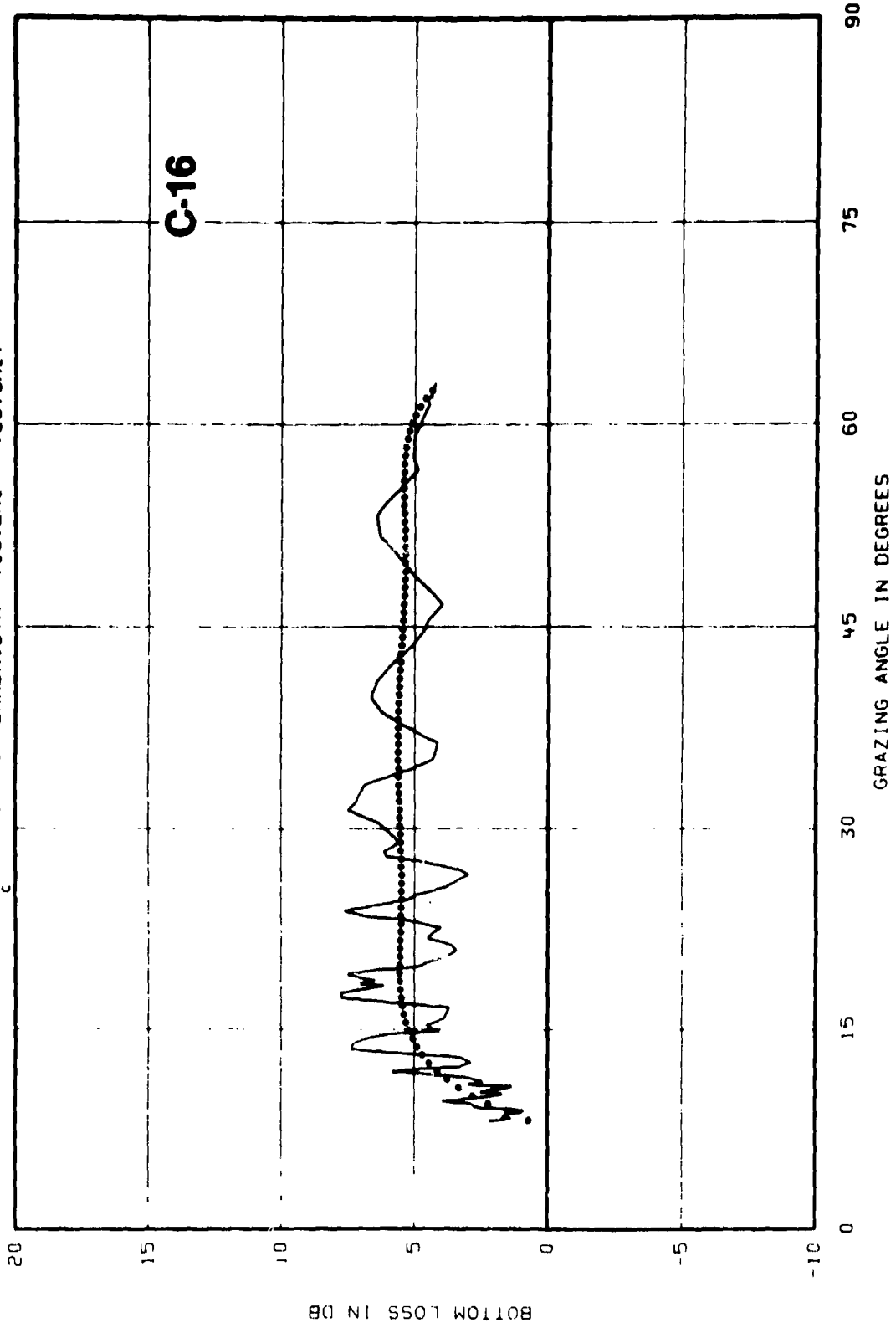
BOTTOM LOSS IN DB

BOTTOM LOSS VS GRAZING ANGLE  
MAINLOBE STATION BL-2 (28 30N 70 30W) 3353 METER RECEIVER  
SOLID LINE-3 PT. MOVING AVG, DOTTED LINE-POLYNOMIAL (ORDER 6)

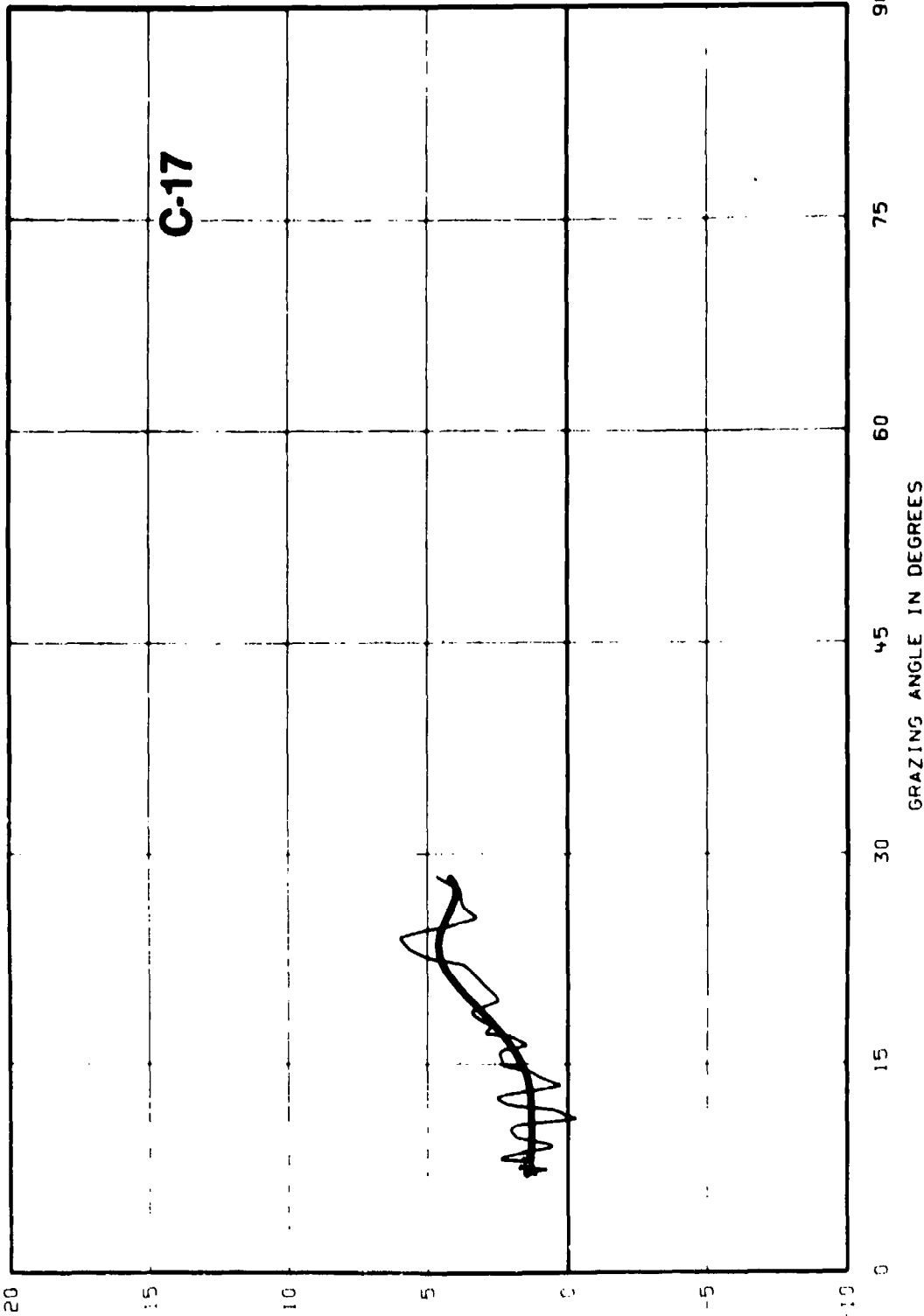
$F_c = 600.0\text{Hz}$  BANDWIDTH( 534.5Hz - 673.5Hz)



BOTTOM LOSS VS GRAZING ANGLE  
MAINLOBE STATION BL-2 (28 30N 70 30W) 3353 METER RECEIVER  
SOLID LINE-3 PT. MOVING AVG, DOTTED LINE-POLYNOMIAL (ORDER 6)  
 $F_c = 745.0\text{Hz}$  BANDWIDTH( 703.2Hz - 789.3Hz)



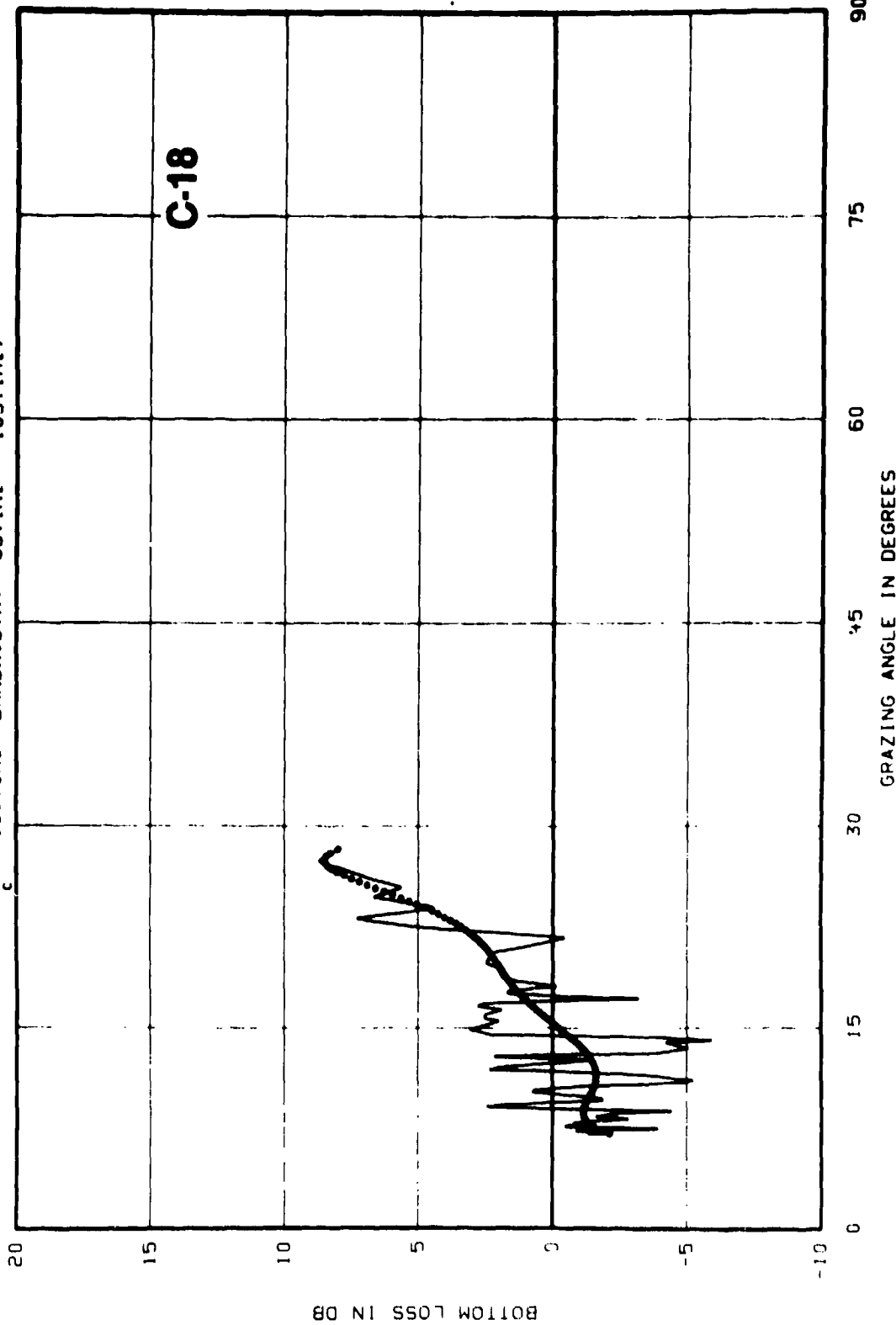
BOTTOM LOSS VS GRAZING ANGLE  
MAINLOBE STATION BL-3 (29 00N 70 30W) 3353 METER RECEIVER  
SOLID LINE-3 PT. MOVING AVG, DOTTED LINE-POLYNOMIAL (ORDER 6)  
BROADBAND BANDWIDTH( 10.0Hz - 750.0Hz)



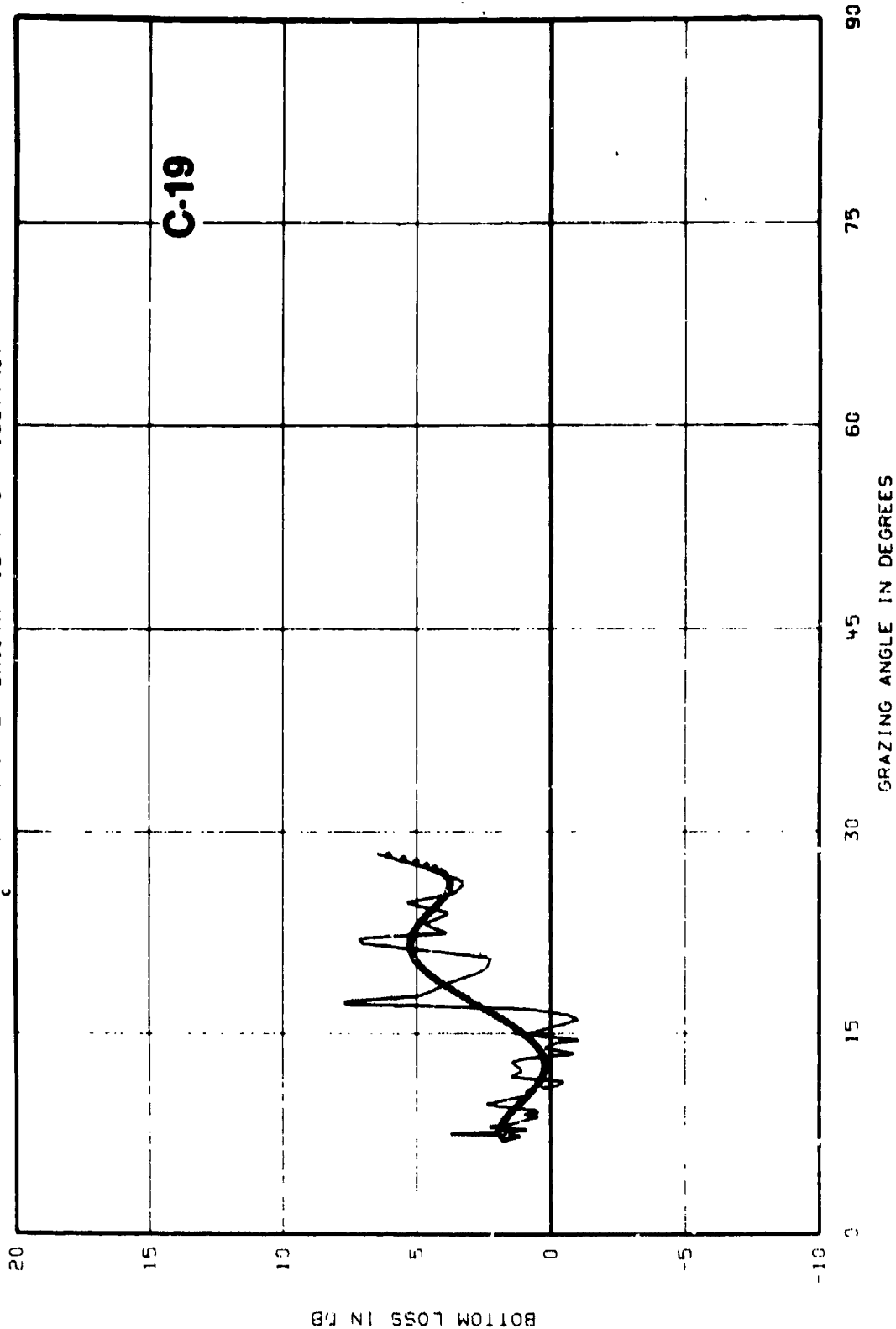
BOTTOM LOSS IN DB

GRAZING ANGLE IN DEGREES

BOTTOM LOSS VS GRAZING ANGLE  
MAINLOBE STATION BL-3 (29 00N 70 30W) 3353 METER RECEIVER  
SOLID LINE-3 PT. MOVING AVG, DOTTED LINE-POLYNOMIAL (ORDER 6)  
 $F_c = 100.0\text{Hz}$  BANDWIDTH( 95.1Hz - 105.1Hz)

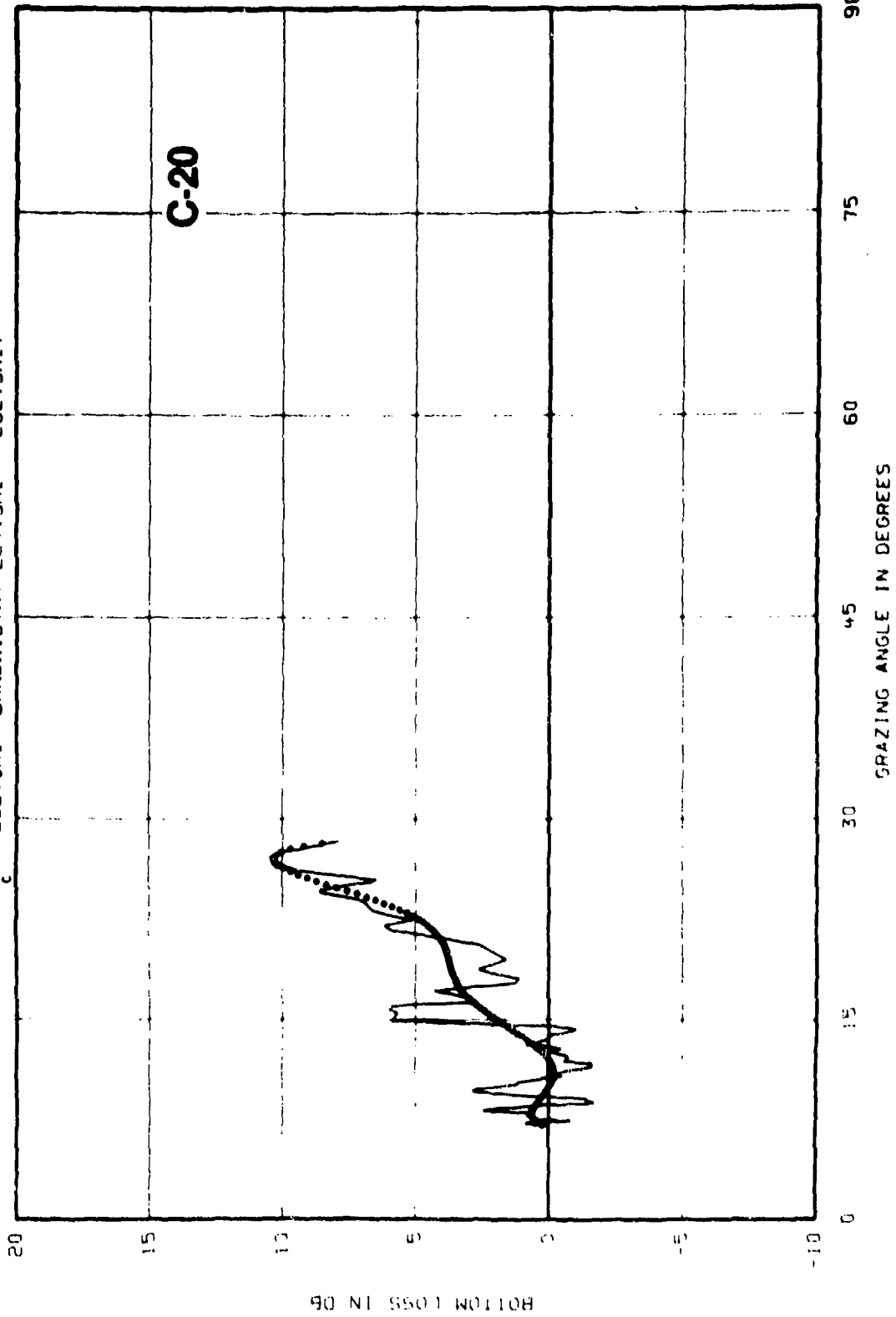


BOTTOM LOSS VS GRAZING ANGLE  
MAINLOBE STATION BL-3 (29 00N 7G 30W) 3353 METER RECEIVER  
SOLID LINE-3 PT. MOVING AVG. DOTTED LINE-POLYNOMIAL (ORDER 6)  
 $F_c = 177.0\text{Hz}$  BANDWIDTH 157.7Hz - 198.7Hz

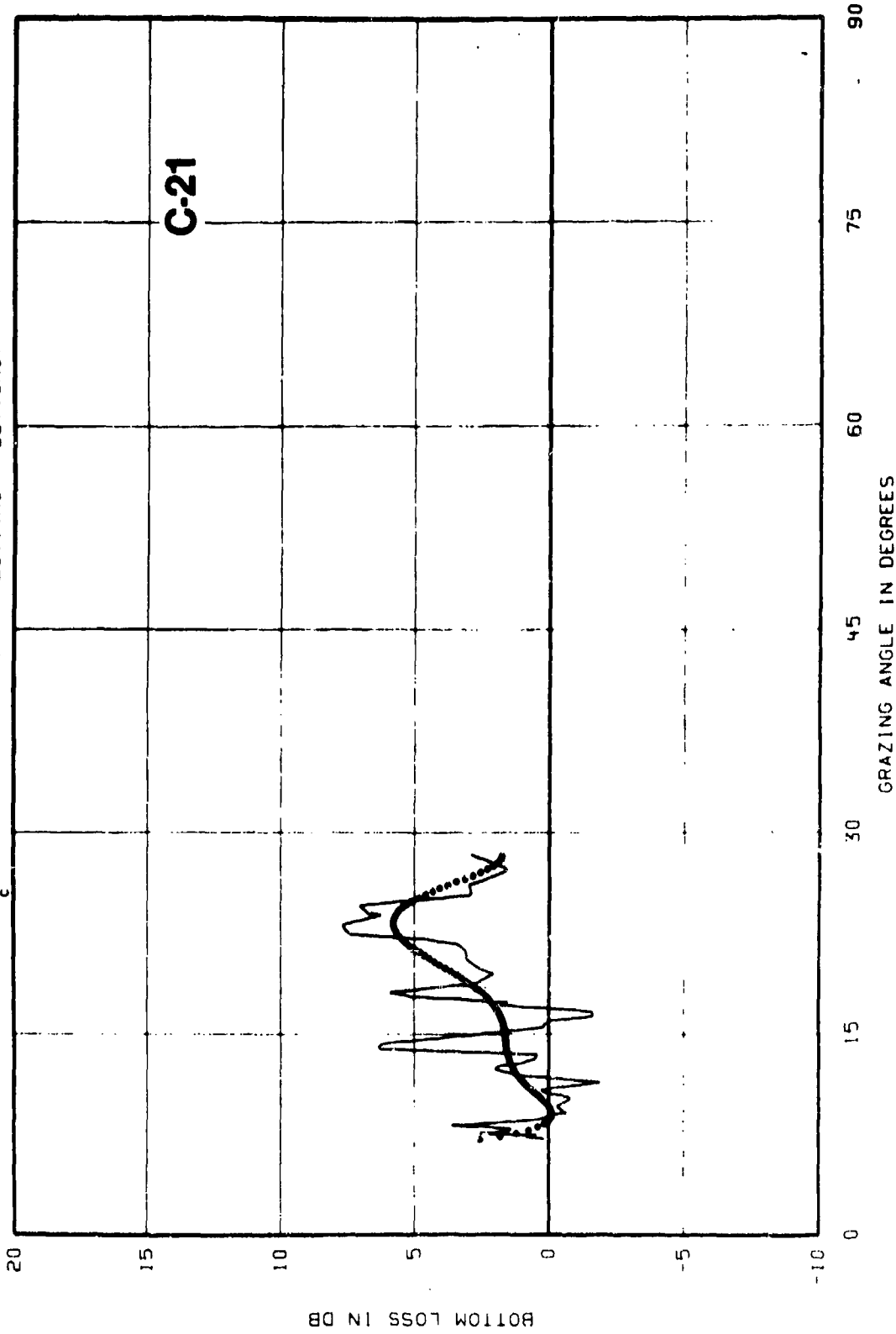


BOTTOM LOSS VS GRAZING ANGLE  
MAINLOBE STATION BL-3 (29 00N 70 30W) 3353 METER RECEIVER  
SOLID LINE-3 PT. MOVING AVG, DOTTED LINE-POLYNOMIAL (ORDER 6)

$F_c = 252.0\text{Hz}$  BANDWIDTH(  $224.5\text{Hz} - 282.9\text{Hz}$  )

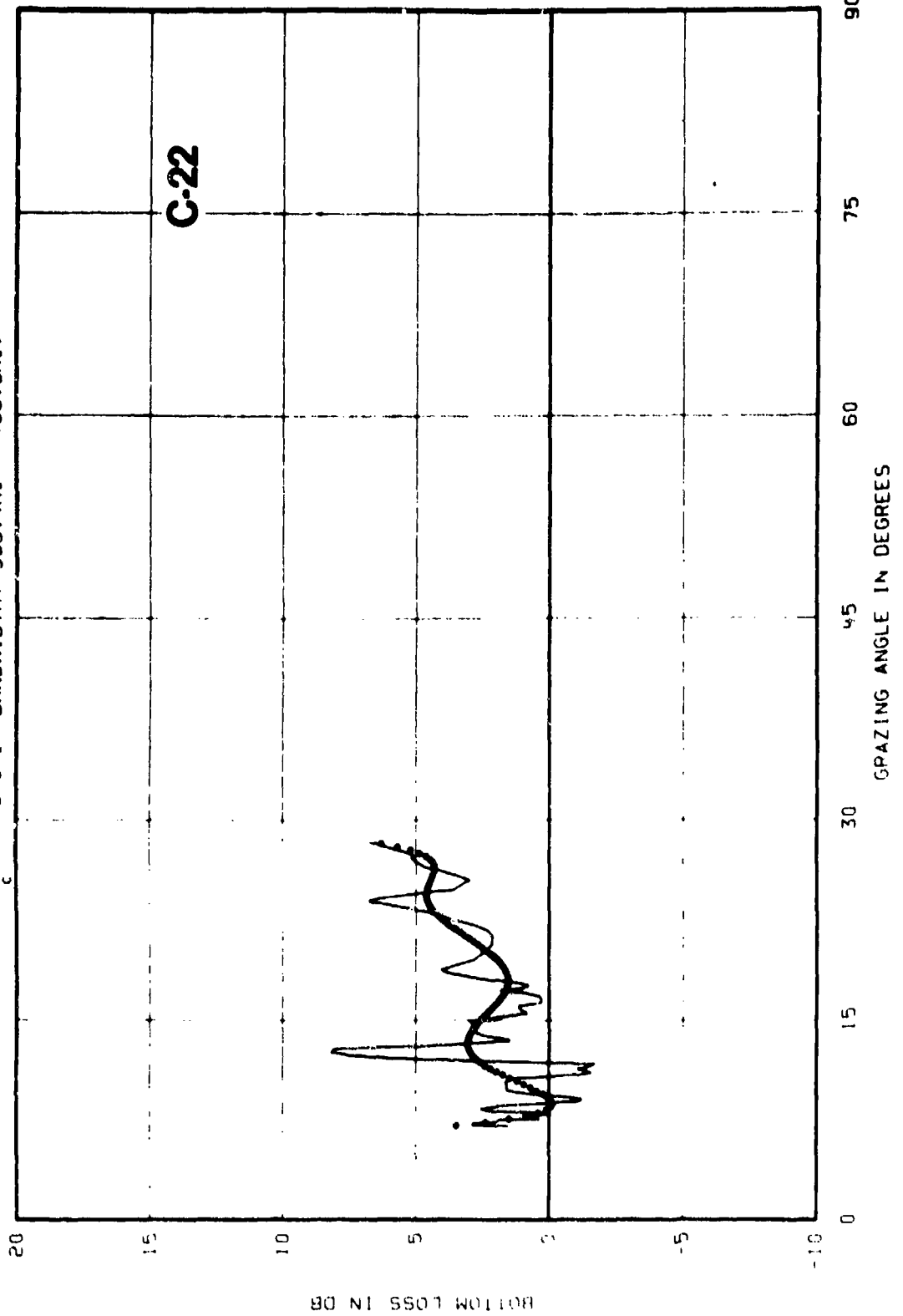


BOTTOM LOSS VS GRAZING ANGLE  
MAINLOBE STATION BL-3 (29' 00N 70 30W) 3353 METER RECEIVER  
SOLID LINE-3 PT. MOVING AVG, DOTTED LINE-POLYNOMIAL (ORDER 6)  
 $F_c = 325.0\text{Hz}$  BANDWIDTH( 287.4Hz - 367.5Hz)

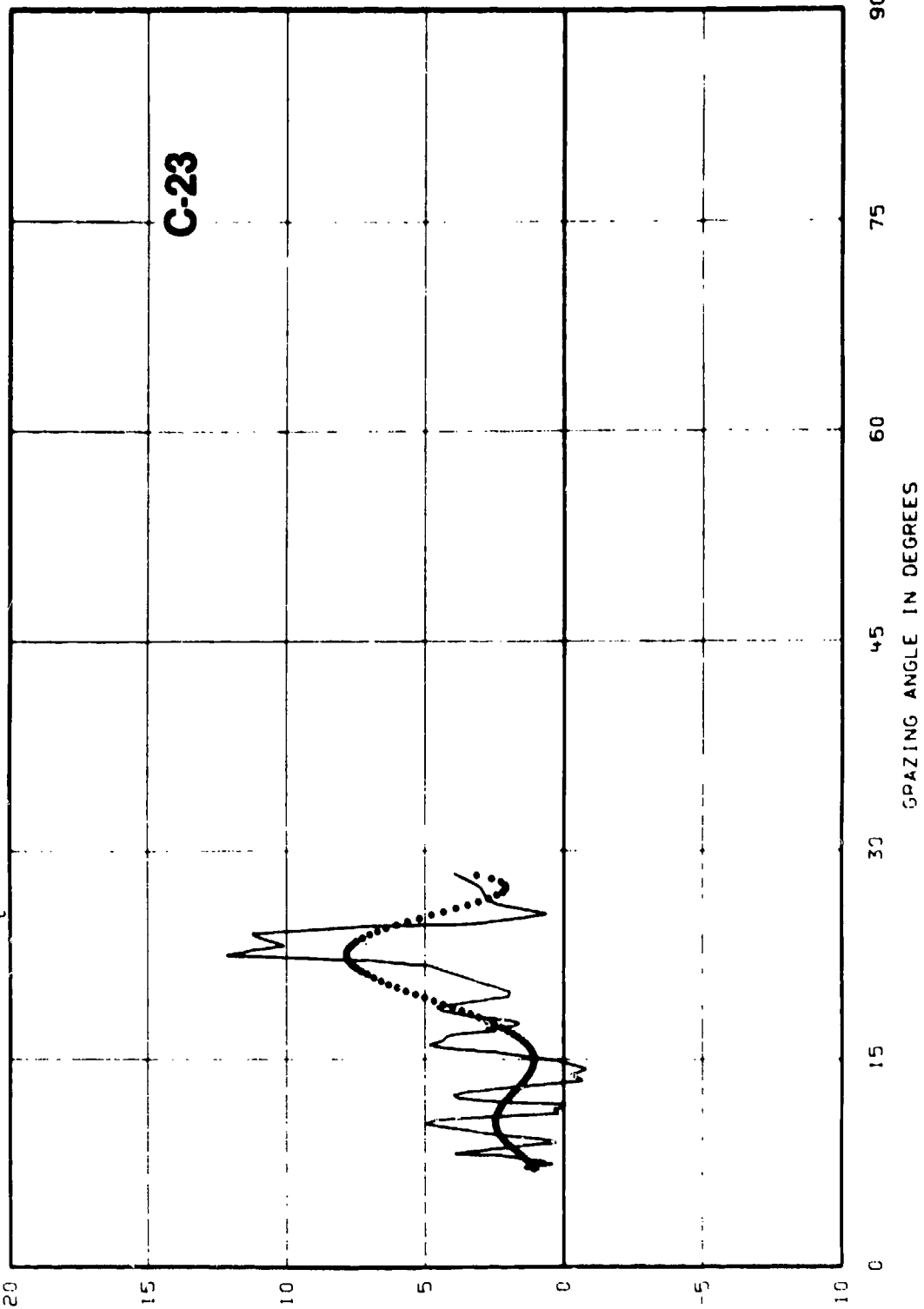


BOTTOM LOSS VS GRAZING ANGLE  
MAINLOBE STATION BL-3 (29 00N 70 30W) 3353 METER RECEIVER  
SOLID LINE-3 PT. MOVING AVG, DOTTED LINE-POLYNOMIAL (ORDER 6)

$F_c = 445 \text{ MHz}$  BANDWIDTH(  $396.4 \text{ Hz} - 499.5 \text{ Hz}$  )

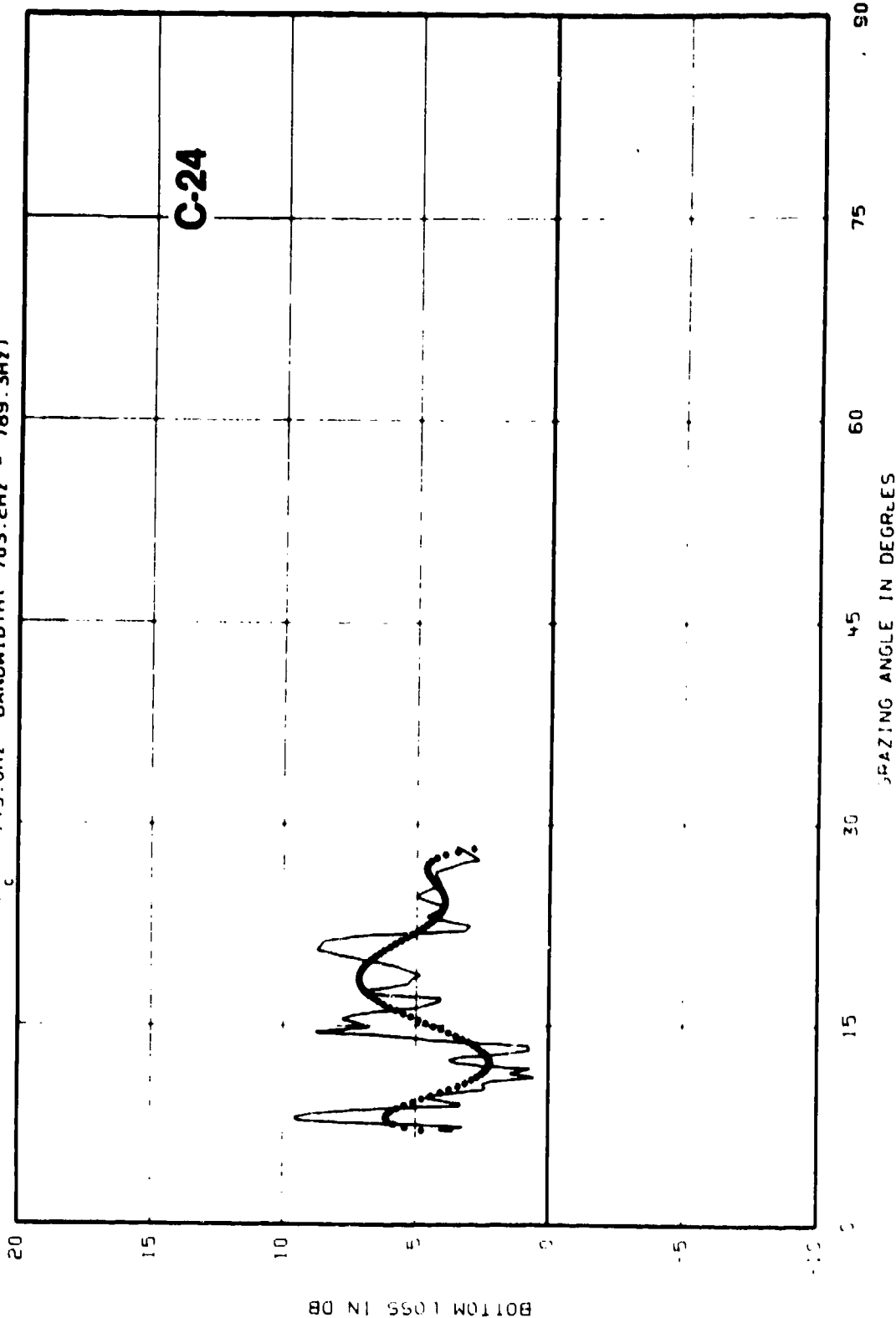


BOTTOM LOSS VS GRAZING ANGLE  
MAINLOBE STATION BL-3 (29 00N 70 30W) 3353 METER RECEIVER  
SOLID LINE-3 PT. MOVING AVG, DOTTED LINE-POLYNOMIAL (ORDER 6)  
 $F_c = 600.0\text{Hz}$  BANDWIDTH( 534.5Hz - 673.5Hz)

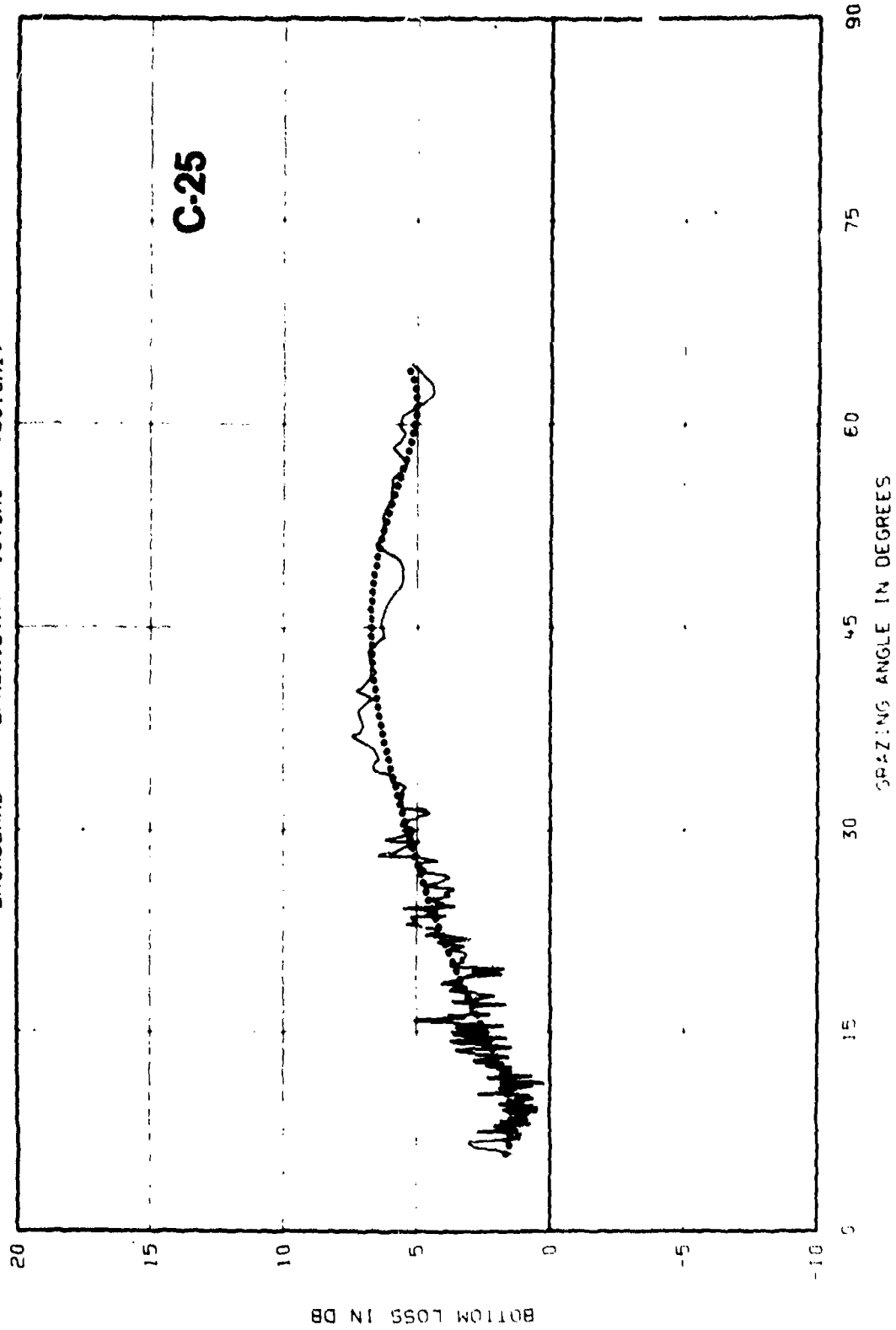


BOTTOM LOSS IN DB

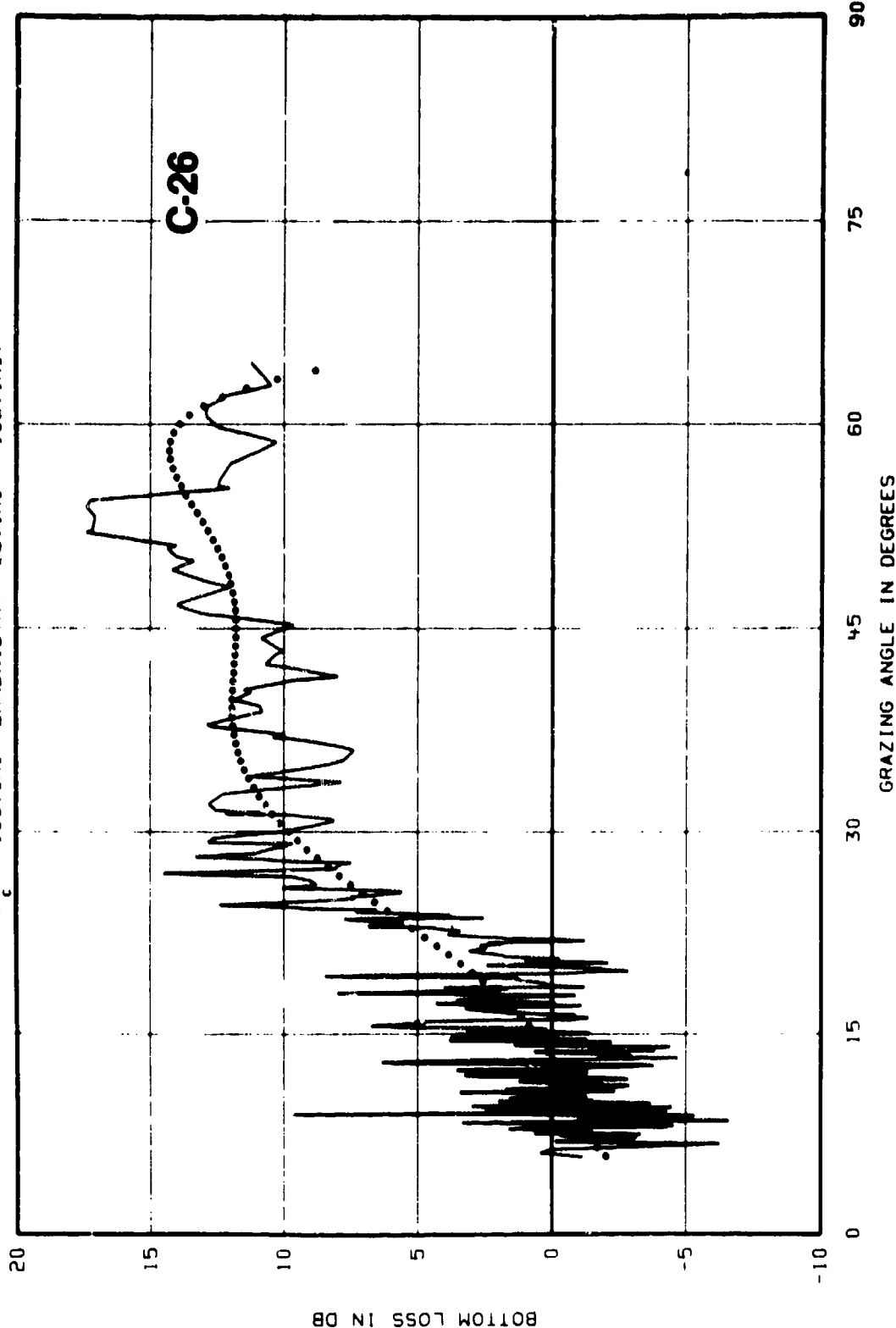
BOTTOM LOSS VS GRAZING ANGLE  
MAINLOBE STATION BL-3 (29 00N 70 30W) 3353 METER RECEIVER  
SOLID LINE-3 PT. MOVING AVG, DOTTED LINE-POLYNOMIAL (ORDER 6)  
 $F_c = 745.0\text{Hz}$  BANDWIDTH( 703.2Hz - 789.3Hz)



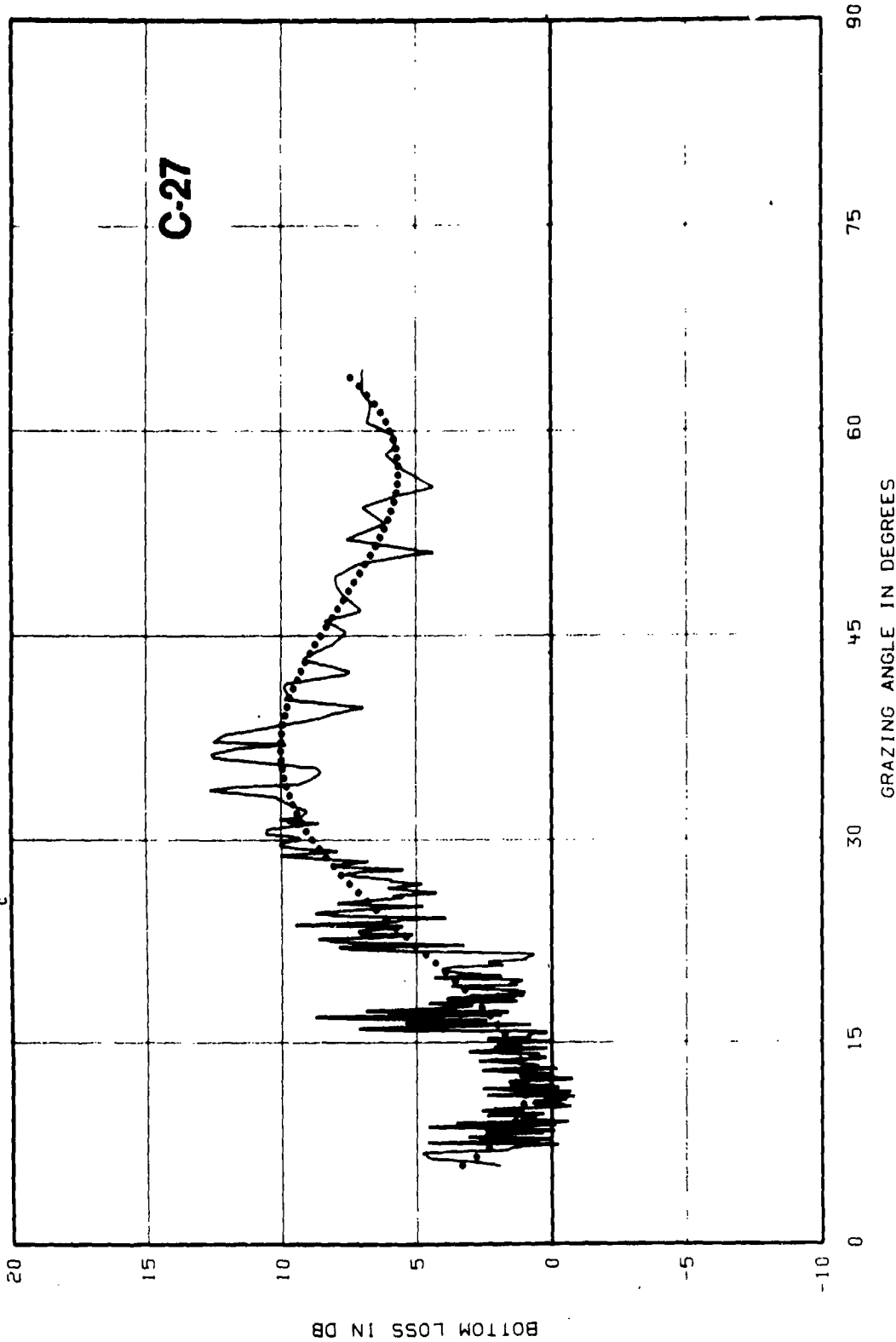
BOTTOM LOSS VS GRAZING ANGLE  
MAINLOBE COMBINED STATIONS BL-1(U), BL-U(L), BL-2, AND BL-3  
SOLID LINE-3 PT. MOVING AVG, DOTTED LINE-POLYNOMIAL (ORDER 6)  
BROADBAND BANDWIDTH( 10.0Hz - 750.0Hz)



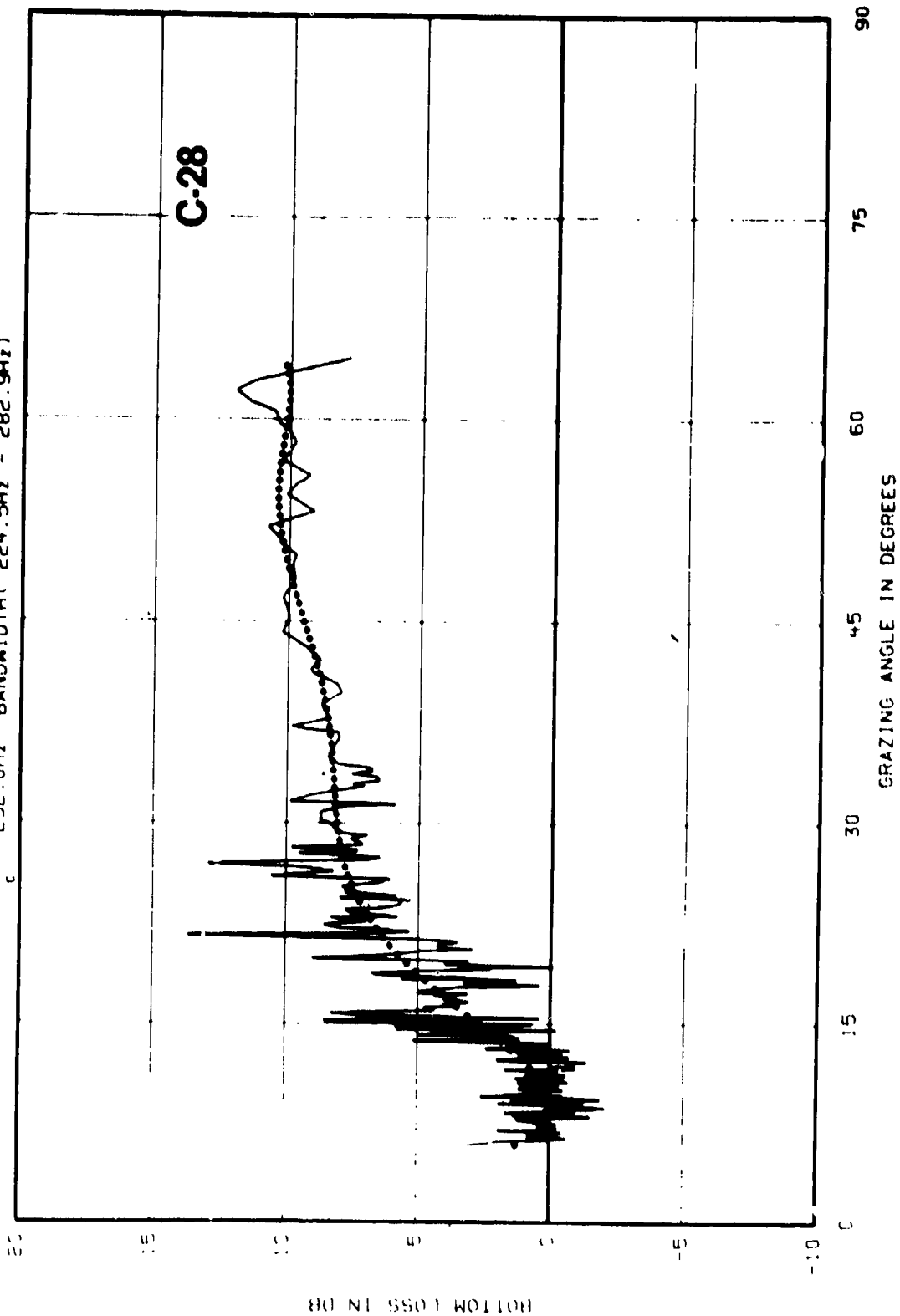
BOTTOM LOSS VS GRAZING ANGLE  
MAINLOBE COMBINED STATIONS BL-1(U), BL-U(L), BL-2, AND BL-3  
SOLID LINE-3 PT. MOVING AVG, DOTTED LINE-POLYNOMIAL (ORDER 6)  
 $F_c = 100.0\text{Hz}$  BANDWIDTH( 95.1Hz - 105.1Hz)



BOTTOM LOSS VS GRAZING ANGLE  
MAINLOBE COMBINED STATIONS BL-1(U), BL-U(L), BL-2, AND BL-3  
SOLID LINE-3 PT. MOVING AVG, DOTTED LINE-POLYNOMIAL (ORDER 6)  
 $F_c = 177.0\text{Hz}$  BANDWIDTH( 157.7Hz - 198.7Hz)

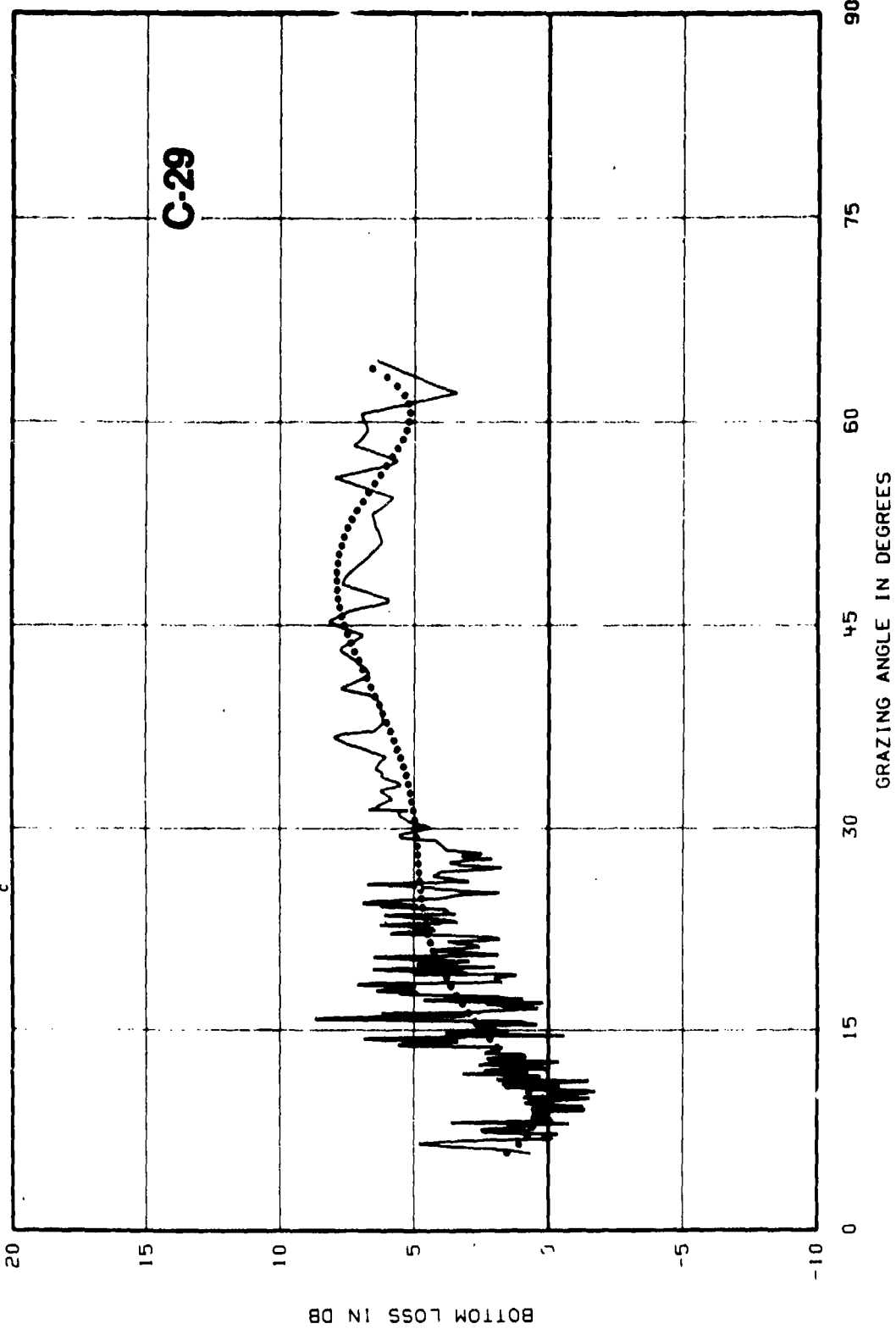


BOTTOM LOSS VS GRAZING ANGLE  
MAINLOBE COMBINED STATIONS BL-1(U), BL-U(L), BL-2, AND BL-3  
SOLID LINE-3 PT. MOVING AVG, DOTTED LINE-POLYNOMIAL (ORDER 6)  
 $F_c = 252.0\text{Hz}$  BANDWIDTH(  $224.5\text{Hz} - 282.9\text{Hz}$  )

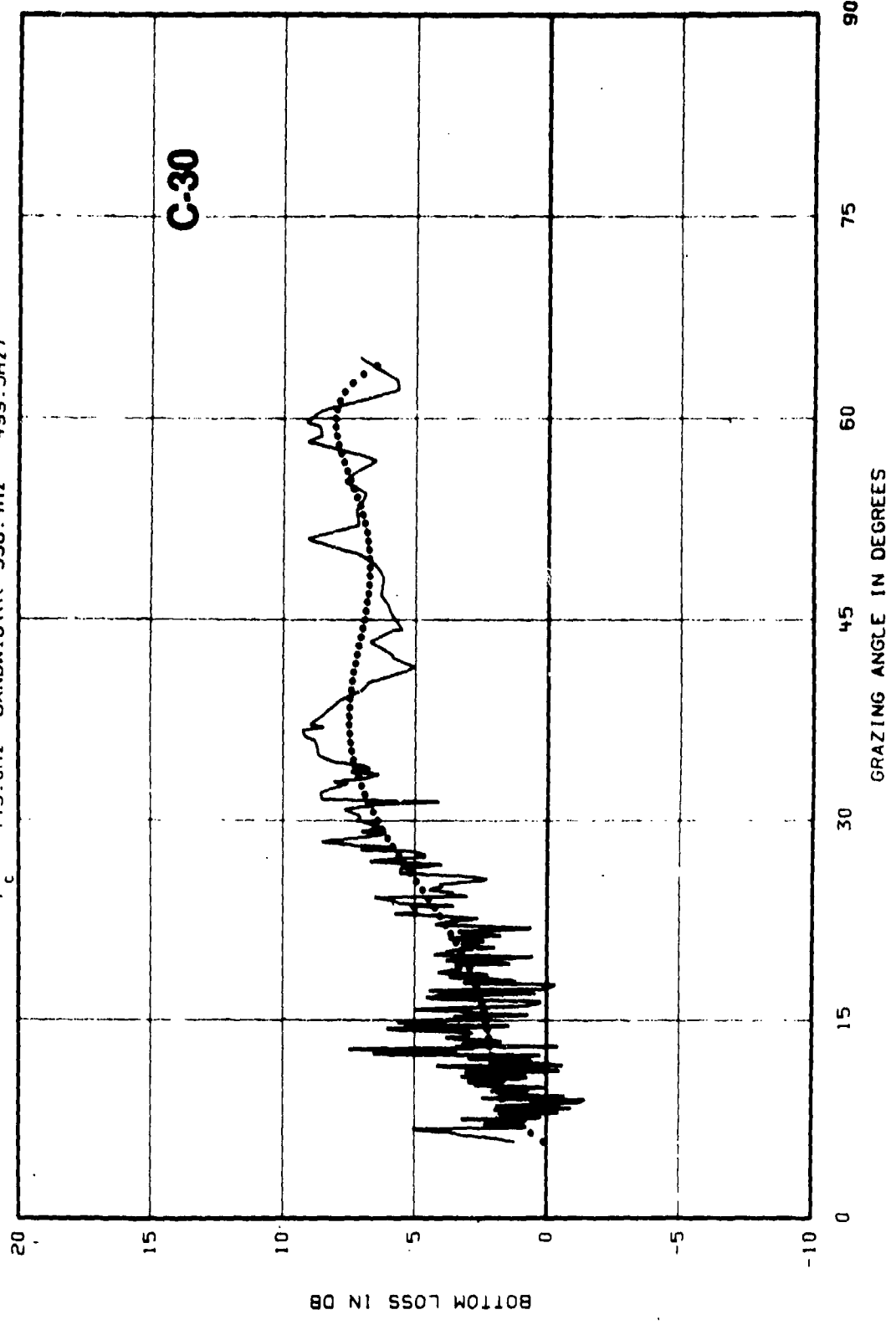


BOTTOM LOSS VS GRAZING ANGLE  
MAIN LOBE COMBINED STATIONS BL-1(U), BL-U(L), BL-2, AND BL-3  
SOLID LINE-3 PT. MOVING AVG, DOTTED LINE-POLYNOMIAL (ORDER 6)

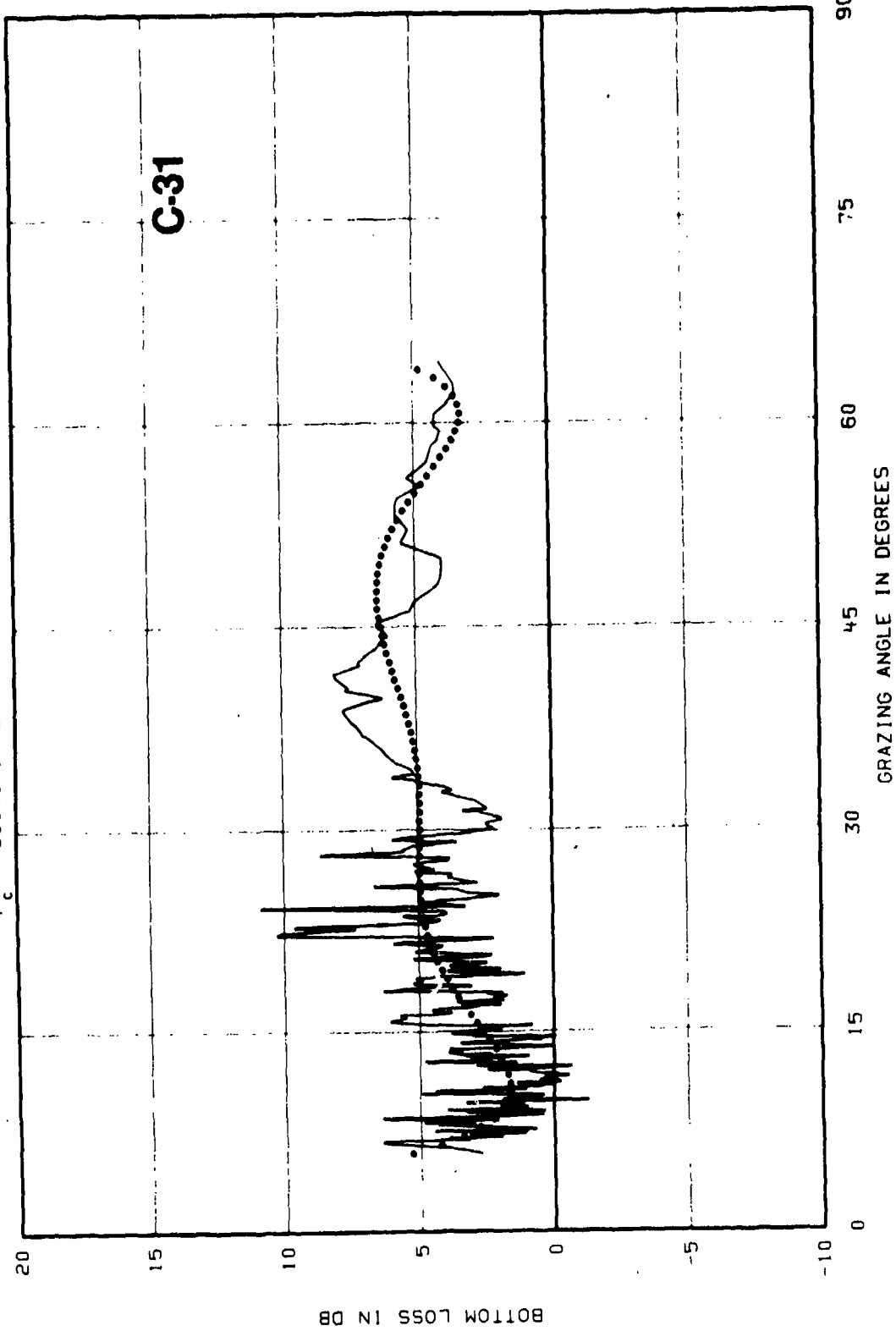
$F_c = 325.0\text{Hz}$  BANDWIDTH(  $287.4\text{Hz} - 367.5\text{Hz}$  )



BOTTOM LOSS VS GRAZING ANGLE  
MAINLOBE COMBINED STATIONS BL-1(U), BL-U(L), BL-2, AND BL-3  
SOLID LINE-3 PT. MOVING AVG, DOTTED LINE-POLYNOMIAL (ORDER 6)  
 $f_c = 445.0\text{Hz}$  BANDWIDTH( 396.4Hz - 499.5Hz)

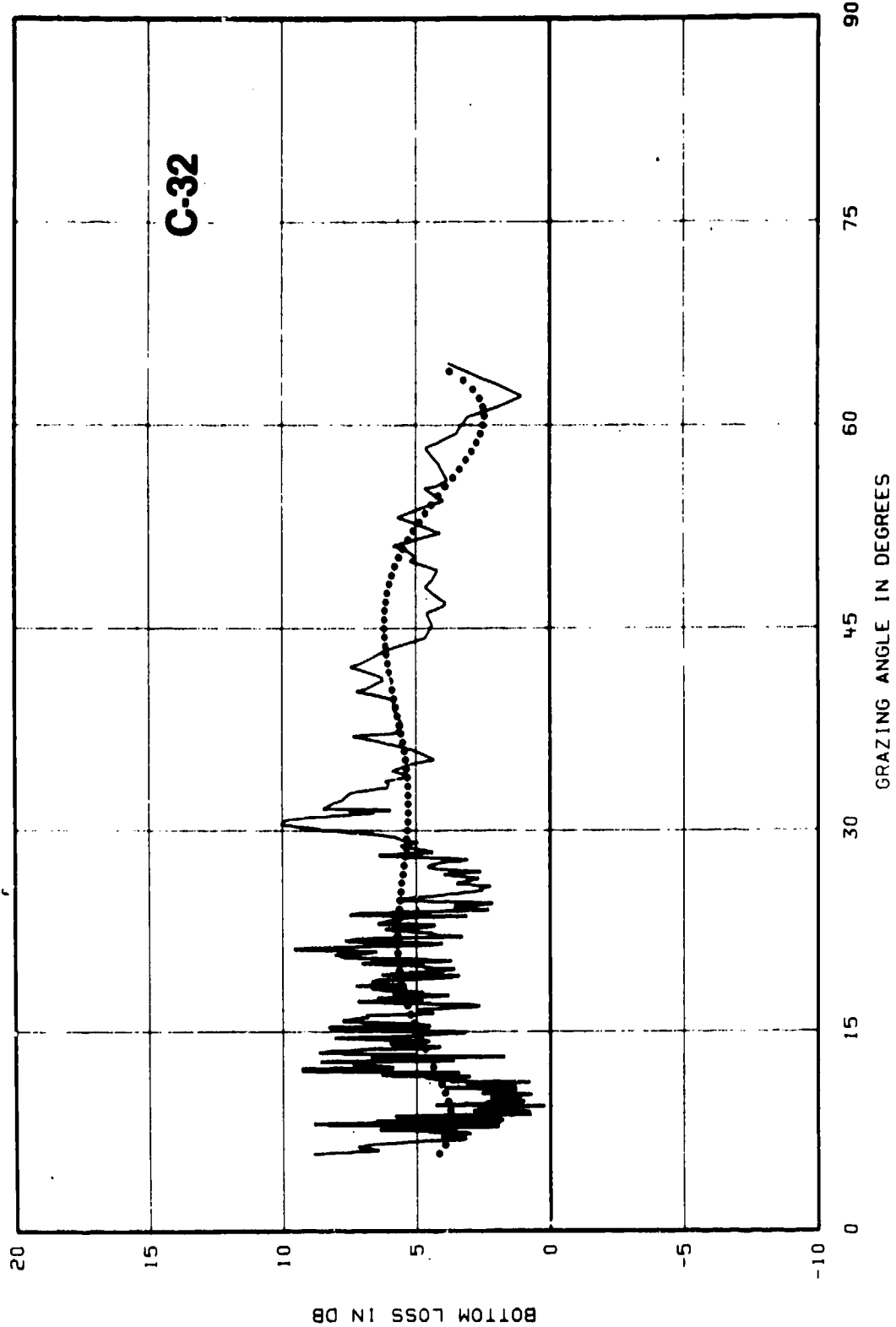


BOTTOM LOSS VS GRAZING ANGLE  
MAINLOBE COMBINED STATIONS BL-1(U), BL-U(L), BL-2, AND BL-3  
SOLID LINE-3 PT. MOVING AVG, DOTTED LINE-POLYNOMIAL (ORDER 6)  
 $F_c = 600.0\text{Hz}$  BANDWIDTH( 534.5Hz - 673.5Hz)



BOTTOM LOSS VS GRAZING ANGLE  
MAINLOBE COMBINED STATIONS BL-1(U), BL-U(L), BL-2, AND BL-3  
SOLID LINE-3 PT. MOVING AVG, DOTTED LINE-POLYNOMIAL (ORDER 6)

$F_c = 745.0\text{Hz}$  BANDWIDTH( 703.2Hz - 789.3Hz)



INITIAL DISTRIBUTION LIST

ADDRESSEE	NO. OF COPIES
CINCLANTFLT	1
CINCPACFLT	1
COMMANDER IN CHIEF, ATLANTIC (INEASTLANT) CDR FOUKE (SACLANT) C-32	1
COMSUBLANT	1
COMSIBPAC	1
NUSC Science Advisor COMSUBLANT	1
COMSUBLANT (Dr. Mueller)	1
FLEET ASW Tactical School (CDR Greuggeman)	1
COMSUBDEVTWELVE (CDR Doors, J. Seaton)	2
ASN(R&D)	1
ONR, ONR-102-D, -102, -480, -481, -483, -485, -212 -222, -230, -486	10
CNO, OP-095, -098, -03, -951, -951D, -951E, -953, -955, -96, -095E, -983, -955G, -95E	13
CNM, MAT-08T2, -08T12, -08T24, SP-20, ASW-111	5
DDR&E (G. Cann)	1
DARPA	1
NRL	2
NRL, USRD, NRL 2627	2
NRL, AESD	1
NORDA	1
Dr. R. Goodman, 110	1
NRL 8170, 7201, 9370	3
OCEANAV	1
NAVOCEANO, Code 02 C37, 6130	3
NOO, Code 03, 06, 6130, 3600	4
NAVELECSYSCOM, ELEX-03, -320, PME-124,	3
NAVSEASYSYSCOM, SEA-03C, -06H1, -06H1-1, -06H1-2, -06H1-3 -06H1-4(4), -06H2, -09G32(4), -660, -6606-22	16
NAVAIRDEVGEN	1
DTNSRDC	1
NAVCOASTSYSLAB	1
NAVSURFWPNCEN	1
NAVOCEANSYSCEN	1
Library, Code 6565	1
NAVPGSCOL	2
NAVWARCOL	1
APL/UW, Seattle	1
ARL/PENN State, State College	1
ARL, Univ of Texas	1
CENTER FOR NAVAL ANALYSES (ACQUISITION UNIT)	1
DDC, ALEXANDRIA	12
MARINE PHYSICAL LAB, SCRIPPS (G. Shor)	2
NOAA/ERL	1
Lamont-Doherty Geological Observatory (R. Houtz, C. Windish, W. Pitman)	3
SACLANTCEN, La Spezia, Italy	2
ONR, London	2

AREA, Canada	1
MAAL, Argentina	1
MOO, UK (LDR Barnett)	1
The Director, Royal Australian Navy Research Laboratory Garden Island, New South Wales 2000, Australia	2
RANRL (M. Hall, P. Nysen)	2
Australian Defence R&D Attache, Washington, DC	2
DREA (H. Merlinger, Major J. Ross, D. Scholfield)	3
DREP (D. Thomson, R. Chapman)	2
SACLANT ASW Research Centre (F. Jensen)	1
NCSL (T. Watson)	1
A. D. Little, Inc., (G. Raisbeck), Acorn Park, Cambridge, MA 02140	1
TRW Systems, Inc., (R. Brown), 7600 Colshire Drive, McLean, VA 22101	1
Planning Systems, Inc., (L. P. Solomon), 7900 Westpark Drive, McLean, VA 22101	1
Undersea Research Corp., (J. Hess), 1920 Aline Avenue, Vienna, VA 22180	1
Underwater Systems, Inc., (M. Weinstein), 8121 Georgia Avenue, Silver Spring, MD 20910	1
Bell Telephone Laboratories, Whippany, NJ 07981	1
B-K Dynamics, Inc. (A. E. Fadness), 2351 Shady Grove Road, Rockville, MD 20850	1
Tracor (J. T. Gottwald), 1601 Research Boulevard, Rockville, MD 20850	1
Texas Instruments, Inc. (A. Kirst), P.O. Box 6015, MS 400, Dallas, TX 75222	1
Raff Associates, Inc. (J. Bowen), 912 Thayer Avenue, Silver Spring, MD 20910	1
University of Miami (S. C. Daubin), School of Marine & Atmospheric Sciences, 10 Rickenbacker Causeway, Miami, FA 33149	1
Woods Hole Oceanographic Institution (E. E. Hays, J. Ewing), Woods Hole, MA 02543	2
Western Electric Company, 2400 Reynolds Road, Winston-Salem, NC	1
Tetra-Tech, Inc. (C. H. Dabney), 1911 Fort Meyer Drive, Arlington, VA 22209	1
Xonics, Inc., (S. Kulek), 6837 Hayvenhurst Avenue, Van Nuys, CA 91406	1
Seismic Engineering Co. (Mr. Leuhrmann), 3616 W. Alabama, Houston, TX 77027	1
Bolt, Beranek and Newman, Inc. (D. Sachs), 1701 N. Fort Mayer Drive, Arlington, VA 22209	1
Supreme Allied Commander, Atlantic, Antisubmarine Warfare Research Center (O. F. Hastrup), La Spezia, Italy	1
Naval Research Laboratory, (R. H. Ferris, F. Ingenito), Washington, DC	3
Naval Ordnance Laboratory (R. J. Urick, I. Blatstein), Silver Springs, MD	2

Naval Undersea Center (H. P. Bucker, H. E. Morris, D. Gordon, M. Pedersen, R. McGirr, G. DiLoreto, J. Stewart, E. Chaika), San Diego, CA	8
Naval Air Development Center, (R. Balonis, C. Bartberger), Johnsville, PA	2
Naval Oceanographic Office (R. E. Christensen, W. Geddes, O. I. Olachok, K. MacKenzie), NSTL, Bay St. Louis, MS	3
Office of Naval Research, Code 780, 486, Arlington, VA	1
Defence Scientific Establishment (R. W. Bannister, K. M. Guthrie) HMNZ Dockyard, Auckland 9, New Zealand	2
Mr. Allen Boyles, Johns Hopkins University, Applied Physics Laboratory, Johns Hopkins Rd., Laurel, MD 20810	1
Mr. John S. Bird, Mr. R. Verrall, Defence Research Establishment Pacific Forces Mail Office, Victoria, B.C. VOSIBO Canada	2
Mr. J. I. Mahler/CSA 1-2321, Automation Industries, Inc., 14000 Georgia Ave., Silver Spring, MD 20910	1
Mr. Eugene J. Feldhaus, EDO Corporation, Research Dept. 13-10 111 St., College Point, NY 11356	1
Mr. Joie P. Jones, Case Western Reserve University 2058 Abington Rd., Cleveland, OH 44106	1
Dr. R. Dicus, NRL, Code 8120	1
Dr. W. P. Cunningham, Dr. D. F. Leipper, Naval Post Graduate School, Monterey, CA	2
Dr. D. Vasholz, NCSL, Code 791	1
Dr. M. Wolpert, NSRDC, Code 1939	1
Dr. D. Stickler, Dr. Sm. McDaniel, Dr. A. Boyles, Johns Hopkins University, Applied Research Laboratory, Penn State	3
Dr. Jorge C. Novarini, ARMADA ARGENTINA, Servicio de Hidrografin Naval Departamento Oceanografia, Montes de Oca 2124, Buenos Aires, Argentina	1
Dr. Ashoke K. Nath, Geoquest International Ltd., 4605 Post Oak Place, Suite 130, Houston, TX 77027	1
Dr. David E. Grass, Diagnostic/Retrieval Systems, Inc., 30 South St., 30 South St., Mt. Vernon, NY 10550	1
Dr. G. P. Gopalakushman, Director, Naval Physical and Oceanographic Laboratory, Naval Base, Cochin-Y, India	1
Dr. John Gill, Mr. Philip Lindop, Admiralty Research Laboratory Portland, Dorset, United Kingdom	2
Dr. John H. Stockhausen, Canadian Defense Research Establishment Atlantic, P.O. Box 1012, Dartmouth, N.S. B2y 327	1
Dr. C. Jeannin, Direction des Construction: Navales et Armes Laboratoire Sous Marine, 83 Le Brusq, France	1
O. Grenness, N-3191 Horten, Norwegian Defense Research Establishment Norway	1
Dr. A. Eller, NRL	1
D. J. Dixey, UK Hydrographic Office	1
Dr. Allan V. Oppenheim, Mass. Institute Tech, Cambridge, MA	1
Dr. Sven Treitel, Dr. W. French, Amoco Production Corp., Tulsa, OK	2
Dr. G. Fain, Dr. L. Estes, Southeastern Mass. University	2
Dr. G. Bernard, ARL University of Texas	1
Dr. A. O. Williams, Brown University, Providence, RI	1

Dr. H. W. Marsh, General Delivery, Penrose, NC 28766	1
Dr. L. Brekhovskikh, Academy of Sciences of USSR, Leninskii Prospect 14 Moscow 117071 USSR	1
Dr. F. Tappert, Courant Institute of Matl. Science, NYU, New York City, NY	1
Director, Weapons Research Establishment, Box 2151 G.P.O. Adelaide 5001, Australia	1
D. G. Strahle, H. A. D'Assumpaco, D. V. Wyllie, WRE Box 2151, G.P.O. Adelaide 5001, Australia	3
Dr. Milo Backus, Dept. of Geological Sciences, University of Texas at Austin, P.O. Box 7909, Austin, Texas 78712	1
Mr. Anthony F. Gangi, Texas A&M Univ., Dept. of Geophysics College Station, Texas 77843	1
Mr. John Grow, US Geological Survey Dept. of the Interior Office of Marine Geology, Woods Hole, MA 02543	1
Mr. Frank Levin, Exxon Production Research Co., Houston, Texas 77001	1